

UCLA

UCLA Electronic Theses and Dissertations

Title

Parallel Nonlinear Aeroelastic Computation for Fighter Wings in the Transonic Region

Permalink

<https://escholarship.org/uc/item/47c3914t>

Author

Larsen, Bradley Robert

Publication Date

2015

Peer reviewed|Thesis/dissertation

UNIVERSITY OF CALIFORNIA

Los Angeles

**Parallel Nonlinear Aeroelastic Computation for Fighter Wings in
the Transonic Region**

A dissertation submitted in partial satisfaction
of the requirements for the degree
Doctor of Philosophy in Aerospace Engineering

by

Bradley Robert Larsen

2015

© Copyright by

Bradley Robert Larsen

2015

ABSTRACT OF THE DISSERTATION

**Parallel Nonlinear Aeroelastic Computation for Fighter Wings in
the Transonic Region**

by

Bradley Robert Larsen

Doctor of Philosophy in Aerospace Engineering

University of California, Los Angeles, 2015

Professor Oddvar O. Bendiksen, Chair

In this dissertation, a parallel three-dimensional aeroelastic simulation is applied to current and next generation fighter aircraft wings. The computational model is a nonlinear fluid and structural mesh coupled using the Direct Eulerian-Lagrangian method. This method attaches unique local coordinates to each node and connects the fluid mesh to the structure in such a way that a transformation preserved to the global coordinates. This allows the fluid and structure to be updated in the same time step and maintains spatial accuracy at their interface. The structural mesh is modeled using modified nonlinear von Karman finite elements and is discretized using the Galerkin finite element method. The fluid mesh also used the Galerkin finite element method to discretize the unsteady Euler equations.

Computational results over a large range of Mach numbers and densities are presented for two candidate fighter wing models for transonic wing tunnel testing. The FX-35 is a trapezoidal wing based on the F-35A, and the F-Wing is a truncated delta wing similar to the F-16. Both wings exhibit a variety of flutter behaviors including strong bending-torsion flutter, limit-cycle oscillations, and essentially single degree-of-freedom responses.

The dissertation of Bradley Robert Larsen is approved.

William S. Klug

Ertugrul Taciroglu

Xiaolin Zhong

Oddvar O. Bendiksen, Committee Chair

University of California, Los Angeles

2015

Contents

- List of Figures** **vii**

- List of Tables** **xviii**

- Nomenclature** **xix**

- 1 Introduction** **1**
 - 1.1 Motivation for Research 1
 - 1.2 Literature Review 2
 - 1.2.1 Transonic Aeroelastic Computation 2
 - 1.2.2 Transonic Flutter Phenomena 5
 - 1.3 Problem Statement and Research Objectives 6
 - 1.4 Dissertation Outline 7

- 2 Fluid Model** **8**
 - 2.1 Introduction 8
 - 2.2 Governing Equations and Discretization 9
 - 2.3 Five-Stage Runge-Kutta Scheme 12

2.4	Boundary Conditions	13
2.5	Mesh Generation	14
3	Nonlinear Structural Model	16
3.1	Introduction	16
3.2	Structural Model	16
3.3	Direct Eulerian-Lagrangian Formulation	17
3.4	Typical Element Formulation	20
3.4.1	Out-of-Plane: Discrete Shear Triangle	20
3.4.2	In-Plane: Constant Strain Triangle	24
3.4.3	In-Plane and Out-of-Plane Coupling	25
3.4.4	Structural Element Equations	26
4	Fluid-Structure Coupling	29
4.1	Introduction	29
4.2	Fluid-Structure Boundary Model	30
4.3	Dynamic Aeroelastic Solution Procedure	33
5	Changes to the Aeroelastic Code	36
5.1	Introduction	36
5.2	Changes for use on the Hofmman2 Cluster	37
5.3	Parallelization	38
5.3.1	Division of Work	39
5.3.2	Sub-Domain Algorithm	39

5.3.3	Sub-domain Implementation	41
5.3.4	Optimization	42
5.4	Verification of Parallel Computational Accuracy	44
5.5	Benchmarking and Parallel Configuration Selection	47
6	Results: TDT Wing Models	50
6.1	Introduction	50
6.2	Candidate Wings: FX-35 and the F-Wing	51
6.3	Subsonic Stability Boundary	58
6.3.1	FX-35: Subsonic Stability	60
6.3.2	F-Wing: Subsonic Stability	72
6.4	Chimney Transition	80
6.4.1	FX-35: Chimney	81
6.4.2	F-Wing: Chimney	92
6.5	Mach Number Freeze	103
6.5.1	FX-35: Mach Freeze	104
6.5.2	F-Wing: Mach Freeze	121
7	Conclusions	132
7.1	Introduction	132
7.2	Conclusions	132
	Bibliography	135

List of Figures

2.1	<i>The Direct Eulerian-Lagrangian computational approach to fluid-structure interaction.</i>	9
3.1	<i>The Eulerian-Lagrangian Formualtion.</i>	18
3.2	<i>Various components of a typical structural element.</i>	20
3.3	<i>Nodal degrees of freedom for the DST.</i>	21
3.4	<i>In-plane deformation in Lagrangian coordiantes.</i>	22
3.5	<i>Local out-of-plane deformations.</i>	23
3.6	<i>Nodal degrees of freedom for the CST.</i>	24
3.7	<i>In-plane deformation in Lagrangian coordiantes.</i>	25
3.8	<i>Typical partition of an element tangent or secant stiffness matrix.</i>	28
4.1	<i>An aerodynamic fluid node attached to a structural element using area coordinates.</i>	31
4.2	<i>A Gaussian quadrature point attached to an aerodynamic fluid element using area coordinates.</i>	32
4.3	<i>Surface pressure being interpolated at a Gaussian quadrature point from the nodes of an aerodynamic fluid element.</i>	33
5.1	<i>Verification of parallel computational results versus original serial output.</i>	46

5.2	<i>Benchmarking results for the original and optimized parallel configurations. A range of results from three separate hardware tests are shown, demonstrating the varying performance of both hardware and software.</i>	48
6.1	<i>The FX-35 (left) and F-Wing (right) planforms.</i>	51
6.2	<i>The first four natural modes of the FX-35 wing planform.</i>	53
6.3	<i>The first two natural modes of the F-Wing planform.</i>	54
6.4	<i>Stability responses for the FX-35 wing at TDT conditions with zero angle of attack and 0.004 plate thickness.</i>	55
6.5	<i>Stability responses for the F-Wing at TDT conditions with zero angle of attack and 0.008 plate thickness.</i>	56
6.6	<i>Indication of the Subsonic Stability Boundary free stream Mach number range.</i>	59
6.7	<i>FX-35: Typical subsonic unstable flutter response at the wing tip (Mach 0.93, Density 0.1 kg/m³).</i>	60
6.8	<i>The full range of FX-35 wing tip flutter responses from stable (top left) to unstable (bottom right) at Mach 0.93.</i>	61
6.9	<i>FX-35: Strong bending-torsion flutter plunge response, demonstrating rapid amplitude growth at increased density (Mach 0.93, Density 0.2 kg/m³).</i>	63
6.10	<i>FX-35: Strong bending-torsion flutter pitch response, demonstrating rapid amplitude growth at increased density (Mach 0.93, Density 0.2 kg/m³).</i>	64
6.11	<i>FX-35: Phase plots corresponding to strong bending-torsion flutter (Mach 0.93, Density 0.2 kg/m³).</i>	64

6.12	<i>FX-35: Kinetic energy distribution between natural modes for strong bending-torsion flutter (Mach 0.93, Density 0.2 kg/m³).</i>	65
6.13	<i>FX-35: Weakly stable plunge response just below the flutter boundary (Mach 0.93, density 0.079 kg/m³).</i>	67
6.14	<i>FX-35: Weakly stable pitch response just below the flutter boundary, small hiccups in the response indicate first-torsion participation (Mach 0.93, density 0.079 kg/m³).</i>	67
6.15	<i>FX-35: Weakly unstable plunge response just above the flutter boundary (Mach 0.93, density 0.08 kg/m³).</i>	68
6.16	<i>FX-35: Weakly unstable pitch response just above the flutter boundary, small variations in the response indicate first-torsion participation here as well (Mach 0.93, density 0.08 kg/m³).</i>	68
6.17	<i>FX-35: Phase plots corresponding to a weakly stable response just below the flutter boundary; showing the slight wavering caused by first-torsion participation (Mach 0.93, density 0.079 kg/m³).</i>	69
6.18	<i>FX-35: Phase plots from a smaller subset of cycles showing the lack of variation within the pattern between cycles at similar amplitudes. The weakness of this coupling effect is most likely due to the relative strength of the modes involved (Mach 0.93, density 0.079 kg/m³).</i>	69
6.19	<i>FX-35: Distribution of kinetic energy by mode. Even at a neutrally stable condition, the first-torsion mode participates in the flutter response (Mach 0.93, density 0.079 kg/m³).</i>	70
6.20	<i>FX-35: Stable plunge response below the flutter boundary (Mach 0.93, density 0.05 kg/m³).</i>	71

6.21	<i>FX-35: Stable pitch response below the flutter boundary (Mach 0.93, density 0.05 kg/m³).</i>	71
6.22	<i>FX-35: Phase plots corresponding to a stable response; the first-torsion mode drops out over time, as evidenced by the transition to a clean sinusoidal decay of the first-bending mode (Mach 0.93, density 0.05 kg/m³).</i>	72
6.23	<i>F-Wing: Strong bending-torsion flutter plunge response, demonstrating rapid amplitude growth at increased density (Mach 0.93, density 0.2 kg/m³).</i>	73
6.24	<i>F-Wing: Strong bending-torsion flutter pitch response, showing first-torsion coupling with the dominant first-bending mode (Mach 0.93, density 0.2 kg/m³).</i>	74
6.25	<i>F-Wing: Phase plots corresponding to strong bending-torsion flutter (Mach 0.93, density 0.2 kg/m³).</i>	74
6.26	<i>F-Wing: Distribution of kinetic energy by mode (Mach 0.93, density 0.2 kg/m³).</i>	75
6.27	<i>F-Wing: Neutrally stable flutter plunge response (Mach 0.93, density 0.13 kg/m³).</i>	76
6.28	<i>F-Wing: Neutrally stable flutter pitch response (Mach 0.93, density 0.13 kg/m³).</i>	76
6.29	<i>F-Wing: Phase plots corresponding a neutrally stable response; the smooth response shows little to no evidence of mode coupling (Mach 0.93, density 0.13 kg/m³).</i>	77
6.30	<i>F-Wing: distribution of kinetic energy by mode, the response is almost purely first-bending (Mach 0.93, density 0.13 kg/m³).</i>	77
6.31	<i>F-Wing: Stable plunge response (Mach 0.93, density 0.05 kg/m³).</i>	78
6.32	<i>F-Wing: Stable pitch response (Mach 0.93, density 0.05 kg/m³).</i>	78
6.33	<i>F-Wing: Phase plots corresponding to a stable response (Mach 0.93, density 0.05 kg/m³).</i>	79
6.34	<i>F-Wing: Distribution of kinetic energy by mode (Mach 0.93, density 0.05 kg/m³).</i>	79

6.35	<i>Indication of the Chimney Transition free stream Mach number range.</i>	81
6.36	<i>FX-35: Steady state plunge asymptotically approaching zero (Mach 0.95, density 0.03 kg/m³).</i>	83
6.37	<i>FX-35: Steady state pitch asymptotically approaching zero (Mach 0.95, density 0.03 kg/m³).</i>	83
6.38	<i>FX-35: Steady state plunge transitioning to a neutrally stable second-bending mode (Mach 0.96, density 0.04 kg/m³).</i>	84
6.39	<i>FX-35: Steady state pitch transitioning to a neutrally stable second-bending mode (Mach 0.96, density 0.04 kg/m³).</i>	84
6.40	<i>FX-35: Plunge (left) and pitch (right) chimney region LCO transitions for Mach 0.96 through Mach 0.99 at low density (0.05 kg/m³ or lower).</i>	85
6.41	<i>FX-35: Lifetime phase plots for a first-bending to second-bending chimney transition (Mach 0.96, density 0.04 kg/m³).</i>	87
6.42	<i>FX-35: Lifetime (left) and steady state (right) phase plots showing similar chimney characteristics prior to the chimney region (Mach 0.95, density 0.03 kg/m³).</i>	88
6.43	<i>FX-35: Steady state chimney response phase plots over a subset of oscillations showing a well defined pattern of second-bending motion (Mach 0.96, density 0.04 kg/m³).</i>	89
6.44	<i>FX-35: Distribution of kinetic energy by mode in the chimney, showing dominant second-bending motion (Mach 0.96, density 0.04 kg/m³).</i>	89
6.45	<i>FX-35: Steady state chimney response phase plots over a subset of oscillations showing the beginnings of multi-mode influence (Mach 0.97, density 0.04 kg/m³).</i>	90

6.46	<i>FX-35: Distribution of kinetic energy by mode in the chimney, showing dominant second-bending motion (Mach 0.97, density 0.04 kg/m³).</i>	90
6.47	<i>FX-35: Steady state chimney response phase plots over a subset of oscillations showing the influence of other modes on the second-bending pattern (Mach 0.98, density 0.02 kg/m³).</i>	91
6.48	<i>FX-35: Distribution of kinetic energy by mode in the chimney, showing dominant second-bending motion and unexpected participation from additional modes beyond the first four (Mach 0.98, density 0.02 kg/m³).</i>	91
6.49	<i>F-Wing: Steady state plunge asymptotically approaching zero prior to the chimney boundary (Mach 0.94, density 0.05 kg/m³).</i>	93
6.50	<i>F-Wing: Steady state pitch asymptotically approaching zero prior to the chimney boundary (Mach 0.94, density 0.05 kg/m³).</i>	93
6.51	<i>F-Wing: Steady state plunge transitioning to a neutrally stable coupled first-torsion and second-bending response after the chimney boundary (Mach 0.94, density 0.05 kg/m³).</i>	94
6.52	<i>F-Wing: Steady state pitch transitioning to a neutrally stable coupled first-torsion and second-bending response after the chimney boundary (Mach 0.94, density 0.05 kg/m³).</i>	94
6.53	<i>F-Wing: Plunge (left) and pitch (right) chimney transitions for Mach 0.95 through Mach 0.98.</i>	95
6.54	<i>F-Wing: Complete lifetime phase plots prior to the chimney transition (Mach 0.94, density 0.05 kg/m³).</i>	96

6.55	<i>F-Wing: Complete lifetime phase plots just after the chimney transition, showing the phase reversal between wing tip pitch and plunge associated with the switch from first-bending to second-bending (Mach 0.95, density 0.05 kg/m³).</i>	97
6.56	<i>F-Wing: Steady state chimney response phase plots over a subset of oscillations showing the well defined pattern of motion (Mach 0.95, density 0.05 kg/m³).</i>	99
6.57	<i>F-Wing: Distribution of kinetic energy by mode in the chimney, showing dominant second-bending motion (Mach 0.95, density 0.05 kg/m³).</i>	99
6.58	<i>F-Wing: Steady state chimney response phase plots for the F-Wing over a subset of oscillations showing a transition to wandering phase behavior (Mach 0.96, density 0.05 kg/m³).</i>	100
6.59	<i>F-Wing: Distribution of kinetic energy by mode in the chimney, showing an increase in first-torsion (Mach 0.96, density 0.05 kg/m³).</i>	100
6.60	<i>F-Wing: Steady state chimney response phase plots for the F-Wing over a subset of oscillations showing a complex pattern that sweeps out a slightly different space with each cycle (Mach 0.97, density 0.04 kg/m³).</i>	101
6.61	<i>F-Wing: Distribution of kinetic energy by mode in the chimney, showing the addition of first-bending for a three mode response (Mach 0.97, density 0.04 kg/m³).</i>	101
6.62	<i>F-Wing: Steady state chimney response phase plots for the F-Wing over a subset of oscillations revealing erratic behavior due the cacophony of mode interactions (Mach 0.98, density 0.02 kg/m³).</i>	102
6.63	<i>F-Wing: Distribution of kinetic energy by mode in the chimney, showing how established patterns begin to break down on approach to Mach one (Mach 0.98, density 0.02 kg/m³).</i>	102

6.64	<i>Indication of the Mach Freeze region free stream Mach number range.</i>	103
6.65	<i>FX-35: Plunge (left) and pitch (right) responses for Mach 0.97 through Mach 1.00 (density 0.2 kg/m³) showing the quenching effect of the Mach number freeze starting around Mach 0.99.</i>	105
6.66	<i>FX-35: Neutrally stable plunge response just after the Mach freeze (Mach 1.00, density 0.2 kg/m³).</i>	107
6.67	<i>FX-35: Neutrally stable pitch response just after the Mach freeze (Mach 1.00, density 0.2 kg/m³).</i>	107
6.68	<i>FX-35: Mach freeze phase plots showing the complex patterns resulting from a multi-mode response (Mach 1.00, density 0.2 kg/m³).</i>	108
6.69	<i>FX-35: Distribution of kinetic energy across natural modes, highlighting the interplay of modes responsible for complex responses seen after the Mach freeze (Mach 1.00, density 0.2 kg/m³).</i>	108
6.70	<i>FX-35: A more subdued neutrally stable plunge response just after the Mach freeze (Mach 1.00, density 0.1 kg/m³).</i>	109
6.71	<i>FX-35: A more subdued neutrally stable pitch response just after the Mach freeze (Mach 1.00, density 0.1 kg/m³).</i>	110
6.72	<i>FX-35: Mach freeze phase plots showing the smearing effect of the first-bending and second-bending mode interaction (Mach 1.00, density 0.1 kg/m³).</i>	110
6.73	<i>FX-35 distribution of kinetic energy across natural modes, revealing a tug of war between first-bending and second-bending (Mach 1.00, density 0.1 kg/m³).</i>	111
6.74	<i>FX-35: Neutrally stable plunge response just after the Mach freeze, which is slowed down by the decreased density (Mach 1.00, density 0.05 kg/m³).</i>	112

6.75	<i>FX-35: Neutrally stable pitch response just after the Mach freeze, which is slowed down by the decreased density (Mach 1.00, density 0.05 kg/m³).</i>	112
6.76	<i>FX-35: Mach freeze phase plots showing the smearing effect of the first-bending and second-bending mode interaction (Mach 1.00, density 0.05 kg/m³).</i>	113
6.77	<i>FX-35: Distribution of kinetic energy across natural modes; neither of the modes present appear to be taking control of the response (Mach 1.00, density 0.05 kg/m³).</i>	113
6.78	<i>FX-35: Neutrally stable plunge response in the Mach freeze region; modes besides first-bending begin to drop off as Mach number increases (Mach 1.03, density 0.2 kg/m³).</i>	115
6.79	<i>FX-35: Neutrally stable pitch response in the Mach freeze region; modes besides first-bending begin to drop off as Mach number increases (Mach 1.03, density 0.2 kg/m³).</i>	115
6.80	<i>FX-35: Mach freeze region phase plots showing the decreasing participation of second-bending (Mach 1.03, density 0.2 kg/m³).</i>	116
6.81	<i>FX-35: Distribution of kinetic energy across natural modes over time (Mach 1.03, density 0.2 kg/m³).</i>	116
6.82	<i>FX-35: Neutrally stable plunge response in the Mach freeze region (Mach 1.05, density 0.2 kg/m³).</i>	117
6.83	<i>FX-35: Neutrally stable pitch response in the Mach freeze region (Mach 1.05, density 0.2 kg/m³).</i>	117
6.84	<i>FX-35: Mach freeze region phase plots showing a return to pure first-bending patterns at higher Mach number (Mach 1.05, density 0.2 kg/m³).</i>	118

6.85	<i>FX-35: Distribution of kinetic energy across natural modes over time (Mach 1.05, density 0.2 kg/m³).</i>	118
6.86	<i>FX-35: Neutrally stable plunge response in the Mach freeze region (Mach 1.04, density 0.05 kg/m³).</i>	119
6.87	<i>FX-35: Neutrally stable pitch response in the Mach freeze region (Mach 1.04, density 0.05 kg/m³).</i>	119
6.88	<i>FX-35: Mach freeze region phase plots showing a return to pure first-bending patterns at higher Mach number (Mach 1.04, density 0.05 kg/m³).</i>	120
6.89	<i>FX-35: Distribution of kinetic energy across natural modes over time (Mach 1.04, density 0.05 kg/m³).</i>	120
6.90	<i>F-Wing: Plunge (left) and pitch (right) responses for Mach 0.98 through Mach 1.01 (density 0.2 kg/m³) showing the tempering effect of the Mach number freeze starting around Mach 1.00.</i>	122
6.91	<i>F-Wing: Weakly unstable plunge response in the Mach freeze region (Mach 1.00, density 0.02 kg/m³).</i>	124
6.92	<i>F-Wing: Distribution of kinetic energy across natural modes over time (Mach 1.00, density 0.02 kg/m³).</i>	124
6.93	<i>F-Wing: Unstable plunge response in the Mach freeze region (Mach 1.00, density 0.15 kg/m³).</i>	125
6.94	<i>F-Wing: Unstable pitch response in the Mach freeze region (Mach 1.00, density 0.15 kg/m³).</i>	125
6.95	<i>F-Wing: Mach freeze region phase plots showing erratic patterns as first-bending and second-bending interact (Mach 1.00, density 0.15 kg/m³).</i>	126

6.96	<i>F-Wing: Distribution of kinetic energy across natural modes over time (Mach 1.00, density 0.15 kg/m³).</i>	126
6.97	<i>F-Wing: Neutrally stable plunge response in the Mach freeze region (Mach 1.03, density 0.05 kg/m³).</i>	128
6.98	<i>F-Wing: Neutrally stable pitch response in the Mach freeze region (Mach 1.03, density 0.05 kg/m³).</i>	128
6.99	<i>F-Wing: Mach freeze region phase plots showing essentially single degree-of-freedom first-bending patterns at higher Mach number (Mach 1.03, density 0.05 kg/m³).</i>	129
6.100	<i>F-Wing: Distribution of kinetic energy across natural modes over time (Mach 1.03, density 0.05 kg/m³).</i>	129
6.101	<i>F-Wing: Unstable plunge response in the Mach freeze region (Mach 1.02, density 0.2 kg/m³).</i>	130
6.102	<i>F-Wing: Unstable pitch response in the Mach freeze region (Mach 1.02, density 0.2 kg/m³).</i>	130
6.103	<i>F-Wing: Mach freeze region phase plots showing a transition to bending-torsion flutter (Mach 1.02, density 0.2 kg/m³).</i>	131
6.104	<i>F-Wing: Distribution of kinetic energy across natural modes over time (Mach 1.02, density 0.2 kg/m³).</i>	131

List of Tables

6.1	<i>Wing planform parameters for the FX-35 and F-Wing.</i>	51
6.2	<i>The first four natural frequencies (Hz) of the FX-35 for the standard atmospheric and modified TDT models ($t =$ plate thickness).</i>	53
6.3	<i>The first four natural frequencies (Hz) of the F-Wing for the standard atmospheric and modified TDT models ($t =$ plate thickness).</i>	54

Nomenclature

δ_{ij}	Kronecker Delta
γ	Ratio of specific heats in the fluid
\mathbf{D}_i	Dissipative flux vector in the discretized fluid system
\mathbf{F}	Flux vector of conserved fluid quantities
\mathbf{m}_{ij}	Consistent mass matrix in the discretized fluid system
\mathbf{n}	Outward surface unit normal vector
\mathbf{Q}_i	Flux vector in the discretized fluid system
\mathbf{R}_{ij}	Vector from node i to node j in a structural element
\mathbf{U}	Fluid mesh velocity vector with components U_1 , U_2 , and U_3
\mathbf{u}	Fluid velocity vector with components u_1 , u_2 , and u_3
\mathbf{W}	Vector of conserved fluid quantities
\mathbf{W}_j	Nodal values of \mathbf{W} in the discretized fluid system
Ω	Fluid control volume
$\partial\Omega$	Boundary of fluid control volume
ϕ_j	Linear shape functions in the discretized fluid system
ρ	Fluid density
σ_{ij}	Cartesian stress tensor
a	Speed of sound
e	Total energy per unit mass
p	Fluid pressure
R	Riemann invariant

t Time

x, y, z Global coordinates (Eulerian)

x', y', z' Local coordinates (Lagrangian)

ACKNOWLEDGMENTS

The difficulty of this task did not lie in its scale or complexity, because their full extent was veiled by my novice. It was uncertainty because of inexperience that most often barred the way, and that could not have been overcome without the encouragement and patience of friends, family, and mentors.

Thank you Professor Bendiksen for providing guidance and for bearing through my mistakes. You have given me the space to work out solutions in my own way, and taken the time to correct my course when those solutions failed. The more I learn, the more impressed I am with the depth and breadth of knowledge my professors keep at their disposal. It is the reward for years of experience and hard work, and I'm grateful that you have allowed me to share in it.

Thank you as well to my committee, Professors Zhong, Taciroglu, and Klug for their assistance with this dissertation and for asking the hard questions.

I want to thank my friends and family for the countless hours they have spent listening to me talk about my research and reassuring me that, at the very least, I sound like I know what I'm talking about.

Most of all I want to thank my parents for everything they have done for me. They are steadfast in their love, unwavering in their support, and have never doubted me for a moment. They also let me move back in with them so I wouldn't be homeless while I wrote this.

This research was supported by AFOSR Contract FA9550-13-C-0016 through a subcontract from Creative Aero Engineering Solutions, Long Beach, CA.

VITA

2009 - B.S. (Mathematics), B.S. (Physics), Azusa Pacific University, Azusa, California.

2011 - M.S. (Aerospace Engineering), University of California Los Angeles, Los Angeles,
California.

Chapter 1

Introduction

1.1 Motivation for Research

The development of advanced modern aircraft comes with the expectation of improved performance in all flight regimes. This has led to the increased use of highly flexible wing structures that are subject to large deformations [1, 2, 3]. Unfortunately, the large dynamic forces created by supersonic pockets and normal shocks in the transonic flight regime make these wings susceptible to dangerous aeroelastic instabilities [4, 5, 6]. A better understanding of the physics behind the problem and more accurate solutions are necessary to predict and mitigate potential problems during the design of the aircraft [7]. While traditional wind tunnel tests provide valuable data about transonic flows, the behavior they seek to capture also runs the risk of destroying the model and damaging the tunnel [8]. Numerical simulations of transonic aeroelastic problems have the potential to make future designs safer, to make testing cheaper, and to provide a better understanding of the underlying physics behind transonic phenomena.

The primary difficulty of numerical simulations is capturing the nuances of the behavior of the wing without creating too heavy a burden in terms of computation. While there are many schools of thought on what kinds of shortcuts can be taken in the interest of saving time, it has been shown that a nonlinear structural implementation and a direct, element-level coupling scheme between structure and fluid are necessary to obtain an accurate solution [9, 10, 11].

The purpose of this research is twofold. First, the methods discussed in this paper, from the work of Hwang and Seber [12, 13], are put to further test on current and next-generation fighter wing planforms for high-altitude flows. These results will form the basis for wind tunnel model tuned to exhibit rich flutter behavior. Second, improvements will be made to the overall function of the computational program to deliver results faster.

1.2 Literature Review

1.2.1 Transonic Aeroelastic Computation

The history of transonic computation is largely that simplifications of the model yield unacceptable errors when compared to real-world results. To some extent, this is true of every computational model. Improvements are always done incrementally through the addition of complexity, but the path to success with the transonic flow regime is an especially long one. The two largest barriers to advancement have been the proper integration of the structural problem with the fluid one and, of course, computational power.

The first forays into transonic computational fluid dynamics were made by a number

of different researchers in the 1970s using potential flow models. They began with a two-dimensional steady flow based on transonic small disturbance theory [14], followed by a three-dimensional steady flow [15], and finally two-dimensional [16] and three-dimensional [17] unsteady flows. These models were extended to include dynamic structural motion through a normal modes method [18, 19, 20], and so yielded the first flutter analyses. However, the limitations of potential flow theory with regards to shock formation and the small disturbance assumption meant that results from these programs could never meet the full demands of modern aircraft design.

In the mid 1980s, increases in computational power allowed researchers to begin using the Euler and Navier-Stokes equations in transonic computation. In 1985, Venkatakrisnan and Jameson [21] made a two-dimensional unsteady Euler flow with a moving airfoil. They were followed by an aeroelastic two-dimensional Euler solver by Bendiksen and Kousen [22, 23], which employed a tangent flow boundary condition at the airfoil surface. At the same time, Wu [24, 25] developed similar flutter programs using the two-dimensional compressible unsteady Navier-Stokes equations. Finally, Guruswamy extended the Euler [26] and Navier-Stokes [27, 28, 29] equations to unsteady three-dimensional flutter analysis of plate finite element wings. Other notable works include three-dimensional Euler [30, 31] and Navier-Stokes [32] applications to highly swept wings, which used a moving fluid mesh algorithm [33] based on a spring-connected analogy.

All aeroelastic programs have to contend with how to combine computational fluid dynamics with finite element structural mechanics. The traditional method of coupling the interface between the fluid and the structure is to treat them as two separate problems with a shared boundary. On the fluid side, the position and velocity of the interface is needed to

enforce boundary conditions, while on the structural side the flow conditions at the interface are needed to solve the surface pressure for the global forces. Both domains require information from the boundary, but the boundary itself is not strictly known. This means some amount of estimation is needed at each time step, either in surface pressure or the boundary location, and errors will inevitably result.

An alternative formulation of fluid-structure coupling was presented by Bendiksen [9], and eventually implemented as the Direct Eulerian-Lagrangian method [34]. This method attaches a local (Lagrangian) coordinate system to the fluid nodes that form the wing surface, which is the fluid-structure interface, and attaches that surface directly to the wing structure using area coordinates. This allows the interface to move with the wing structure directly, so that the position and velocity of each element forming the wing surface interface is known at all times. Additionally, since the transformations between the local and global coordinates are known, the local (Lagrangian) fluid forces can be compiled into the force balance equations in the global (Eulerian) coordinate system. The remaining fluid nodes in the interior are allowed to move in accordance with wing surface interface. This allows the model to be treated as a continuum, and assumptions with regard to the wing boundary are not required. The quantitative difference when compared to the traditional approach is that the work done by the fluid on the wing and the total wing energy (strain plus kinetic) are equal for the Direct Eulerian-Lagrangian method, whereas classical methods showed a difference in energy and work over time.

1.2.2 Transonic Flutter Phenomena

The Direct-Eulerian Lagrangian method has proven useful at capturing a number of transonic flutter phenomena observed during wind-tunnel testing. This includes neutrally stable and weakly unstable limit-cycle oscillation (LCO) type flutter, dynamic-pressure independent chimneys of LCO flutter near sonic conditions, strongly stabilizing Mach number freeze effects close to the speed of sound, and essentially single degree of freedom (ESDOF) flutter responses.

LCO flutter in the transonic region has been shown to be an inherently nonlinear problem [23, 35, 36, 37, 38, 39], but it is also sensitive to the treatment of the wing surface boundary. Nonlinear von Karman plate models overestimate the stiffness of the wing and achieve only mixed success at LCO prediction [37, 39]. To capture the full range of LCO behavior present in the transonic region, the wing boundary must be modeled without approximation as in the Direct Eulerian-Lagrangian formulation [9].

The most interesting phenomenon is the transonic dip or LCO chimney in highly flexible wings as observed in the cranked delta wing by NASA [8] and the arrow wing by JAXA [40]. The chimney is characterized by a narrow vertical band of Mach numbers where LCO flutter instabilities persist down to, and presumably below, the possible dynamic pressure of the wind tunnel. Chimneys also coincide with the Mach number freeze region, which corresponds to the arrival of the normal shock at the trailing-edge of the wing. Just before the Mach freeze, unsteady aerodynamic forces rapidly reverse amplitude and phase, triggering LCOs characterized by the wing's natural modes. At a slightly higher Mach number, the predominant instabilities are snuffed out, but weakly unstable LCOs persist as a chimney

[41].

The Direct Eulerian-Lagrangian Method was recently used by Mellquist [42] to reproduce LCO chimney behavior for a cranked wing similar to the one used in the JAXA study [40]. The study also found evidence of the Mach freeze phenomenon, which stabilizes the flutter response near Mach one, as well as single degree-of-freedom LCOs in the supersonic region.

1.3 Problem Statement and Research Objectives

Computational solutions are the undeniable future of research and design in every major field of study. However, without validation by wind tunnel results, a computational model has no merit or function. Even then, it is not good enough just to reproduce a known outcome, the model must be able to predict what will happen beforehand. An opportunity to do just that has presented itself. The Direct Eulerian-Lagrangian Method will be used to predict a fighter aircraft wing model to undergo wind tunnel testing for flutter behavior. It's not that fighter wings haven't undergone transonic wind tunnel tests, it's just that the results are classified.

The objective of this research is to improve the functionality of the code, design a fighter aircraft wing planform that will exhibit rich flutter behavior under specified tunnel conditions, and predict the flutter results of that particular model. The computational results obtained here have a direct impact on the model that will be built in the future. Current objectives will be accomplished by the following:

1. Improve the functionality of the code by decreasing computational runtime through parallelization.

2. Adjust structural parameters of the wing planform to optimize the number of interesting flutter cases that can be reproduced within the constraints of the wind tunnel operating limits.
3. Identify as closely as possible the transition points between observable types of flutter within the wind tunnel test matrix.

1.4 Dissertation Outline

Immediately following this introduction, Chapter 2 discusses the formulation of the fluid model and the fluid mesh generation. Chapter 3 details the nonlinear structural model and Chapter 4 explains the coupling approach between the fluid and structure using the Direct Eulerian-Lagrangian method. Chapter 5 contains the methods used to parallelize the computational domain, along with performance benchmarks and the verification of the result against the serial method. Computational flutter results are given in Chapter 6, which compare and contrast the various flutter behaviors that are typical of the FX-35 and F-Wing planforms. Conclusions and ideas for future research are presented in Chapter 7.

Chapter 2

Fluid Model

2.1 Introduction

This chapter deals with the fluid dynamic theory and computational methods used to handle the flow field of the model. The fluid domain is comprised of an unstructured tetrahedral mesh and a nonlinear implementation of the Euler equations. Since the model is aeroelastic, it helps if the fluid mesh is allowed to move with the structural mesh. For this reason, a mixed Lagrangian-Eulerian formulation is used. The fluid flow and the fluid mesh are both in motion relative to the fixed frame and relative to each other, which is reflected in the formulation of the governing equations and the boundary conditions. This fluid model is based on the model developed by Bendiksen et al. [10, 11, 34, 43, 44, 12, 13, 45, 46]

The interface between the structural mesh and the fluid mesh at the wing surface boundary is coupled using the Direct Eulerian-Lagrangian method. The details of the coupling will be covered in Chapter 4. Briefly, the formulation allows the motion of the structure and the fluid at the wing surface boundary to be solved together in an element-by-element

manner. The solution does not require normal or assumed modes for the structure and both meshes are integrated in the same time step. The main steps of this approach are illustrated in Figure 2.1.

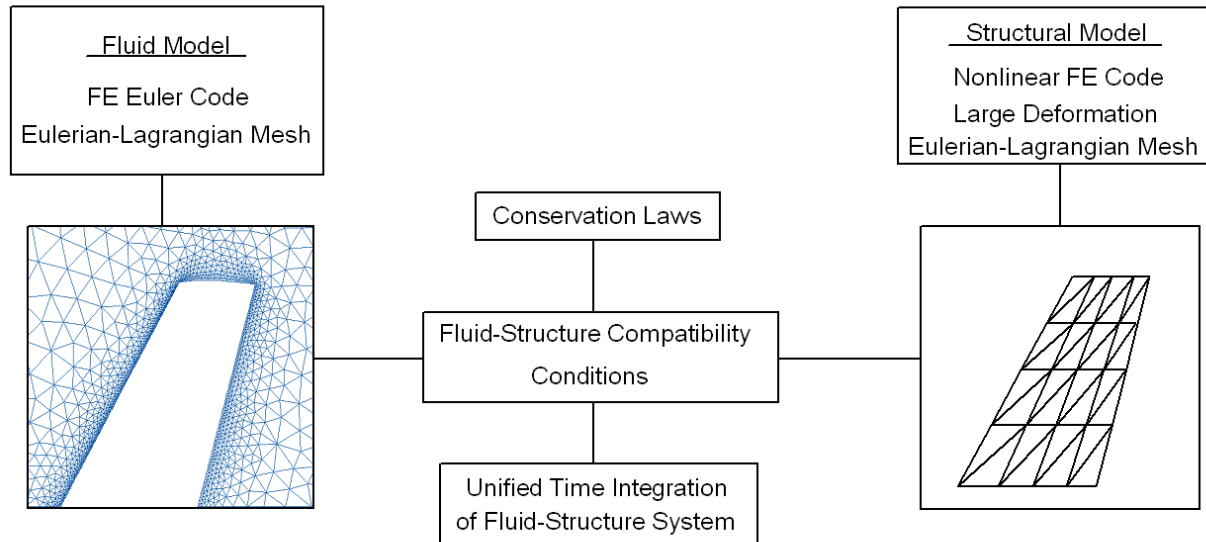


Figure 2.1: *The Direct Eulerian-Lagrangian computational approach to fluid-structure interaction.*

2.2 Governing Equations and Discretization

The fluid domain is governed by the integral form of the conservation laws,

$$\frac{\partial}{\partial t} \int_{\Omega} \mathbf{W} dV + \int_{\partial\Omega} \mathbf{F} \cdot \mathbf{n} dS = 0 \quad (2.1)$$

where Ω is the control volume of a fluid cell, $\partial\Omega$ is the control volume boundary moving with velocity \mathbf{U} , $\mathbf{n} = n_i \hat{\mathbf{e}}_i$ is the outward unit normal, $\hat{\mathbf{e}}_i$ are unit vectors, and

$$\mathbf{W} = \begin{bmatrix} \rho \\ \rho u_1 \\ \rho u_2 \\ \rho u_3 \\ \rho e \end{bmatrix} \quad (2.2)$$

$$\mathbf{F} = \mathbf{F}_j \hat{\mathbf{e}}_j, \quad \mathbf{F}_j = \begin{bmatrix} \rho(u_j - U_j) \\ \rho u_1(u_j - U_j) - \sigma_{1j} \\ \rho u_2(u_j - U_j) - \sigma_{2j} \\ \rho u_3(u_j - U_j) - \sigma_{3j} \\ \rho e(u_j - U_j) - \sigma_{ij} u_i \end{bmatrix} \quad (2.3)$$

\mathbf{W} is the vector of conserved fluid quantities (mass, momentum, and energy), where ρ is the fluid density, \mathbf{u} is the fluid velocity vector, and e is the total energy per unit mass. \mathbf{F} is the flux vector of conserved fluid quantities, where σ_{ij} is the Cartesian stress tensor, u_j and U_j are the Cartesian components of \mathbf{u} and \mathbf{U} , and body forces are neglected. Equation 2.1 represents conservation of mass, conservation of momentum in three dimensions, and conservation of energy.

Viscosity is ignored and the stress tensor can be simplified as a function of pressure.

$$\sigma_{ij} = -p\delta_{ij} \quad (2.4)$$

Pressure can be eliminated by rewriting the perfect gas equation in terms total energy per unit mass.

$$p = \rho(\gamma - 1)\left(e - \frac{1}{2}u_i u_i\right) \quad (2.5)$$

The discretization of the Equation 2.1 is achieved through a Galerkin finite element method. The governing equations are multiplied by an admissible test function and then integrated. In the case of the tetrahedral fluid elements, shape functions can be formed from the combination of four volume coordinates.

$$\mathbf{W}(x_1, x_2, x_3, t) = \sum_j \mathbf{W}_j \phi_j(x_1, x_2, x_3, t) \quad (2.6)$$

Here, \mathbf{W}_j are nodal values of \mathbf{W} and ϕ_j are linear shape functions that depend on both time and space. Substituting Equation 2.6 into the Galerkin form of Equation 2.1 yields,

$$\frac{\partial}{\partial t} \int_{\Omega} \mathbf{W} \phi_i dV + \int_{\Omega} \phi_i \nabla \cdot \mathbf{F} dV \quad (2.7)$$

The final discretized form of the equation is created by numerically evaluating integrals through Gaussian integration and adding a dissipation function.

$$\frac{d}{dt} \sum_j \mathbf{m}_{ij} \mathbf{W}_{ij} + \mathbf{Q}_i - \mathbf{D}_i = 0 \quad (2.8)$$

Here, i represents a single node and j is the summation over only those nodes adjacent to i . Additionally, \mathbf{m}_{ij} is the consistent mass matrix, \mathbf{Q}_i is the flux vector, and \mathbf{D}_i are dissipative fluxes of the Jameson-Mavriplis type [47, 48], here used in a modified form [12, 49].

2.3 Five-Stage Runge-Kutta Scheme

A five-stage Runge-Kutta scheme is used to integrate Equation 2.8. The scheme is shown in Equation 2.9.

$$\begin{aligned}
\mathbf{W}^{(0)} &= \mathbf{W}^{[n]} \\
\mathbf{W}^{(1)} &= [\mathbf{M}]^{-1} \left(\mathbf{M}^{(0)} \mathbf{W}^{(0)} - \alpha_1 \Delta t \left[\mathbf{Q} \left(\mathbf{W}^{(0)} \right) - \mathbf{D} \left(\mathbf{W}^{(0)} \right) \right] \right) \\
\mathbf{W}^{(2)} &= [\mathbf{M}]^{-1} \left(\mathbf{M}^{(0)} \mathbf{W}^{(0)} - \alpha_2 \Delta t \left[\mathbf{Q} \left(\mathbf{W}^{(1)} \right) - \mathbf{D} \left(\mathbf{W}^{(1)} \right) \right] \right) \\
\mathbf{W}^{(3)} &= [\mathbf{M}]^{-1} \left(\mathbf{M}^{(0)} \mathbf{W}^{(0)} - \alpha_3 \Delta t \left[\mathbf{Q} \left(\mathbf{W}^{(2)} \right) - \mathbf{D} \left(\mathbf{W}^{(1)} \right) \right] \right) \\
\mathbf{W}^{(4)} &= [\mathbf{M}]^{-1} \left(\mathbf{M}^{(0)} \mathbf{W}^{(0)} - \alpha_4 \Delta t \left[\mathbf{Q} \left(\mathbf{W}^{(3)} \right) - \mathbf{D} \left(\mathbf{W}^{(1)} \right) \right] \right) \\
\mathbf{W}^{(5)} &= [\mathbf{M}]^{-1} \left(\mathbf{M}^{(0)} \mathbf{W}^{(0)} - \alpha_5 \Delta t \left[\mathbf{Q} \left(\mathbf{W}^{(4)} \right) - \mathbf{D} \left(\mathbf{W}^{(1)} \right) \right] \right) \\
\mathbf{W}^{[n+1]} &= \mathbf{W}^{(5)}
\end{aligned} \tag{2.9}$$

where α_i for $i = 1, 2, 3, 4, 5$ are $\frac{1}{4}, \frac{1}{6}, \frac{3}{8}, \frac{1}{2}, 1$ respectively and Δt is the time step. Superscripts in parentheses refer to the Runge-Kutta stage, and superscripts in brackets refer to the global time-marching step number. Dissipative terms are only evaluated in the first two stages to save computational time.

The time step, Δt_i^* , is calculated as the local minimum time for a wave to propagate between a chosen node, i , to adjacent nodes, $k = 1, 2, \dots, n$, where n is the number of adjacent nodes.

$$\Delta t_i^* = \min(\Delta t_{ik}), \forall k \text{ adjacent to node } i \tag{2.10a}$$

$$\Delta t_{ik} = \frac{\Delta \mathbf{x} \cdot \Delta \mathbf{x}}{\left| (\bar{u} - \bar{U}) \cdot \Delta \mathbf{x} \right| + \bar{a} |\Delta \mathbf{x}|} \tag{2.10b}$$

$$\Delta \mathbf{x} = (x_k - x_i) \hat{\mathbf{e}}_x + (y_k - y_i) \hat{\mathbf{e}}_y + (z_k - z_i) \hat{\mathbf{e}}_z \tag{2.10c}$$

Where \hat{u} , \hat{U} , and \hat{a} are the mean flow velocity, mesh velocity, and speed of sound between nodes i and k . The entire domain must proceed at the same global time step, Δt^* , calculated from Equation 2.10a. The explicit Runge-Kutta method described here must be bounded by the Courant-Friederich-Lewy (CFL) number, λ , in order to be numerically stable.

$$\Delta t^* = \min(\Delta t_i^*), \forall \text{ nodes } i \quad (2.11a)$$

$$\Delta t \leq \lambda \Delta t^* \quad (2.11b)$$

2.4 Boundary Conditions

The fluid model encounters four distinct boundaries: The upstream far-field, the downstream far-field, fixed tunnel walls, and the moving wing surface. Each necessitates the addition of an appropriate boundary condition.

On the fixed tunnel walls the mesh velocity is zero and the corresponding boundary condition is given by

$$\mathbf{u} \cdot \mathbf{n} = 0 \quad (2.12)$$

where \mathbf{u} is the fluid velocity vector and \mathbf{n} is the normal vector of the wall surface.

At the wing surface the fluid mesh and structural mesh move together. The resulting boundary condition is

$$(\mathbf{u} - \mathbf{U}) \cdot \mathbf{n} = 0 \quad (2.13)$$

where \mathbf{U} is the fluid mesh velocity vector.

At the far-field boundaries, non-reflective boundary conditions are chosen to minimize the reflection of outgoing disturbances [47]. Assuming the flow is locally one-dimensional,

the incoming Riemann invariant, R_∞ , can be found using the free stream flow conditions, and the outgoing Riemann invariant, R_i , can be calculated by extrapolation from the interior domain.

$$R_\infty = \mathbf{u}_\infty \cdot \mathbf{n} - \frac{2a_\infty}{\gamma - 1} \quad (2.14a)$$

$$R_i = \mathbf{u}_i \cdot \mathbf{n} - \frac{2a_i}{\gamma - 1} \quad (2.14b)$$

The mesh velocity at the far-field boundary is naturally zero, so the normal velocity of the flow and the speed of sound can be calculated as

$$\mathbf{u} \cdot \mathbf{n} = \frac{1}{2}(R_i + R_\infty) \quad (2.15a)$$

$$a = \frac{\gamma - 1}{4}(R_i + R_\infty) \quad (2.15b)$$

Conditions for the tangential velocity and entropy must be provided in order to form a complete definition of the flow at either far-field boundary. For an inflow boundary, tangential flow and entropy are set to their free stream values. At an outflow boundary, they are extrapolated from the interior.

2.5 Mesh Generation

A separate program written by Hwang [12] is responsible for generating the initial fluid mesh. Since the three-dimensional model is aeroelastic and both the structure and fluid increments are solved together in each time step, the fluid mesh must be able to move with the structure under any realistic simulated result. To achieve this, an unstructured mesh is created using the 'Advancing Front Method', in which a unique configuration of nodes is

procedurally generated and tested for suitability.

The tetrahedrons formed by the nodes may experience undesirably large deformations during the course of the simulation, so it is important that their initial shapes are relatively regular. The mesh faces are also assigned positive and negative facing directions that easily allow for unique identification of cells, as well as consistent calculation of signed cell volumes. The latter is an especially important check against nodes punching through an opposing face and creating a negative cell volume.

The finished mesh is rigidly attached to the far field boundaries and the wing surface, with the former having constant spatial coordinates and the latter moving with the wing structural nodes. The remaining interior nodes are allowed to change position and velocity and are modeled as a spring-connected web. New interior node locations are computed using an iterative spring-equilibrium method with forward-substitution [12].

Chapter 3

Nonlinear Structural Model

3.1 Introduction

This chapter contains information about the nonlinear structural finite element model. The chosen theories for element components and numerical solution methods are intended to capture as accurately as possible the characteristics of physical test wings without being overly cumbersome in terms of required computational power. The nonlinear model presented here was developed by Seber [13].

3.2 Structural Model

The purpose of this model is to predict the behavior of physical models in wind-tunnel conditions. As such, each structural component is designed to mimic some aspect of the behavior of its real world counterpart. A typical physical model is first created using a thin flexible aluminum plate, which dominates the structural response during testing. Covering

this plate is a lightweight balsa wood shell that captures the shape of the airfoil and creates realistic aerodynamic conditions.

Accordingly, the computational model is comprised of a plane of structural nodes and a "wing surface layer" of fluid mesh nodes, which represent the metal plate and the airfoil shell respectively. The structural mesh is responsible for recreating the kinematic response seen in a physical test wing. The aerodynamic forces are modeled by rigidly attaching the innermost layer of the fluid mesh to the structure in the shape of the airfoil. The details of the coupling mechanics at the fluid-structure interface will be discussed in Chapter 4.

3.3 Direct Eulerian-Lagrangian Formulation

This program uses the Direct Eulerian-Lagrangian Formulation to handle the motion of the structural mesh and the wing surface nodes. The time marching integration of the dynamics is done element-by-element, with solutions to the mesh motion being found directly at the element level. The 'Eulerian-Lagrangian' naming of the formulation is due to the methods used to keep track of the individual positions of the triangular structural elements. Each element has a spatial position and orientation in two coordinate systems as shown in Figure 3.1.

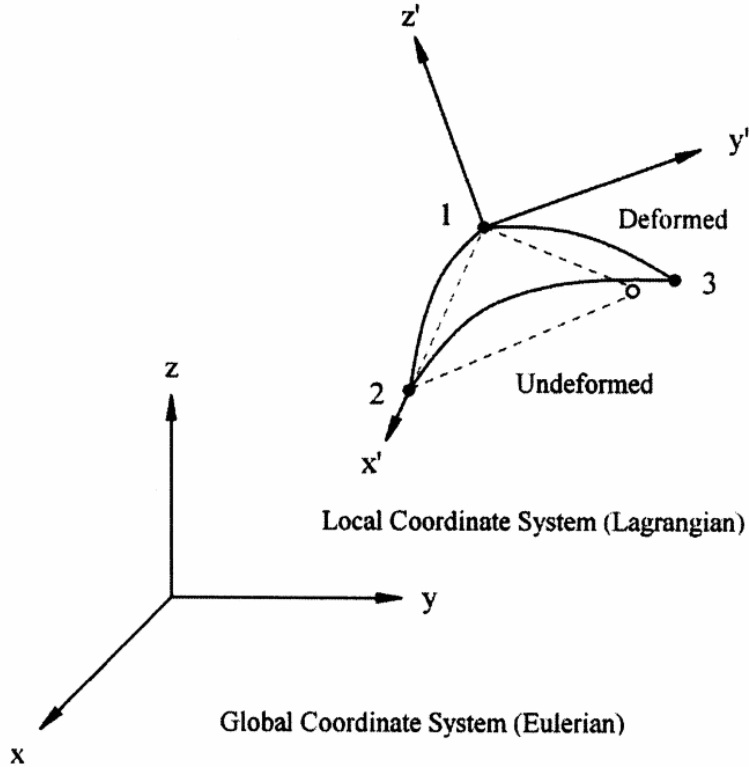


Figure 3.1: *The Eulerian-Lagrangian Formualtion.*

The first is a global Eulerian coordinate system (denoted by x , y , and z axes) that is common to every element in the model. The second is a locally attached Lagrangian coordinate system (denoted by x' , y' , and z' axes) with a known cosine rotation transformation to the global Eulerian coordinate system. Each element has its own unique Lagrangian coordinates that move with that element as it deforms.

The specific definition of the local Lagrangian coordinate system is based on the identities of the nodes forming the triangular element. The three nodes comprising a given element are numbered one through three when the mesh is initially generated, and that numbering is reflected in the figures and equations shown here. First, a z' unit vector is defined normal

to the element plane by taking a cross product of vectors between element nodes.

$$\hat{\mathbf{e}}_{z'} = \frac{\mathbf{R}_{21} \times \mathbf{R}_{31}}{|\mathbf{R}_{21} \times \mathbf{R}_{31}|} \quad (3.1)$$

Where \mathbf{R}_{21} and \mathbf{R}_{31} are vectors in the x' - y' plane. These vectors are expressed in the global coordinate system as

$$\mathbf{R}_{21} = (x_2 - x_1)\hat{\mathbf{e}}_x + (y_2 - y_1)\hat{\mathbf{e}}_y + (z_2 - z_1)\hat{\mathbf{e}}_z \quad (3.2a)$$

$$\mathbf{R}_{31} = (x_3 - x_1)\hat{\mathbf{e}}_x + (y_3 - y_1)\hat{\mathbf{e}}_y + (z_3 - z_1)\hat{\mathbf{e}}_z \quad (3.2b)$$

The x' and y' axes can be given any orientation in the plane of the element so long as the formulation is consistent. The x' axis is chosen to rest along the vector connecting nodes 1 and 2 and the corresponding unit vector is given by

$$\hat{\mathbf{e}}_{x'} = \frac{\mathbf{R}_{21}}{|\mathbf{R}_{21}|} \quad (3.3)$$

With the x' and z' axes defined, the y' axis unit vector is calculated from the cross product of the other two.

$$\hat{\mathbf{e}}_{y'} = \hat{\mathbf{e}}_{z'} \times \hat{\mathbf{e}}_{x'} \quad (3.4)$$

Any vector expressed in global coordinates can be rewritten in local coordinates (and vice versa) by means of a cosine rotation matrix.

$$\mathbf{q}^L = [e] \mathbf{q}^G \quad (3.5a)$$

$$[e] = \begin{bmatrix} (e_{x'})_1 & (e_{x'})_2 & (e_{x'})_3 \\ (e_{y'})_1 & (e_{y'})_2 & (e_{y'})_3 \\ (e_{z'})_1 & (e_{z'})_2 & (e_{z'})_3 \end{bmatrix} \quad (3.5b)$$

Where \mathbf{q}^L and \mathbf{q}^G are vectors expressed in local and global coordinates respectively, and $[e]$ is a direction cosine matrix taken from the components of the local unit vectors when expressed in global coordinates.

3.4 Typical Element Formulation

The individual elements in the structural model are a combination of three distinct components, as shown in Figure 3.2.

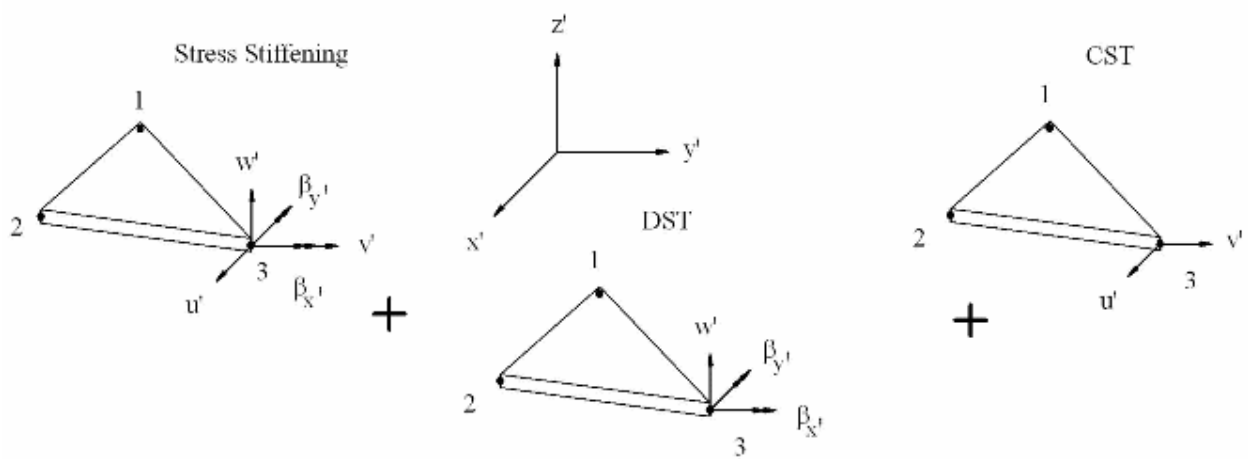


Figure 3.2: Various components of a typical structural element.

3.4.1 Out-of-Plane: Discrete Shear Triangle

The Discrete Shear Triangle (DST) is a Mindlin-Reissner plate finite element designed to model motion occurring transverse to the plane of the wing. Figure 3.3 shows the degrees of freedom associated with this element, which are out-of-plane displacement and out-of-plane rotation about the x and y axes.

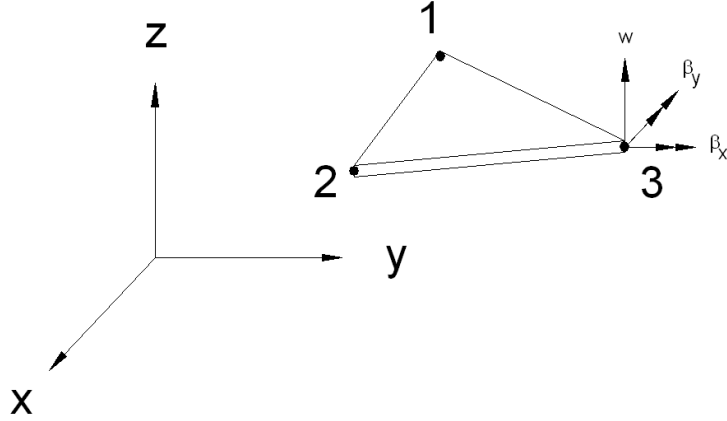


Figure 3.3: *Nodal degrees of freedom for the DST.*

The DST element contributes nine degrees of freedom to the overall formulation.

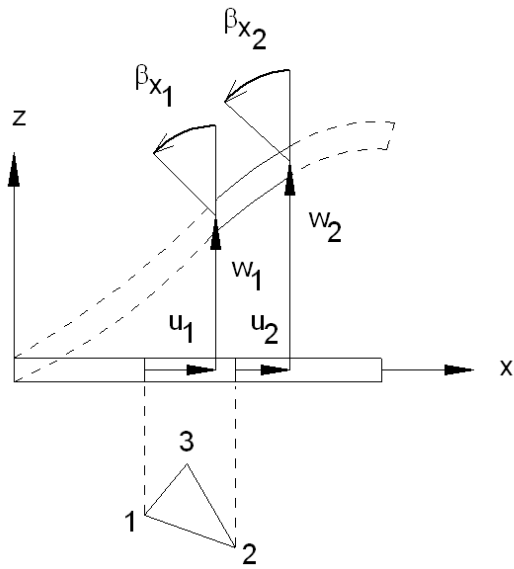
$$\mathbf{q}'_w{}^T = \{ w'_1 \quad \beta_{x'_1} \quad \beta_{y'_1} \quad w'_2 \quad \beta_{x'_2} \quad \beta_{y'_2} \quad w'_3 \quad \beta_{x'_3} \quad \beta_{y'_3} \} \quad (3.6)$$

When described in Lagrangian coordinates the out-of-plane displacements are equal to zero, since the element itself defines the local x-y plane.

$$\mathbf{q}'_w{}^T = \{ 0 \quad \beta_{x'_1} \quad \beta_{y'_1} \quad 0 \quad \beta_{x'_2} \quad \beta_{y'_2} \quad 0 \quad \beta_{x'_3} \quad \beta_{y'_3} \} \quad (3.7)$$

The use of the Eulerian-Lagrangian formulation means that local deformations are not affected by rigid body motion. The inclusion of rigid body motion leads to an overestimation of structural stiffness [50]. Figure 3.4 contrasts the Von Karman and Eulerian-Lagrangian formulation; where in the former rigid body motion contributes to elastic deformation and in the latter it does not.

von Karman Theory



Direct Eulerian-Lagrangian Formulation

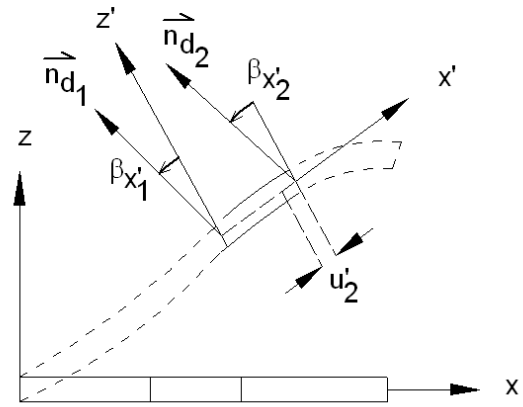


Figure 3.4: *In-plane deformation in Lagrangian coordinates.*

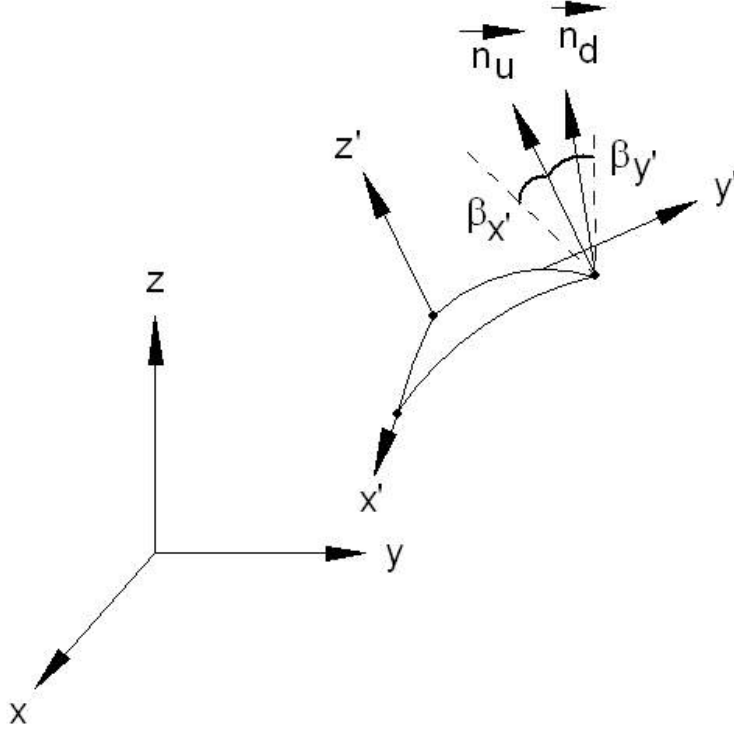


Figure 3.5: *Local out-of-plane deformations.*

Figure 3.5 shows the local out-of-plane rotational deformations, which can be calculated using a finite rotation relation.

$$\mathbf{n}_d^{t^{n+1}} = \cos(\Delta\phi)\mathbf{n}_d^{t^n} + (1 - \cos(\Delta\phi))(\mathbf{n} \cdot \mathbf{n}_d^{t^n})\mathbf{n} + \sin(\Delta\phi)(\mathbf{n} \times \mathbf{n}_d^{t^n}) \quad (3.8a)$$

$$\Delta\phi = \sqrt{(\Delta\beta_x)^2 + (\Delta\beta_y)^2 + (\Delta\beta_z)^2} \quad (3.8b)$$

$$\mathbf{n} = (-\Delta\beta_y\mathbf{i} + \Delta\beta_x\mathbf{j} + \Delta\beta_z\mathbf{k}) \quad (3.8c)$$

where $\Delta\phi$ is the magnitude of the rotation, \mathbf{n} is the normalized rotation vector, and $\mathbf{n}_d^{t^n}$ and $\mathbf{n}_d^{t^{n+1}}$ are the deformed unit vectors at times t^n and t^{n+1} expressed in the global coordinate system. The local rotational deformations can be calculated from the local deformed unit

vector $(\mathbf{n}_d^{tn})^L$ as shown in Equations 3.9a and 3.9b.

$$\beta_{x'} = (\mathbf{n}_d^{tn})_x^L \frac{\cos^{-1} \left((\mathbf{n}_d^{tn})_z^L \right)}{\sqrt{\left((\mathbf{n}_d^{tn})_x^L \right)^2 + \left((\mathbf{n}_d^{tn})_y^L \right)^2}} \quad (3.9a)$$

$$\beta_{y'} = (\mathbf{n}_d^{tn})_y^L \frac{\cos^{-1} \left((\mathbf{n}_d^{tn})_z^L \right)}{\sqrt{\left((\mathbf{n}_d^{tn})_x^L \right)^2 + \left((\mathbf{n}_d^{tn})_y^L \right)^2}} \quad (3.9b)$$

3.4.2 In-Plane: Constant Strain Triangle

The Constant Strain Triangle is designed to capture motion that occurs inside the plane of the structural elements. As shown in Figure 3.6, this would include both displacements and rotation (drilling) in the local x-y plane, however, inclusion of the drilling degrees of freedom usually leads to numerical instabilities. For this reason, drilling is ignored in this formulation.

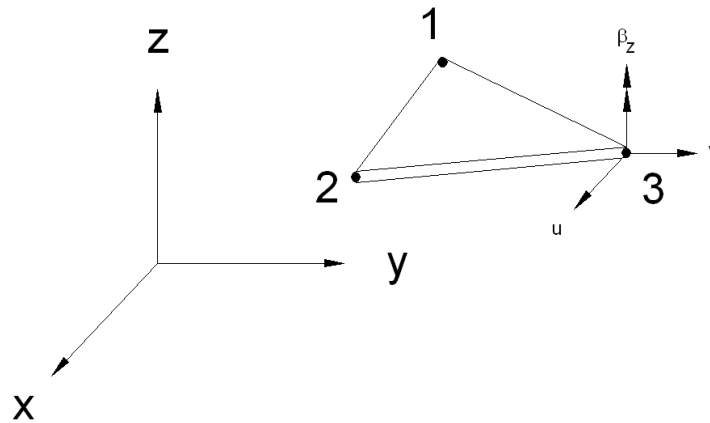


Figure 3.6: Nodal degrees of freedom for the CST.

The CST element contributes only six degrees of freedom to the typical structural element

after drilling is ignored.

$$\mathbf{q}'_w{}^T = \{ u'_1 \quad v'_1 \quad u'_2 \quad v'_2 \quad u'_3 \quad v'_3 \} \quad (3.10)$$

When expressed in the local Lagrangian coordinate, the local degrees of freedom are reduced even further.

$$\mathbf{q}'_w{}^T = \{ 0 \quad 0 \quad u'_2 \quad 0 \quad u'_3 \quad v'_3 \} \quad (3.11)$$

This is due to the special selection of the orientation of the local coordinates, as demonstrated in Figure 3.7.

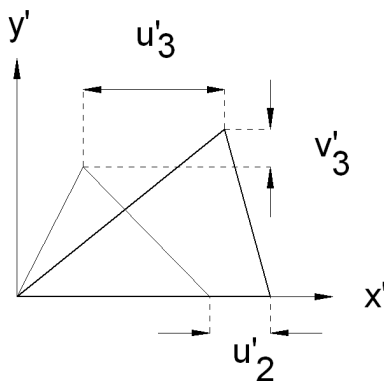


Figure 3.7: *In-plane deformation in Lagrangian coordinates.*

3.4.3 In-Plane and Out-of-Plane Coupling

The nonlinear structural model is based on the Von Karman plate theory with Green-Lagrange strains to provide nonlinear in-plane and out-of-plane coupling. Higher order terms in Green-Lagrange strains are dropped under the assumption that in-plane strains are small relative to out-of-plane strains. In the case of large deformations, the kinematic assumptions used to derive the governing equations are no longer valid and the Von Karman

formulation must be replaced with the Direct Eulerian-Lagrangian formulation. This allows the retention of kinematic assumptions guaranteed by the Von Karman plate theory so long as the wing behaves elastically.

3.4.4 Structural Element Equations

Each element component discussed in the previous section contributes to the overall formulation of the structural kinematics. The total strain energy for a structural element (U_{total}^e) is the combination of strain energies from membrane stretching of the CST (U_m), out-of-plane bending (U_b) and shear (U_s) from the DST, nonlinear coupling of in-plane and out-of-plane motion (U_{ncm}), and the nonlinear coupling effect of slope due to large deformations (U_{ncs}).

$$U_{total}^e = U_m + U_b + U_s + U_{ncm} + U_{ncs} \quad (3.12)$$

The equations for each contribution to the strain energy are given by

$$U_m = \frac{1}{2}h \int_A \{\epsilon_a\}^T [C_n] \{\epsilon_a\} dA \quad (3.13a)$$

$$U_b = \frac{h^3}{24} \int_A \{\kappa\}^T [C_n] \{\kappa\} dA \quad (3.13b)$$

$$U_{ncm} = h \int_A \{\epsilon_a\}^T [C_n] \{\epsilon_n\} dA \quad (3.13c)$$

$$U_{ncs} = \frac{1}{2}h \int_A \{\epsilon_n\}^T [C_n] \{\epsilon_a\} dA \quad (3.13d)$$

$$U_s = \frac{1}{2}h \int_A \{\gamma\}^T [C_s] \{\gamma\} dA \quad (3.13e)$$

Where U_m , U_b , and U_s are quadratic-order, U_{ncm} is cubic-order, and U_{ncs} is quartic-order.

The constitutive matrices $[C_n]$ and $[C_s]$ are given in Equation Group 3.14. Here, k is the shear correction factor, which is $\frac{5}{6}$ for rectangular cross sections, and G is the shear modulus.

$$[C_n] = \frac{E}{1 - \nu^2} \begin{bmatrix} 1 & \nu & 0 \\ \nu & 1 & 0 \\ 0 & 0 & \frac{1-\nu}{2} \end{bmatrix} \quad (3.14a)$$

$$[C_s] = kG \begin{bmatrix} 1 & 0 \\ 0 & 1 \end{bmatrix} \quad (3.14b)$$

The strain components are given by

$$\{\epsilon_a\} = \left\{ \begin{array}{c} \frac{\partial u'}{\partial x'} \\ \frac{\partial v'}{\partial y'} \\ \frac{\partial v'}{\partial x'} + \frac{\partial u'}{\partial y'} \end{array} \right\} \quad (3.15a)$$

$$\{\epsilon_n\} = \left\{ \begin{array}{c} \frac{1}{2}\beta_{x'}^2 \\ \frac{1}{2}\beta_{y'}^2 \\ \beta_{x'}\beta_{y'} \end{array} \right\} \quad (3.15b)$$

$$\{\gamma\} = \left\{ \begin{array}{c} \frac{\partial w'}{\partial x'} + \beta_{x'} \\ \frac{\partial w'}{\partial y'} + \beta_{y'} \end{array} \right\} \quad (3.15c)$$

$$\{\kappa\} = \left\{ \begin{array}{c} \frac{\partial \beta_{x'}}{\partial x'} \\ \frac{\partial \beta_{y'}}{\partial y'} \\ \frac{\partial \beta_{x'}}{\partial y'} + \frac{\partial \beta_{y'}}{\partial x'} \end{array} \right\} \quad (3.15d)$$

The principle of stationary potential energy is used with the total strain energy calculated in Equation 3.12 to form the element stiffness matrices. There are two stiffness matrices associated with each finite element, the tangent stiffness matrix $[K_t]$ and the secant stiffness matrix $[K_s]$. The typical partition of an element tangent or secant stiffness matrix is down in Figure 3.8.

$$\begin{bmatrix} \mathbf{K}_e \\ 15 \times 15 \end{bmatrix} = \begin{bmatrix} \begin{bmatrix} \text{out-of-plane} \\ \text{partition} \\ \text{(DST)} \\ 9 \times 9 \end{bmatrix} & \begin{bmatrix} \text{coupling} \\ \text{partition} \\ \text{(nonlinear)} \\ 9 \times 6 \end{bmatrix} \\ \begin{bmatrix} \text{coupling} \\ \text{partition} \\ \text{(nonlinear)} \\ 6 \times 9 \end{bmatrix} & \begin{bmatrix} \text{in-plane} \\ \text{partition} \\ \text{(CST)} \\ 6 \times 6 \end{bmatrix} \end{bmatrix}$$

Figure 3.8: *Typical partition of an element tangent or secant stiffness matrix.*

The tangent stiffness matrices are used in the calculation of the incremental deformations of the global system. The secant stiffness matrices are used to form the element elastic forces in local coordinates, which are then transformed to global coordinates to form the global elastic force vector. For details of the derivation of these matrices, see Seber [13] and Rajasekaran and Murray [51].

Chapter 4

Fluid-Structure Coupling

4.1 Introduction

As mentioned previously, an inner layer of the fluid mesh functions as the airfoil surface for aerodynamic calculations and is attached rigidly to the structural mesh. These surface-aero nodes move directly with the structural mesh using the local Lagrangian coordinate system as if they were part of the structure itself. The locations of these nodes relative to structure are known in advance and never change, meaning that their Eulerian coordinates can be found via pre-constructed transformations without any additional computation. The benefit of this method is that the code does not have to search for the locations of the fluid surface nodes relative to the structure prior to calculations.

4.2 Fluid-Structure Boundary Model

During mesh initialization, the fluid mesh nodes that form the wing surface are given a z-axis offset based on the wing thickness and airfoil shape. The initial positions of these surface nodes in the x-y plane are calculated and saved in area coordinates for the structural element they belong to. As an element deforms, points inside that element deform in the same fashion, however, the area coordinates of those points remain constant. This means that area coordinates for wing surface nodes only need to be calculated once. Figure 4.1 shows a spatial representation of the relationship between a structural element and an aerodynamic fluid node.

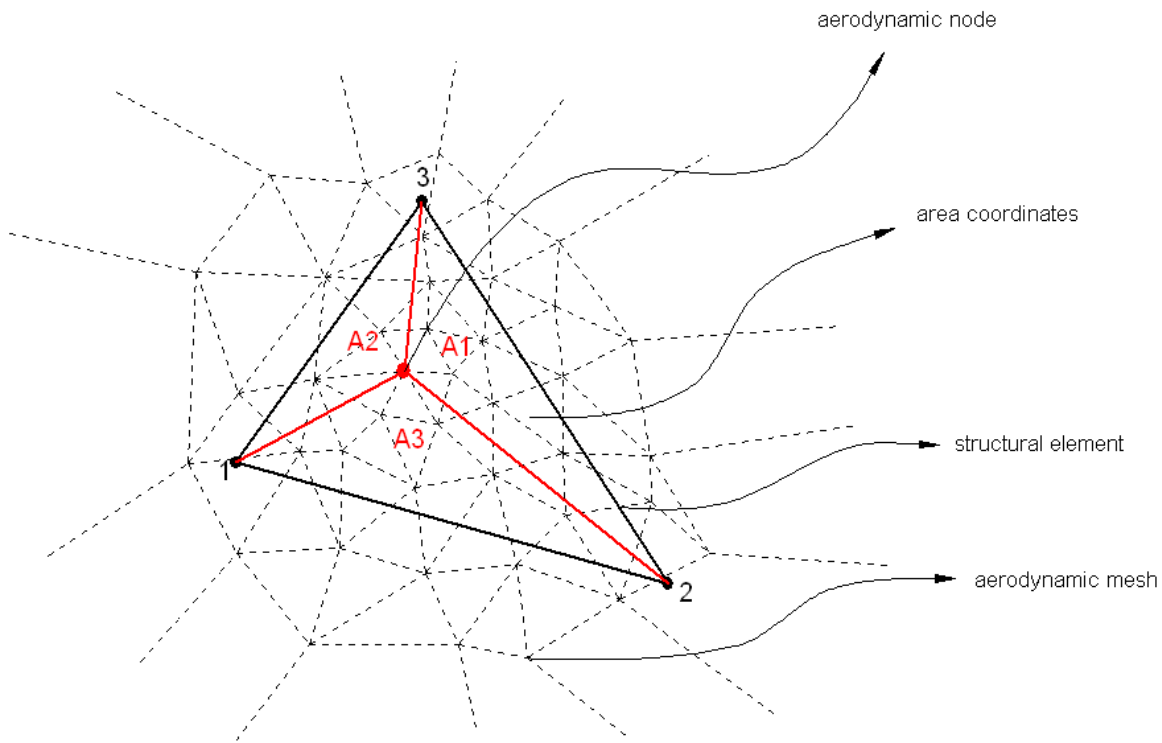


Figure 4.1: *An aerodynamic fluid node attached to a structural element using area coordinates.*

In addition to the wing surface nodes, each structural element has thirteen Gaussian quadrature points used to solve the aerodynamic forces acting on that element. The locations of these quadrature points on the element surface are saved in area coordinates, which do not change. To solve the new aerodynamic load at the next time step, all that is needed is the updated pressure values at each quadrature point. Updated data values must be obtained through the flow conditions at the fluid nodes that comprise the wing surface. These nodes form their own shell of triangular elements offset from the structural mesh. When viewed from 'above' each Gaussian quadrature point in a structural triangle also belongs to a fluid triangle above it. Since the fluid is attached to the structure in the

same manner as the Gaussian quadrature points, each point always belongs to the same fluid triangle and structural triangle even after deformation. Moreover, the location of each Gaussian quadrature point inside its fluid triangle can be found in yet another set of area coordinates (shown in Figure 4.2), which never changes. For the purpose of calculating aerodynamic forces, the pressure field inside the fluid triangle is assumed to be linear, and the data value at any Gaussian quadrature points contained therein can be solved through interpolation. Figure 4.3 shows the surface pressure as a follower force being projected onto a structural element.

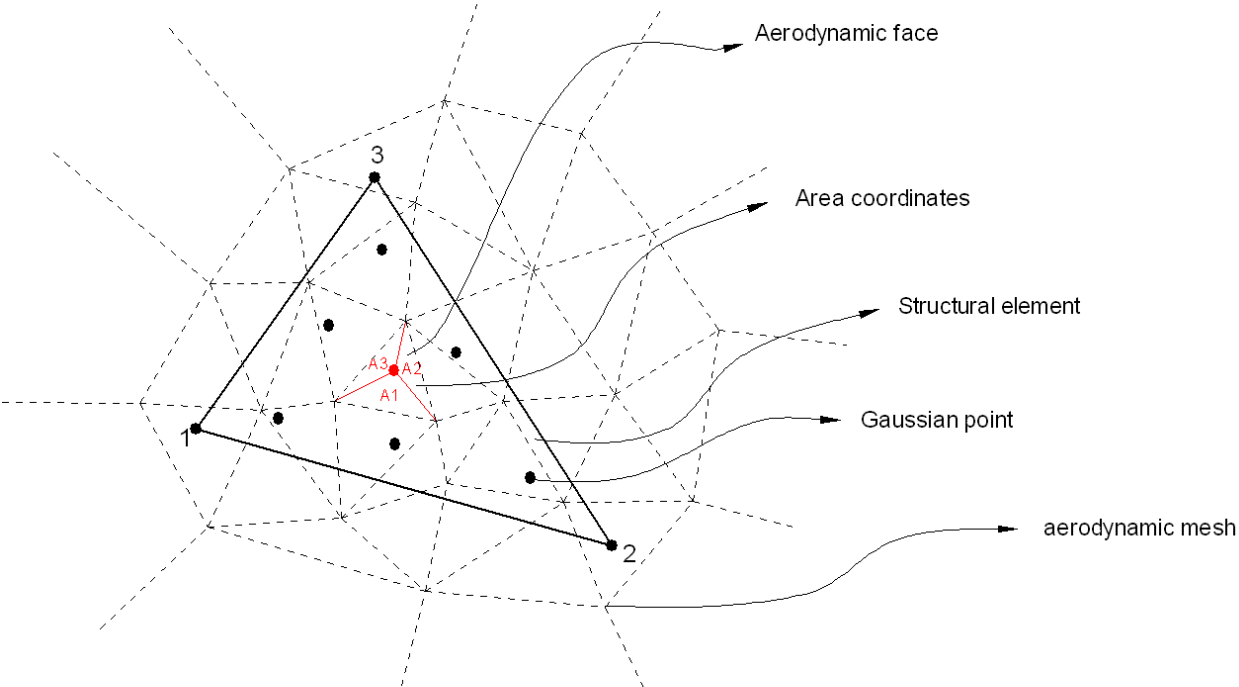


Figure 4.2: A Gaussian quadrature point attached to an aerodynamic fluid element using area coordinates.

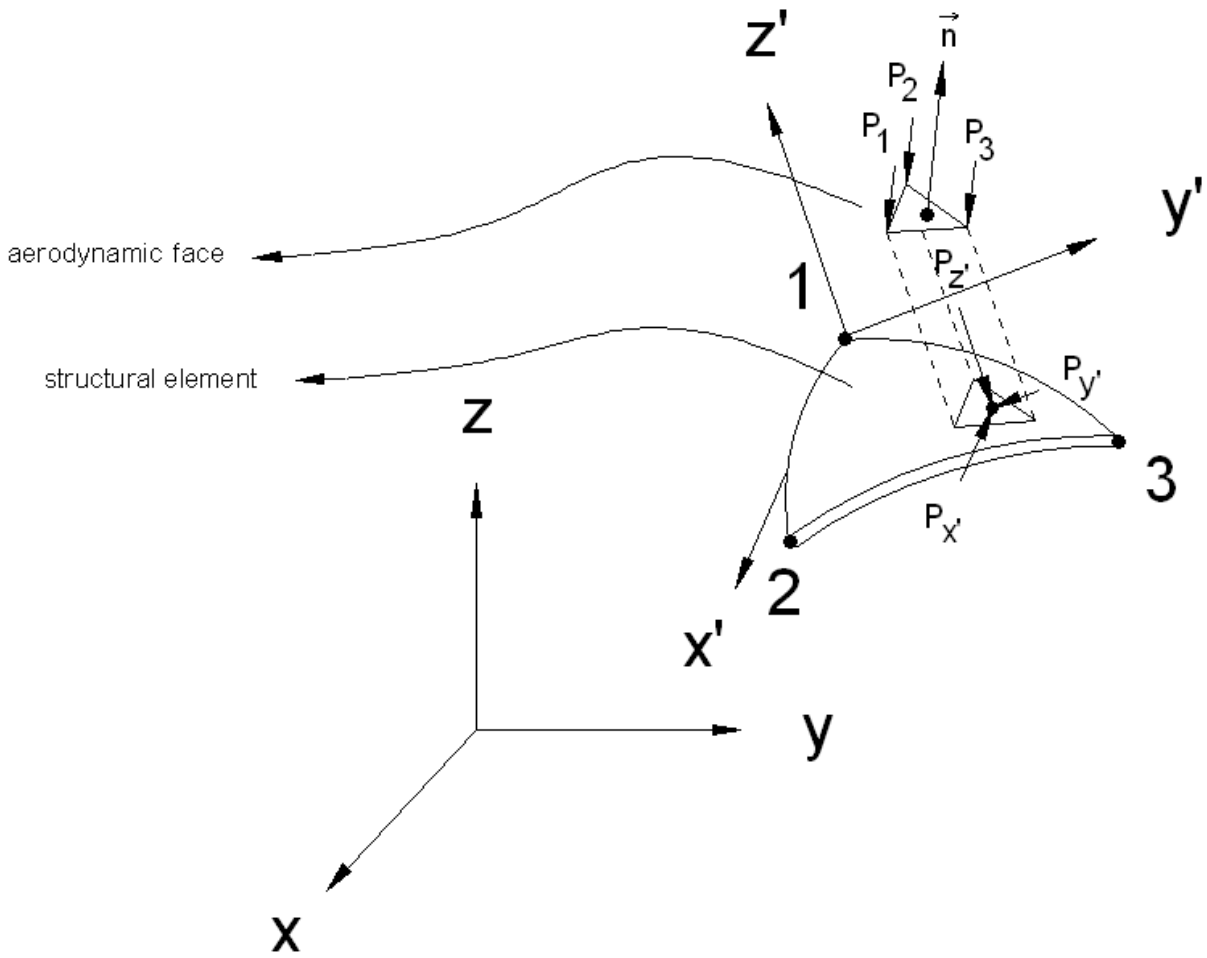


Figure 4.3: *Surface pressure being interpolated at a Gaussian quadrature point from the nodes of an aerodynamic fluid element.*

4.3 Dynamic Aeroelastic Solution Procedure

A five-stage explicit Runge-Kutta scheme is used to solve the differential equation,

$$[M] \{\ddot{q}_t\} + [K] \{q_t\} = \{F\} \quad (4.1)$$

Here, $[M]$ and $[K]$ are the structural system global mass and stiffness matrices, $\{q_t\}$ is the

global displacement vector, $\{F\}$ is the global external force vector, and overdots represent derivatives with respect to time. All terms vary with time except for the mass matrix $[M]$, which only needs to be calculated once at the beginning of the simulation. The external forces are limited to aerodynamic forces only.

The second term in Equation 4.1 represents the global elastic force vector, $\{F_{elastic}\}$. Moving this term to the right hand side yields the equation

$$[M] \{\ddot{q}_t\} = \{F\} - \{F_{elastic}\} \quad (4.2)$$

The solution procedure for Equation 4.2 is given by the following steps (as outlined by Seber [13]):

1. Invert the global mass matrix.
2. Calculate the time step.
3. Update the structural conditions (or set them from an initial condition).
4. Calculate the right hand side using the global aerodynamic load vector and global element elastic force vectors.
5. Solve Equation 4.2 for the accelerations.
6. Integrate the accelerations to calculate the new velocities and displacements.
7. Update the deformed nodal vectors.
8. Calculate the new wing surface fluid node locations.
9. Calculate the new interior fluid node locations.

10. For stage one or stage two of the Runge-Kutta scheme, calculate the adaptive dissipation vector for the fluid.
11. Solve the current stage of the Runge-Kutta equation.
12. Update the vector of conserved flow quantities.

Each Runge-Kutta stage repeats this procedure starting with updating the structural variables. Each new time step repeats the procedure from calculating the new time step.

Chapter 5

Changes to the Aeroelastic Code

5.1 Introduction

The code development goal for this project was to take the functioning serial nonlinear flutter solver developed by Seber [13] and time-optimize how it can be used to compute a large volume of results. Importantly, this was to be accomplished without altering the algorithm and while maintaining, as close as possible, the exact same solution. There are two main issues with the original program that make it difficult to implement on a large scale. First, the amount of data we intend to collect requires the use of UCLA's Hoffman2 computing cluster. However, the code requires linking to commercially licensed libraries that are not available on Hoffman2. Second, results for most test conditions can be obtained in a matter of days or weeks, but no quantity of processors can speed up the months of continuous computation it can take to converge to the steady state solution at some key data points.

The first issue has been resolved by converting to open-source libraries for any external subroutine calls. It is a relatively simple change, but necessary to make it possible to

execute the aeroelastic code of the Hoffman2 cluster, allowing dozens of programs to operate simultaneously and removing the need to skip data points in the test-matrix in the interest of time. The second issue has been tackled by creating a parallel version of the source code that can reduce the wall-clock time required to converge to a steady state solution.

5.2 Changes for use on the Hofmman2 Cluster

The Hofmman2 cluster is UCLA's remote-access network of computing nodes that are made available for academic research purposes. There are over 1200 nodes and 13,000 cores, making it an invaluable resource for a project like this one. For Fortran 77 specifically, the cluster uses an Intel compiler and maintains a library of commercially licensed and open source subroutines.

The only substantive change necessary to make the source code compatible with the Hoffman2 cluster was to swap out the set of subroutines used for solving and manipulating linear systems of equations. The original program uses IMSL libraries, which the cluster does not have a license for. They were replaced by BLAS and LAPACK libraries, which are open source. The subroutines from these libraries are used to solve the linear system of equations created from the global mass and stiffness matrices and the global force vector. Additionally, they are used to find natural modes and frequencies from the free vibration eigensolution of those matrices.

The remaining alterations to the source code are line-by-line bug fixes, often resulting from the compiler-specific handling of ambiguities and syntax errors created by the programmer. Uninitialized variables, mismatched data types, wrong intrinsic function calls, and the

ordering of statements in a subroutine header are a few examples what are technically errors under the rules of Fortran 77, but may not be returned as errors by the compiler. It is possible to select specific compiling options that are less strict about the programmer following the rules, in which case the compiler will attempt to fix those mistakes based on the context. It was deemed better to have these errors returned at compile-time; taking the opportunity to clean up the syntax and ensure the executable code performs as intended.

5.3 Parallelization

The parallelization of this program uses Message Passing Interface (MPI) for Fortran 77 and is based on the work done by Guang-Yaw Hwang [12]. He created the original serial linear flutter solver as well as a stand-alone parallel version nearly twenty years ago. However, complications with the hardware utilized for parallel computation led to the decision to abandon further development of parallelized code. There have been twenty years of changes made to the serial program that prevent a simple copy/paste of the parallel subroutines. However, the program is modular in nature, meaning the majority of changes have not impacted the order of operations when the code is executed. This means the algorithm of the original parallel implementation is still valid, but is basically non-functioning on the line-by-line level when directly transplanted. The following subsections provide conceptual details about how the parallel algorithm functions, as well as how the serial code has to be changed to accommodate the parallel structure.

5.3.1 Division of Work

A relatively simple approach is taken in dividing the workspace between processors. The computational domain is made up of roughly 62,000 nodes, which need to be split up into as many sub-domains as there are processors. The global domain is divided by taking vertical slices perpendicular to the plane of the wing, and assigning the resulting sub-domains to the individual processors. Since the concentration of fluid nodes is nearly constant in the span-wise direction, the distribution of nodes ends up relatively even in each sub-domain. Additionally, since the computational sub-domains share at most two interfaces (on either side of the vertical slice), the potential number of ghost nodes (placeholder values needed for calculations where node connections have been broken) remains reasonably low. The goal in this regard is to minimize the number of nodes exposed on the surface of the slices. Since the majority of fluid nodes are located in a tightly packed three-dimensional sheath around the wing surface, acceptably few nodes are revealed when using a transverse slice.

5.3.2 Sub-Domain Algorithm

The functional implementation of this division requires some method of redefining the global array of nodes as unique local arrays for each processor. Most calculations in the code are performed by looping over all the nodes in the domain, and ideally, replacing one configuration of nodes with another doesn't cause any problems. Fortunately, the solution algorithm is designed to work for various wing shapes and size, its function does not have a strict dependence on the total number or configuration of nodes and boundary nodes. It only needs to know how nodes are labeled in order to correctly incorporate them into the appropriate

calculations. Because of this, it is possible on each processor to swap the node array from the global spatial domain to the local spatial domain just by re-enumerating the correct subset of nodes. It makes no difference whether the problem being solved is a full wing in a box or a just a slice of that wing, so long as the spatial domain is rebuilt correctly in the appropriate arrays.

The only problem created by slicing up the domain is that a new type of boundary is created wherever node connections have been severed. Any calculations which require data from adjacent nodes cannot be performed at these boundaries, because the adjacent nodes no longer exist. To solve this problem, each processor must reconstitute these missing connections in the form of ghost nodes, a single layer of fake data points which store necessary data values from the real data points in neighboring processor sub-domains. Once the data from a ghost node has been used for inter-node calculations, it is considered spent and must be updated before it can be used again. Usually this is done via message passing, retrieving the new data value from the corresponding real node in the neighboring processor's sub-domain. Alternatively, additional ghost node layers can be added to delay the need for interprocessor communication. Each extra layer means that one additional calculation can be performed without altering the solution of the program in that sub-domain. Basically, this method is just ghost nodes for the ghost nodes, which can be counterproductive to the original purpose of dividing the domain to reduce its size. Whether to use additional ghost nodes or additional message passing is usually determined by what provides the best performance. The "right" answer is dependent on a number of factors, including the program algorithm and the physical hardware configuration.

The only other consideration would be the execution of order-dependent algorithms,

where a different enumeration of the same domain yields a new result. In this case, parallelization necessarily changes the exact solution, and the only workaround is to temporarily return to the original global scheme to perform the order-dependent calculation. The next best thing in this situation is to validate that the convergence of the big picture solution is not affected by the discrepancy created in that moment.

5.3.3 Sub-domain Implementation

As part of the program initialization, each processor performs a block of subroutines that separate the program into two distinct parts: global (pre-parallel) and local (post-parallel). Before this block is executed, all processors initialize the global arrays necessary for the full problem solution, including all nodes, lines, faces, cells, and boundaries. Then, in the parallel subroutine block, the full domain is replaced with the sub-domain belonging to the executing processor. Data points outside the local domain are stripped from the nodal array. Array indices for the remaining nodes are then renumbered within their processor, and a mapping between the local and global domains is preserved. This is the point at which each processor seeks out its respective ghost nodes. These nodes are appended to the sub-domain node arrays, but are given a special boundary identifier that excludes them from certain calculations (namely anything that would attempt to search for a further layer of ghost nodes that does not exist). The lines, faces, cells, and boundaries are also re-evaluated within the local scheme. When each processor dumps back into the main algorithm, it is now applying the same solution process to a differently shaped domain. The only thing left to account for is to find every inter-node calculation in the program, and ensure that ghost

node data values are up-to-date as needed.

5.3.4 Optimization

There are two factors which affect efficiency in parallel computation: duplication of calculations and interprocessor communication. Any nontrivial parallelization requires the use of ghost nodes and message passing. Each time a ghost node is used in a calculation the inter-node computation is mirrored in the neighboring processor, meaning some time is being wasted on repeated work. Also, each time a ghost node has to be updated through message passing, the involved processors may have to wait to continue calculations. This particular program uses a five-stage Runge-Kutta algorithm with multiple instances of inter-node calculation inside each stage. That means, at the bare minimum, ghost nodes have to be updated once for each stage and possibly multiple additional times within a given stage depending on the configuration. The result is that this program has substantial parallel overhead for each time step, and there will be a noticeable loss of efficiency so long as the integrity of the serial algorithm is maintained. The goal of optimizing this process is to find the combination of ghost nodes and interprocessor communication that yields the best results for the hardware being used.

The parallel implementation that was used as the framework for this program was designed to minimize interprocessor communication. It was determined that four layers of ghost nodes were needed to meet that criteria. Ghost nodes increase sub-domain node counts by approximately 2000 nodes per layer per exposed boundary (2000 for the first and last processor, and 4000 for anything in between). In the case of four processors and 62455 nodes,

the largest sub-domain will contain approximately 30,000 nodes. Already, parallel execution in this configuration is expected to suffer a fifty percent loss of efficiency. The alternative, reducing ghost nodes and increasing message passing, would seem like it must necessarily provide a more efficient solution. However, this may not be the case depending on the communication medium. Some parallel hardware configurations are physically separated and rely on network or high-speed cable connections to exchange information between processors. These setups necessarily introduce additional delays and wait times that do not bode well for complicated algorithms. Increasing the number of instances of message passing is only an effective solution for shared-memory nodes where a single multi-core processor handles the entire parallel program and all cores are able to access the same memory modules directly.

Today's hardware configurations are often two-, four-, six-, or even eight-core processors that fit the shared-memory format described above. For this reason, optimization of the parallel algorithm has been done with shared-memory as the assumed hardware configuration.

The new parallel implementation uses a single layer of ghost nodes along with considerably more instances of message passing. Reducing the number of layers of ghost nodes is very nearly trivial, with the primary requirements being commenting out a large block of code and changing the appropriate variable to tag the first ghost node layer as the outermost. However, one layer is particularly difficult to debug, because it requires finding every instance of inter-node computation and following the result line-by-line to determine if and when it needs to be updated. Every instance of unnecessary message passing means a loss in efficiency.

5.4 Verification of Parallel Computational Accuracy

This program uses the Fortran 77 standard with Message Passing Interface (MPI) for parallel computation. MPI allows processors to communicate data values stored in memory without loss of precision. This leads to identical execution when compared to a serial implementation, except in cases where the order of execution affects the solution. In this program, one such order-dependent algorithm exists in the interior fluid-mesh node-movement subroutine.

The spring-equilibrium analogy used to update the locations of fluid mesh nodes progresses very slowly when done through simple iteration. Since the impetus for all fluid mesh motion is the fluid-structure boundary, only the first layer of adjacent nodes can "feel" this motion after one iteration. This assumes that new node positions are solved from adjacent node data only, and that they are stored in a temporary array until all indices have been calculated for the current loop. To speed up the flow of information into the mesh, this program uses a forward-substitution method in which new node location data overwrites old array values immediately. This means it is possible for the mesh boundary movement to propagate through the entire fluid mesh in a single loop of the equilibrium algorithm. Unfortunately, the exact solution from this method depends on the order of calculation, and dividing the domain for parallel processing guarantees that the exact solution will be different. However, if this difference does not affect the convergence of the overall program solution, then it can be neglected.

Three configurations of parallelization were tested against the original serial solution to find the best combination of speed and accuracy. The first uses four layers of ghost nodes that

only needs to be updated once at the end of each Runge-Kutta stage. This is the updated parallel structure that Hwang developed [12] and has the drawback of creating a rather large computational domain. The second configuration contains a single layer of ghost nodes that has to be updated between any two uses of adjacent node data. This method results in a smaller domain per processor, but requires significantly more message passing compared to the four-layer version. The third configuration is identical to the second, except that it returns each processor to the global domain when solving the interior fluid mesh motion. This last method is expected to inhibit performance, and is primarily a comparison tool to determine if parallelizing the order-dependent fluid mesh movement algorithm is adversely affecting the accuracy of the solution.

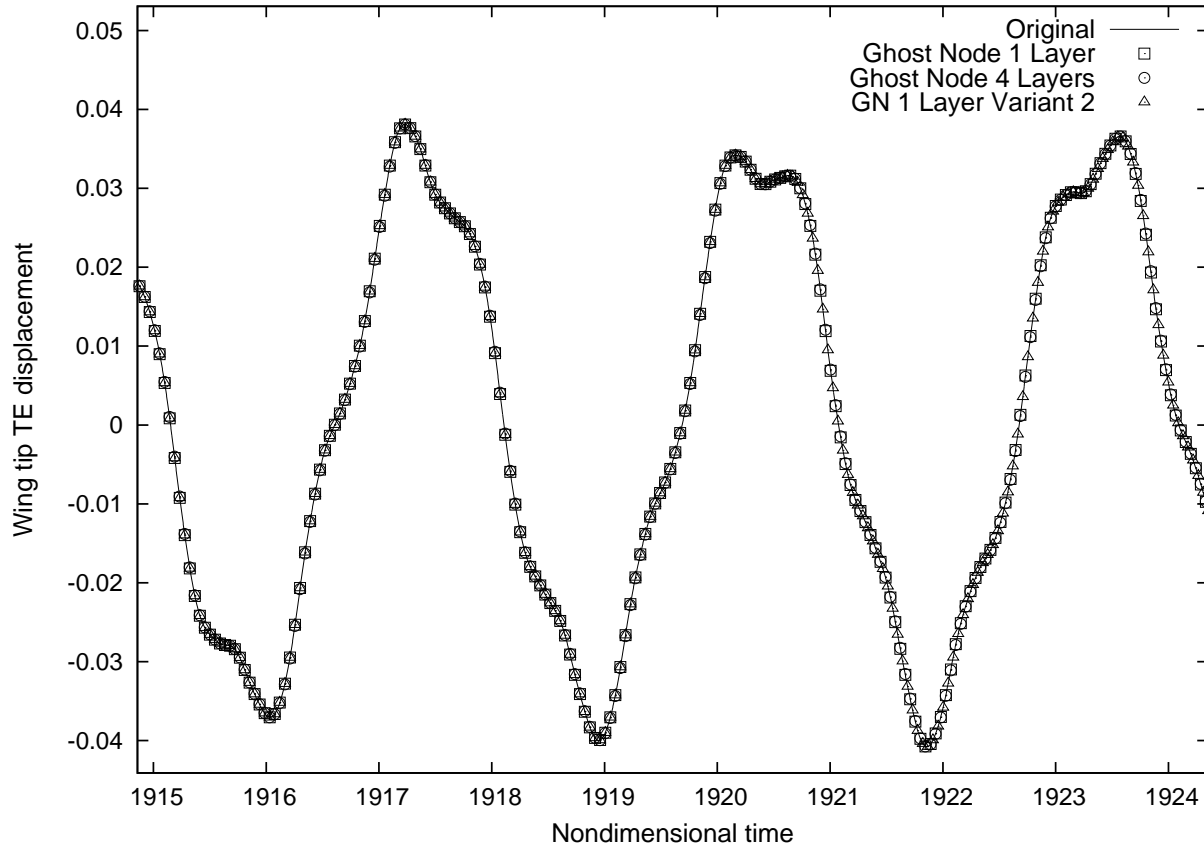


Figure 5.1: Verification of parallel computational results versus original serial output.

Figure 5.1 shows the wing tip trailing-edge displacement solution for the FX-35 wing at Mach 0.98, 0.007 plate thickness, zero angle of attack, and 0.499 kg/m^3 density using the serial method and all three parallel configurations. This particular example was chosen because of the complicated modal participation apparent in the solution, which all three programs capture extremely well. Since there is no discernible difference in accuracy between parallel configurations, the fastest one was chosen for production.

5.5 Benchmarking and Parallel Configuration Selection

Creating a reliable benchmark for any program can be tricky, since the performance of an executable changes with different hardware setups and can also vary between runs on the same hardware. With that in mind, benchmarking was done in as close to a controlled environment as possible, and using the hardware on the Hoffman2 cluster, since that is where all production runs are executed.

The Hoffman2 cluster allows users to request interactive control of a computational node for a limited period of time. During that time, that node may be used to compile and execute any programs stored on the remote servers in real-time. Users can make specific requests for the amount of memory, number of cores, and duration of access to the node. Additionally, the request can be limited to a shared-memory node, which restricts the session to a single multi-core processor that also meets the aforementioned criteria. If there are no matching nodes available, then the user is simply given an error message. When access is granted to a node, there is no guarantee that it is the same hardware accessed in a previous session.

With this in mind, multiple benchmarking sessions were executed on shared-memory multi-core processors (between six and eight cores depending on availability); averaging the results from three to five identical runs for each program configuration using one through eight cores. Results varied between runs and between hardware configurations, but the overall pattern of performance across cases was consistent.

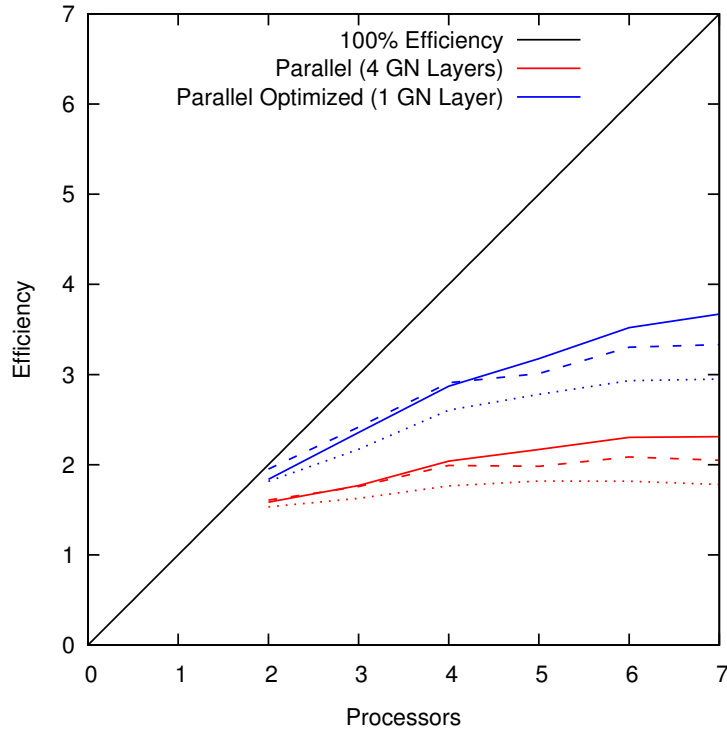


Figure 5.2: Benchmarking results for the original and optimized parallel configurations. A range of results from three separate hardware tests are shown, demonstrating the varying performance of both hardware and software.

Figure 5.2 shows the benchmarking results for the two major parallel configuration milestones created through this research. Each line represents the averaged results from one hardware setup, with three setups presented in the figure. The results vary noticeably for both parallel configuration. However, the difference in performance between the programs is consistently in the favor of the hardware-optimized version, which is not unexpected. The original four-ghost-node-layer program performed adequately, with roughly 50% efficiency when using four cores. The optimized single-ghost-node-layer version showed an appreciable increase in performance with around 70% efficiency for four cores. Both parallel implementa-

tions do rather poorly with anything more than four cores, due in part to the large overhead inherent in the algorithm. However, that is not to say that performance could not be further improved.

Chapter 6

Results: TDT Wing Models

6.1 Introduction

The computational results presented in this chapter are part of a preparatory process to select a wing model for wind tunnel testing. This project is part of the design process for that model, but does not include the production or testing of the model, which will take place at some point in the future. The wind tunnel, sometimes referenced here as the Transonic Dynamics Tunnel or TDT, and its operating parameters have already been determined in advance, along with the decision to select some variety of fighter wing. What remains is to choose the specific wing model and to show that it exhibits worthwhile flutter behaviors inside the operable range of the wind tunnel. This chapter presents two viable candidates for wind tunnel testing based on aeroelastic phenomena observed in the computed data.

6.2 Candidate Wings: FX-35 and the F-Wing

The two wing designs chosen for numerical computation are the FX-35 and the F-Wing shown in Figure 6.1. Detailed parameters for both wings are given in Table 6.1. The FX-35 is an approximation of the planform for the F-35A, the newest generation of military fighter, which is a trapezoidal wing with a moderately-swept leading edge and a slightly forward-swept trailing edge. The F-Wing is based on the F-16 style fighter aircraft, with a moderately-swept leading edge and trailing edge sweep.

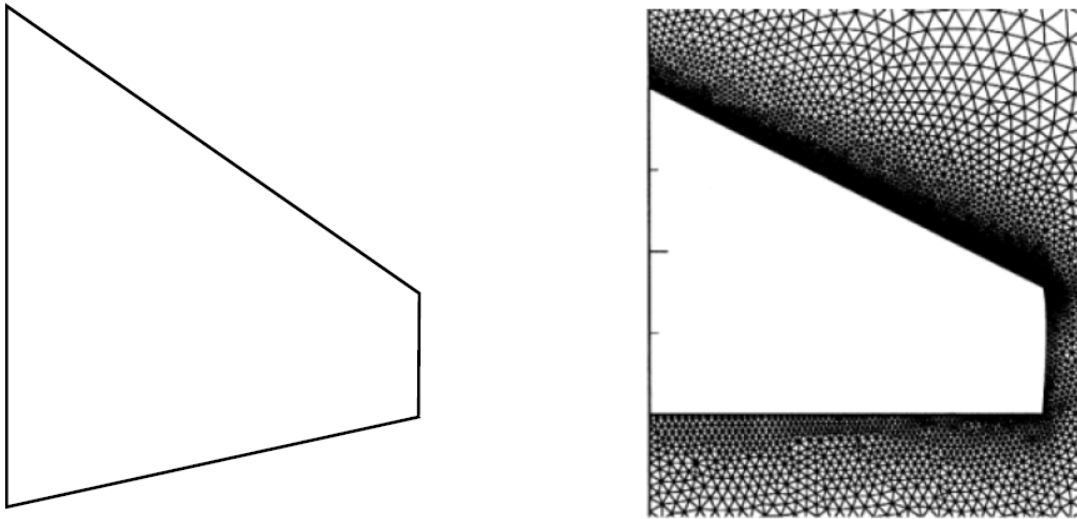


Figure 6.1: *The FX-35 (left) and F-Wing (right) planforms.*

Model	$b/2$	A	Λ_{LE}	Λ_{TE}	λ	Airfoil
FX-35	$0.832c_r$	2.67	35°	-11.7°	0.245	NACA 64A003
F-Wing	$1.2c_r$	3.457	27°	0°	0.3866	NACA 64A003

Table 6.1: *Wing planform parameters for the FX-35 and F-Wing.*

Normally, computational results for these two wings are done near atmospheric conditions. However, the TDT operational range is for considerably lower dynamic pressure. As a result, both wing models have been modified to have a reduced thickness, which should shift their flutter responses into the desired test scope. Comparisons of the natural frequencies between the atmospheric and TDT wing models are shown in Tables 6.2 and 6.3. Mode shape contour plots can be seen in Figures 6.2 and 6.3.

Model	t	1B	1T	2B	2T
FX-35 (atm)	0.007	12.068	44.071	59.864	112.439
FX-35 (TDT)	0.004	6.896	25.185	34.214	64.253

Table 6.2: The first four natural frequencies (Hz) of the FX-35 for the standard atmospheric and modified TDT models ($t = \text{plate thickness}$).

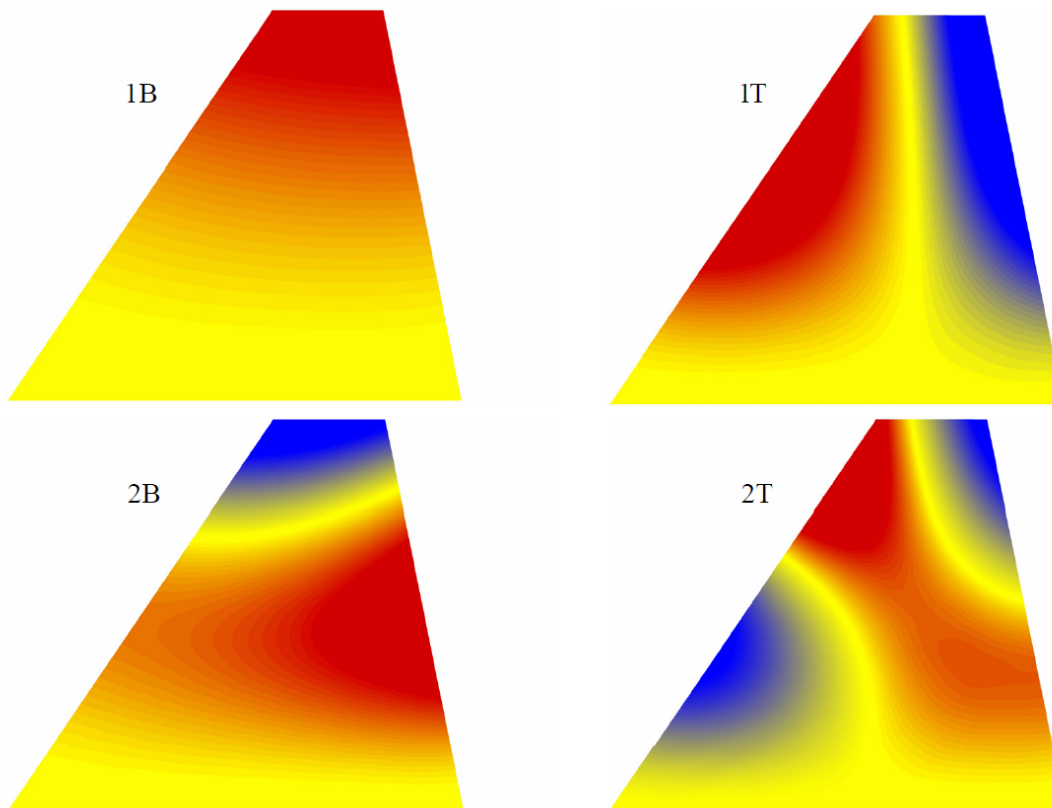


Figure 6.2: The first four natural modes of the FX-35 wing planform.

Model	t	1B	1T	2B	2T
F-Wing (atm)	0.012	8.939	38.361	48.264	100.657
F-Wing (TDT)	0.008	5.960	25.575	32.185	67.110

Table 6.3: The first four natural frequencies (Hz) of the F-Wing for the standard atmospheric and modified TDT models ($t = \text{plate thickness}$).

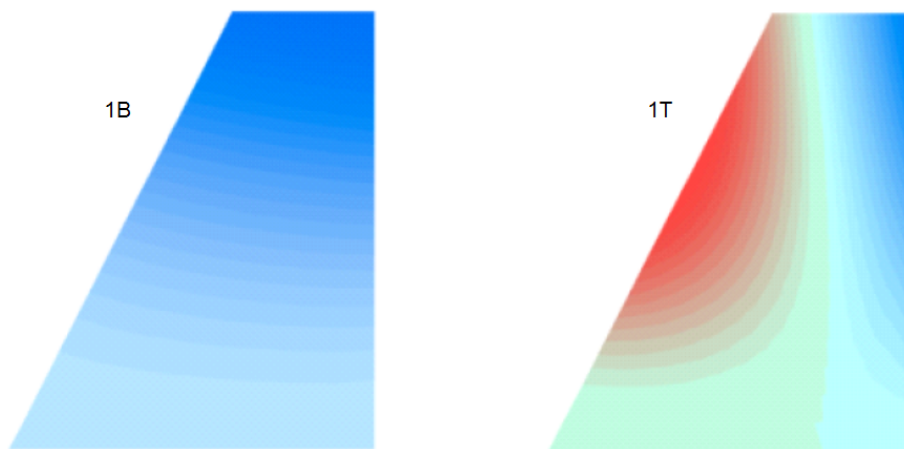


Figure 6.3: The first two natural modes of the F-Wing planform.

Figures 6.4 and 6.5 characterize the various stability responses of the FX-35 and the F-Wing under the TDT operating parameters. All calculations were performed at zero angle of attack and parameters represent free stream values. It is important to note that almost all responses contain transonic Mach distributions on the upper and lower wing surface that often terminate in a normal shock. The green and orange/red regions in these figures show the stability boundary for traditional flutter behavior, where the first bending mode is either decaying to a near zero amplitude or growing to the point of structural failure. Orange indicates the response is in transition from mostly first-bending to strong bending-torsion,

which are the red dots. Additional behaviors are explained below.

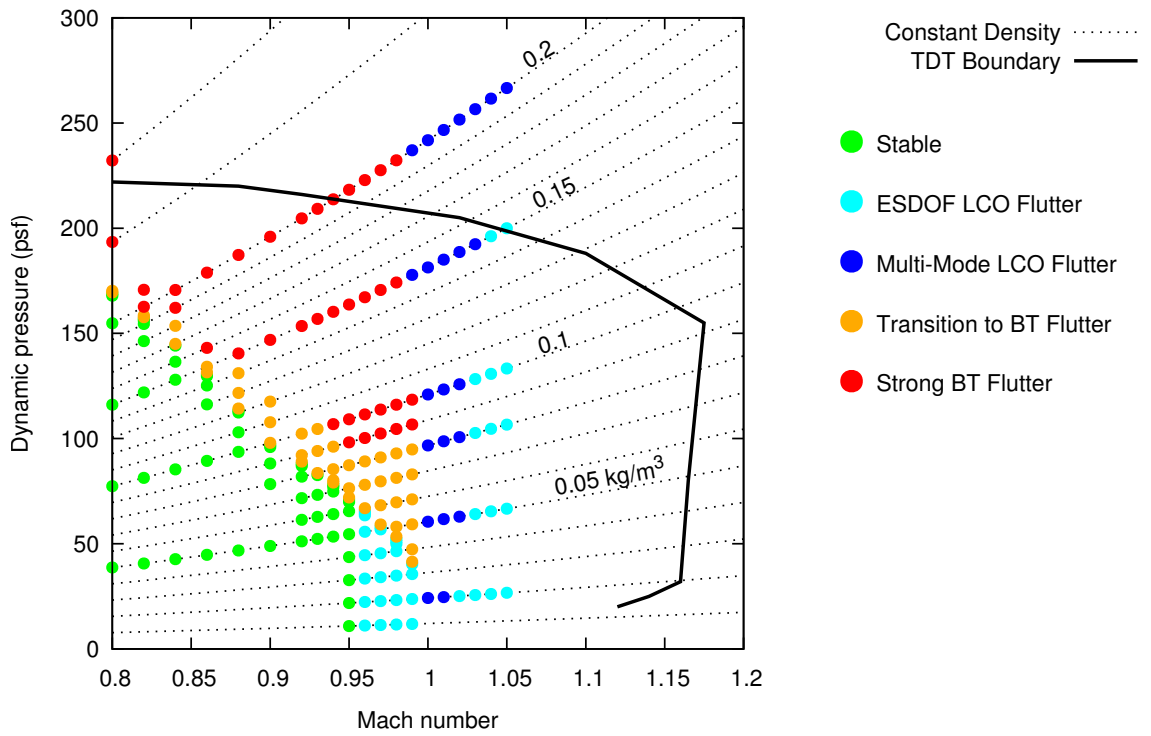


Figure 6.4: Stability responses for the FX-35 wing at TDT conditions with zero angle of attack and 0.004 plate thickness.

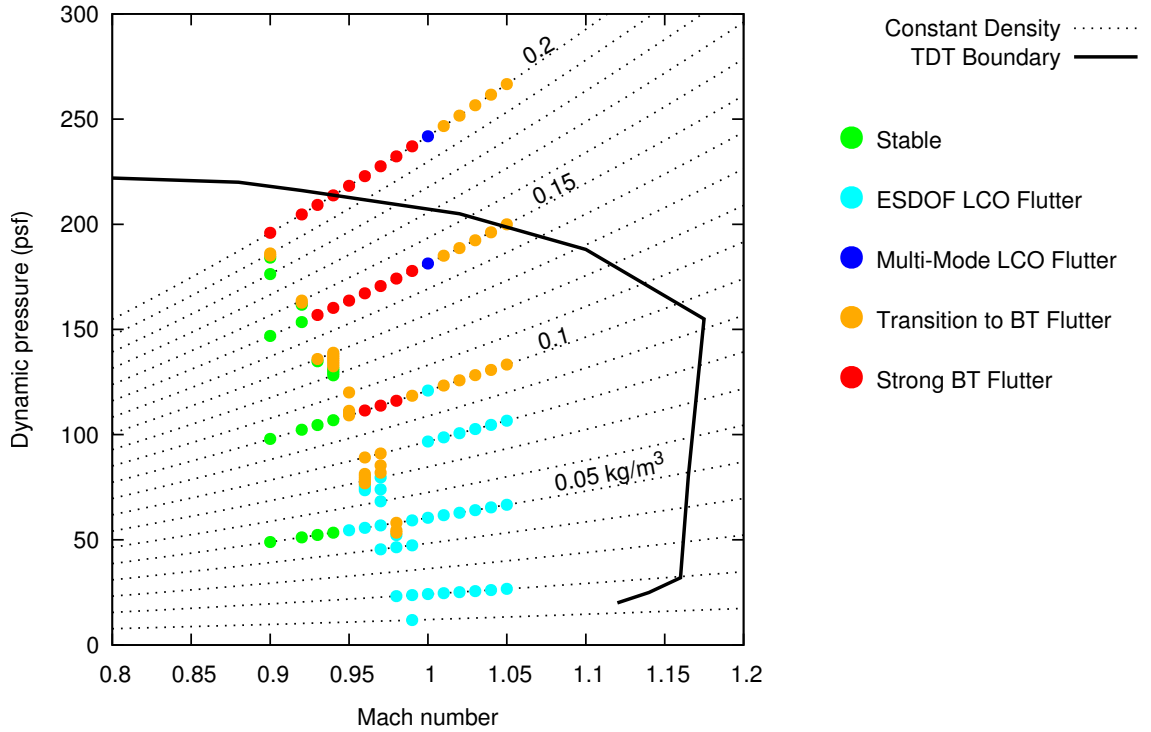


Figure 6.5: *Stability responses for the F-Wing at TDT conditions with zero angle of attack and 0.008 plate thickness.*

The cyan region indicates the transition to the chimney, a rather peculiar area wherein the second bending mode invariably remains neutrally stable even after all other modes have been completely damped out. This behavior begins very suddenly once a Mach number threshold has been crossed, and continues down to near-zero air density; creating a chimney-like shape in the corresponding figure. The amplitudes of wing tip pitch and plunge are nearly independent of changes to dynamic pressure, at least until the value is high enough for general flutter instabilities to re-emerge. This is also the first occurrence of true limit-cycle behavior, where various initial conditions converge to the same steady state amplitude.

The far right of the figure contains results for the transition into supersonic Mach num-

bers, which share characteristics of the chimney at low dynamic pressure and exhibit unstable flutter at high dynamic pressure. However, right at the beginning around Mach 1.00, the response is overall much more chaotic in nature, and often lacks the aesthetically pleasing qualities of subsonic data points. Seemingly random bursts in amplitude and mode participation make it difficult to make any specific correlations between it and the other regions. The FX-35 contains a large range of limit-cycle steady states with multi-mode responses between Mach 1.01 and Mach 1.05. The F-Wing, by contrast, starts from essentially single degree of freedom first-bending limit-cycles at low density, then transitions to bending-torsion flutter as density increases.

The figures show that both candidate wing models exhibit the desired range of aeroelastic responses within the parameters of the TDT tunnel. A great number of individual data points and thousands of extra hours of computation were used to depict with as much detail as possible exactly what the model predicts for the regions discussed above. However, that is not to say that even greater detail does not remain hidden beyond the reaches of what time allowed for. The following section takes a closer look at the results from individual test points representative of known types of flutter response. The focus remains on the demonstration that these behaviors exist within the model; attempts to explain the causes behind those behaviors are left to a minimum.

The entire test matrix can be divided into three distinct regions based on the changing characteristics of the response with respect to Mach number. First is the subsonic stability boundary, which is the dividing line for growth or decay of the initial response. This region contains very few neutrally stable responses and limited multi-mode influence. The second region is the chimney, which still exhibits stability boundary behavior with respect

to the initial condition, but introduces a steady state second-bending response present at all densities. However, the strength of this response is relatively low and is easily drowned out by first-bending at higher densities. The last region is the supersonic response after the Mach number freeze, a strong damping effect that occurs around Mach one. This region is characterized by neutrally stable or weakly unstable responses with possible multi-mode interaction.

6.3 Subsonic Stability Boundary

Each individual test point is a unique combination of Mach number and density, but they all begin with a similar initial condition, which is a small kick to the first bending mode. How this mode grows or decays is the first indication of the expected flutter response at that test point. Instability in the first bending mode almost always corresponds to strong flutter, while the stability of this mode generally indicates stable or neutrally stable behavior. With this in mind, the first bending mode can be used to narrow the pool of data points chosen for extended computation. Transient behavior in the wing response may look different depending on the initial condition, but for most test points the steady state solution is unaffected. The initial condition used here is intended to identify the strong flutter boundary first, and steady state solutions second.

For each Mach number in the range indicated in Figure 6.6, a standard set of densities are chosen at regular intervals in order to map the general stability behavior of the initial condition. Increasing and decreasing density is typically destabilizing and stabilizing respectively, and very low densities tend to slow down the rate of change for all aspects of the

response. An iterative approach is used to select additional densities for new test points in an effort to hone in on the neutrally stable condition. This inevitably creates a large number of results with the same terminal response, but with varying rates of growth or decay. The relative strength of the response is still important information that can be used both for analysis and for predicting safe operational ranges in a wind tunnel.

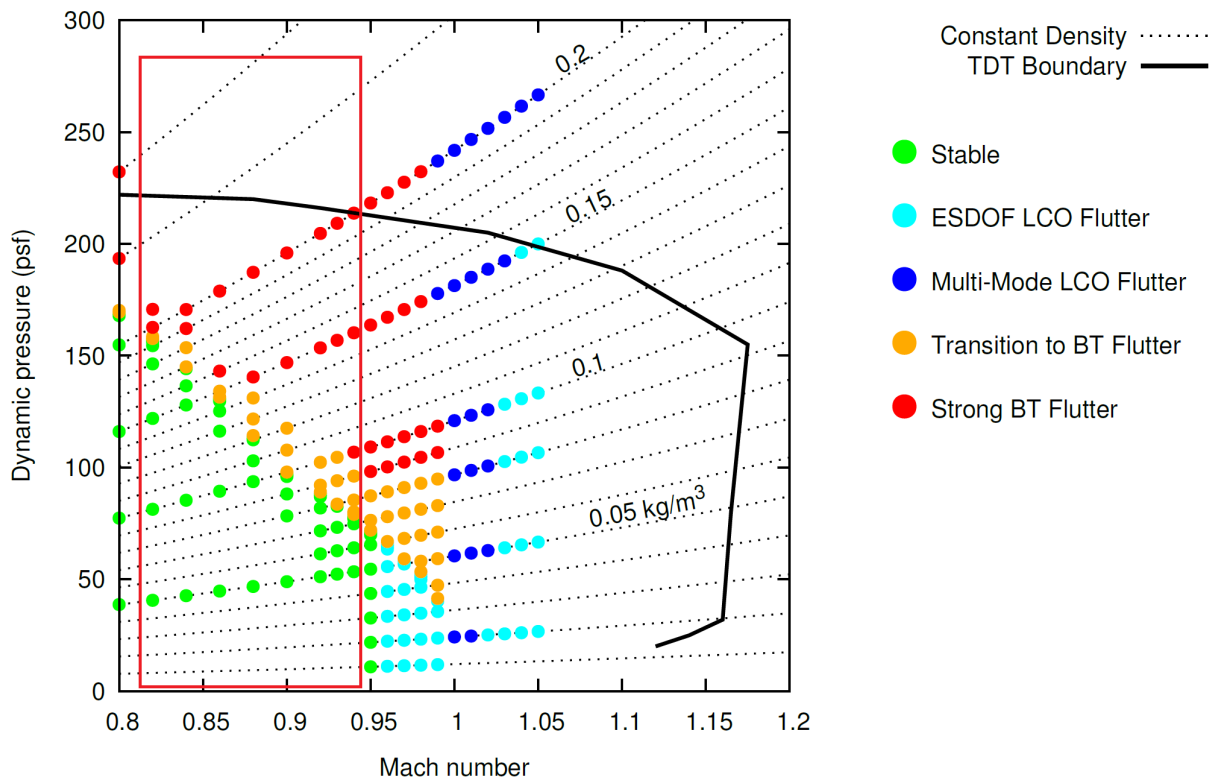


Figure 6.6: Indication of the Subsonic Stability Boundary free stream Mach number range.

6.3.1 FX-35: Subsonic Stability

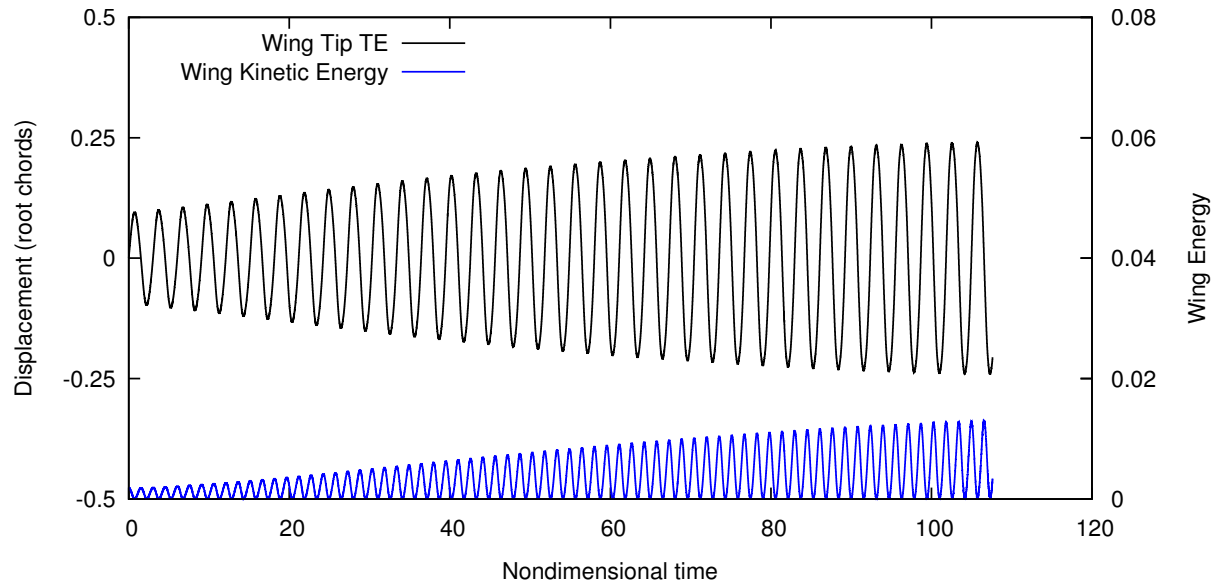


Figure 6.7: *FX-35: Typical subsonic unstable flutter response at the wing tip (Mach 0.93, Density 0.1 kg/m^3).*

In the subsonic region before the chimney, flutter behavior follows a predictable pattern. As Mach number increases, the neutrally stable density value decreases. Above this boundary, the response is progressively more unstable and vice versa below the boundary. Figure 6.7 shows a typical unstable flutter response with a moderate rate of growth for the FX-35 wing at Mach 0.93 and a density of 0.1 kg/m^3 . Even at a tip plunge of 0.25 root chords, the response is not overly alarming for this particular version of the FX-35 model, which is thinner and more flexible than usual. Still, the terminal result of this test point is most likely structural failure. Figure 6.8 shows the entire series of flutter responses for Mach 0.93 corresponding to the densities shown in Figure 6.4. These test points fall into one of three categories: Strong bending-torsion flutter, neutrally stable flutter, or a stable response.

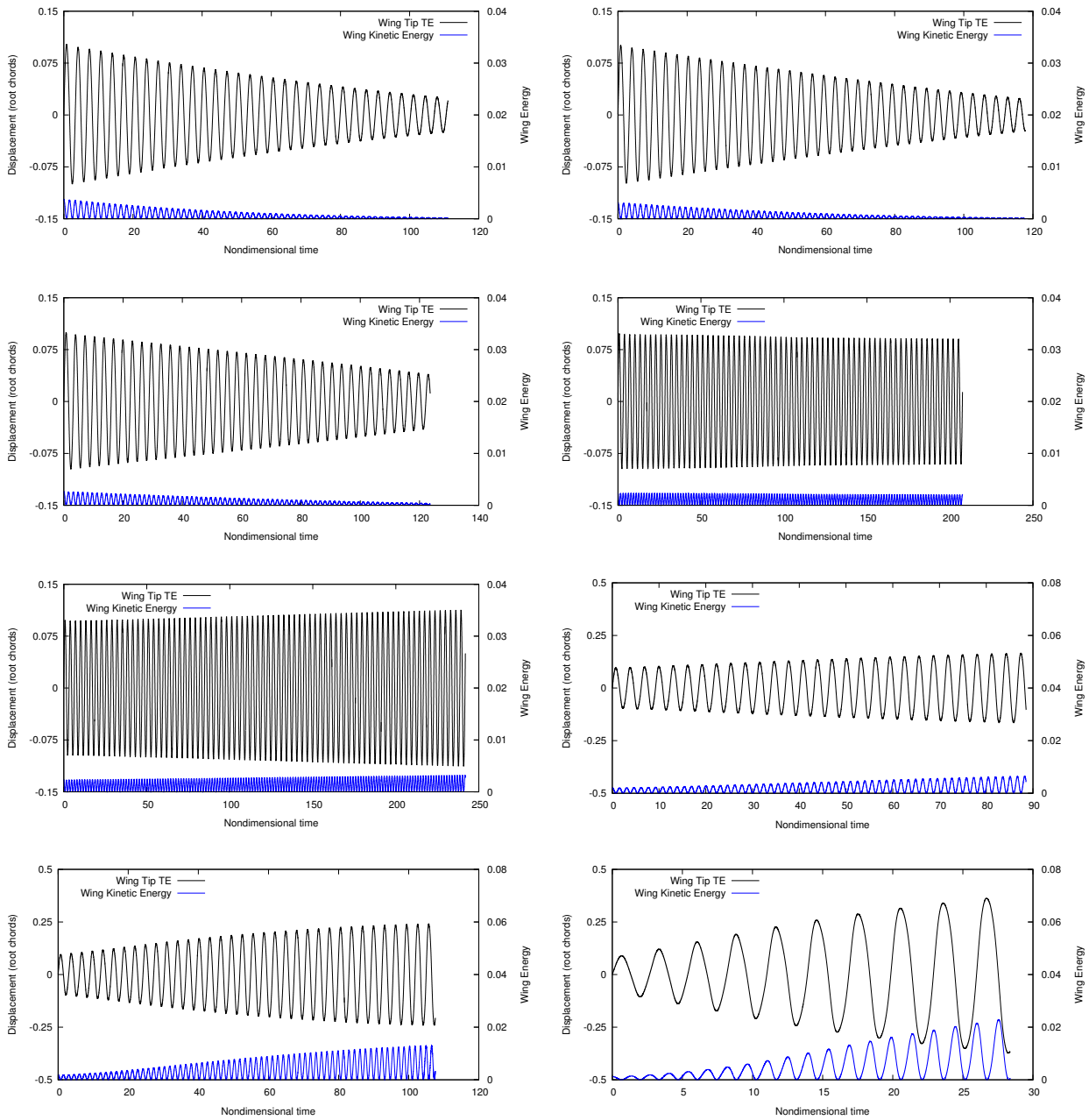


Figure 6.8: *The full range of FX-35 wing tip flutter responses from stable (top left) to unstable (bottom right) at Mach 0.93.*

Strong bending-torsion flutter refers to fast growing responses with mode coupling between first-bending and first-torsion that result in the structural failure of the model within a relatively short period of time. Any density value that is sufficiently higher than the flutter boundary value will result in strong bending-torsion flutter. Figures 6.9 and 6.10 show what happens to the wing tip plunge and pitch respectively when the density is increased to 0.2 kg/m^3 . The rate of growth in wing kinetic energy is substantially higher than at lower densities, manifesting in large amplitude oscillations in both pitch and plunge. If this case were run in a wind tunnel and resulted in the same response, it would almost certainly end in the loss of the model. Figure 6.11 shows two phase plots for wing tip plunge versus velocity and pitch, which can be useful for finding patterns in what seem like chaotic responses. In this case, there's nothing special to see; just an highly unstable response.

In many cases, it is difficult to notice the participation of the first-torsion mode, first because it contains relatively low kinetic energy compared to bending, and second because both first-bending and second-bending result in considerable wing tip pitch as a normal characteristic of their mode shapes. Figure 6.10 contains two combined responses corresponding to the two modes present. The low-frequency, high-amplitude oscillation is directly caused by the first-bending mode and is accordingly out of phase with the plunge response in Figure???. The high-frequency, low-amplitude oscillation is caused by the first-torsion mode, which manifests in the plunge response as a slight irregularity in the sinusoidal motion. Figure 6.12 shows the distribution of kinetic energy between the participating modes; with first-torsion barely making an appearance as first-bending dominates. The fact is, torsion modes tend to get overwhelmed by bending modes in the majority of cases in every form of output besides pitch plots.

Irregularities at the tail end of these plots are the result of the diminishing ability of the program to function as nodes are stretched and contorted beyond their intended limit.

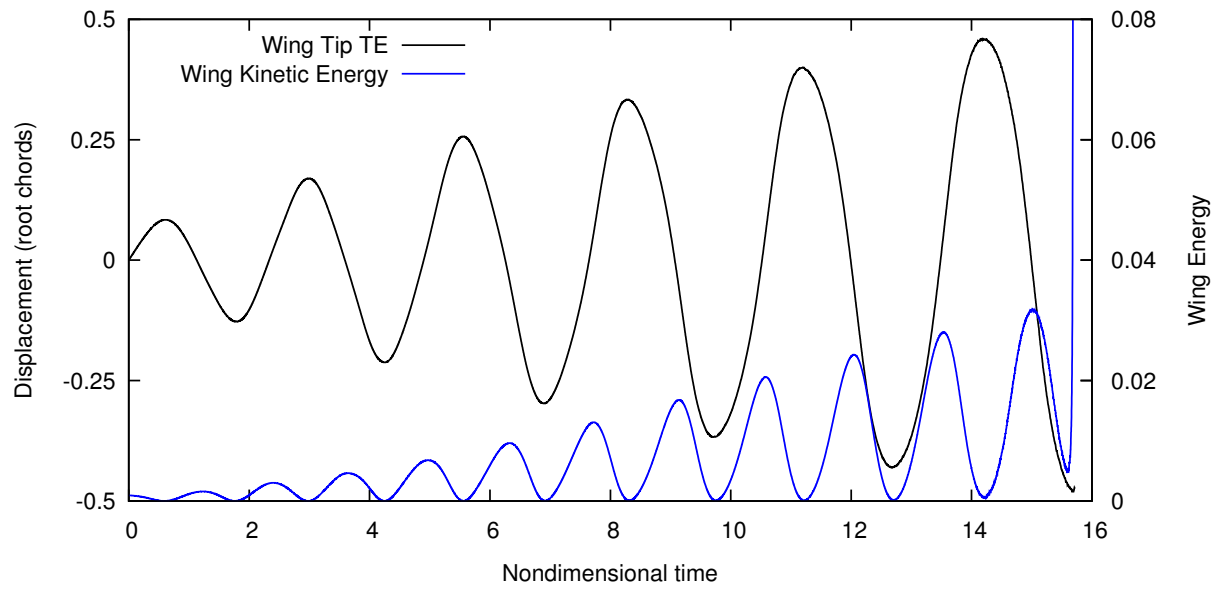


Figure 6.9: *FX-35: Strong bending-torsion flutter plunge response, demonstrating rapid amplitude growth at increased density (Mach 0.93, Density 0.2 kg/m³).*

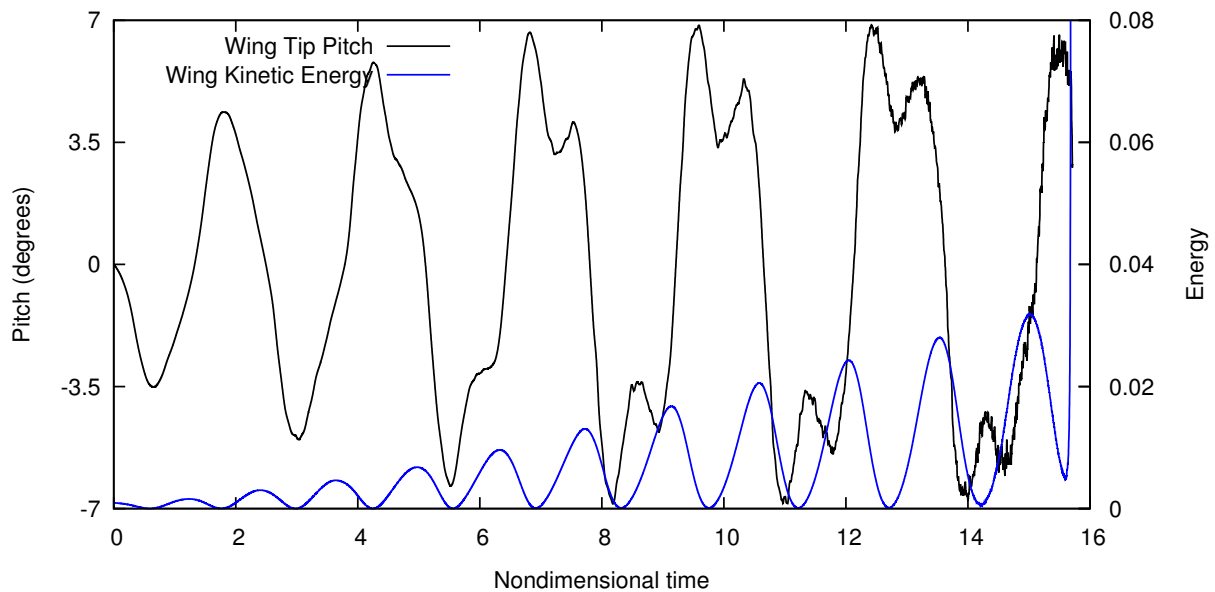


Figure 6.10: *FX-35: Strong bending-torsion flutter pitch response, demonstrating rapid amplitude growth at increased density (Mach 0.93, Density 0.2 kg/m^3).*

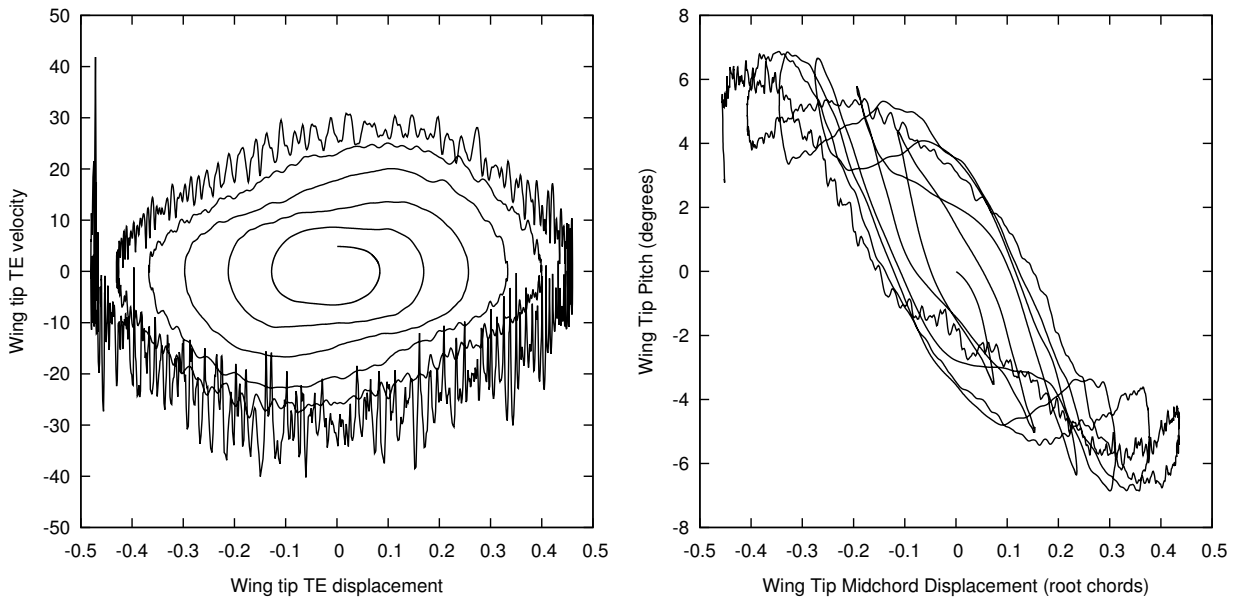


Figure 6.11: *FX-35: Phase plots corresponding to strong bending-torsion flutter (Mach 0.93, Density 0.2 kg/m^3).*

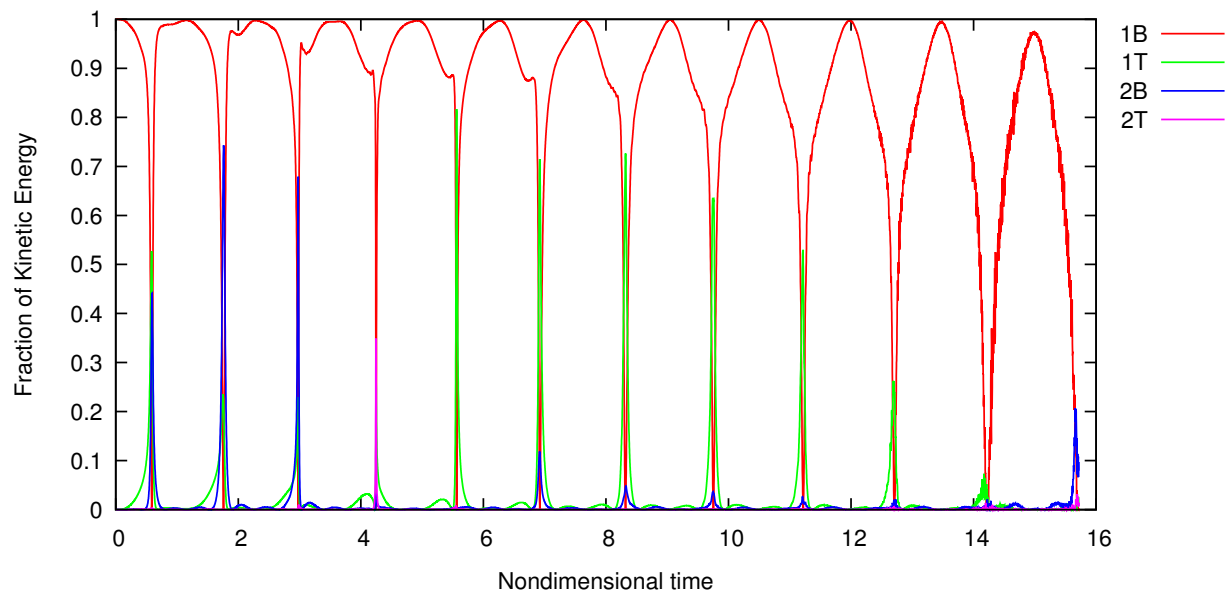


Figure 6.12: *FX-35: Kinetic energy distribution between natural modes for strong bending-torsion flutter (Mach 0.93, Density 0.2 kg/m³).*

Figures 6.13 through 6.16 show plunge and pitch plots for the flutter response on either side of stability boundary at densities of 0.079 kg/m³ and 0.08 kg/m³, respectively. The margin here is extremely narrow, with very slow decay observed below the boundary and very slow growth above it. It is possible for the stability boundary to exist over a range of densities that all exhibit a response with a neutrally stable amplitude. That is not the case here, as neither response shows any sign of tapering off at some asymptotic limit, meaning they are simply stable and unstable motion. It is evident from small irregularities in the pitch that these are still coupled responses between the first-bending and first-torsion modes.

Because the rate of growth is so small, this gives the opportunity to observe various patterns in the motion with a bit more precision. Figures 6.17 and 6.18 show the stable

case phase plots for the wing tip plunge versus velocity and pitch for the entire time domain and for a small subset of cycles. The wavering motion in the phase plots is due to the presence of both first-bending and first-torsion, but the regularity of the pattern suggests the torsion mode is not driving any part of the motion. The kinetic energy distribution, seen in Figure 6.19 confirm that the first-torsion mode is participating weakly. Erratic phase responses can be used as a gauge for the relative strength of involved modes; multi-mode responses can cause complicated wandering in the phase patterns, as will be seen later in this chapter.

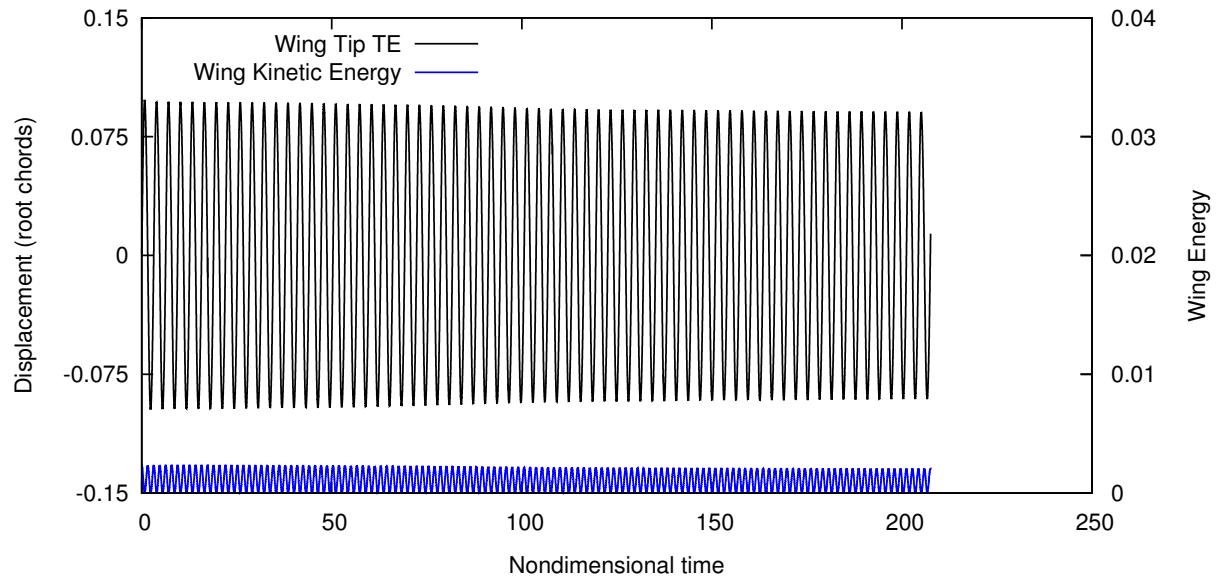


Figure 6.13: *FX-35: Weakly stable plunge response just below the flutter boundary (Mach 0.93, density 0.079 kg/m³).*

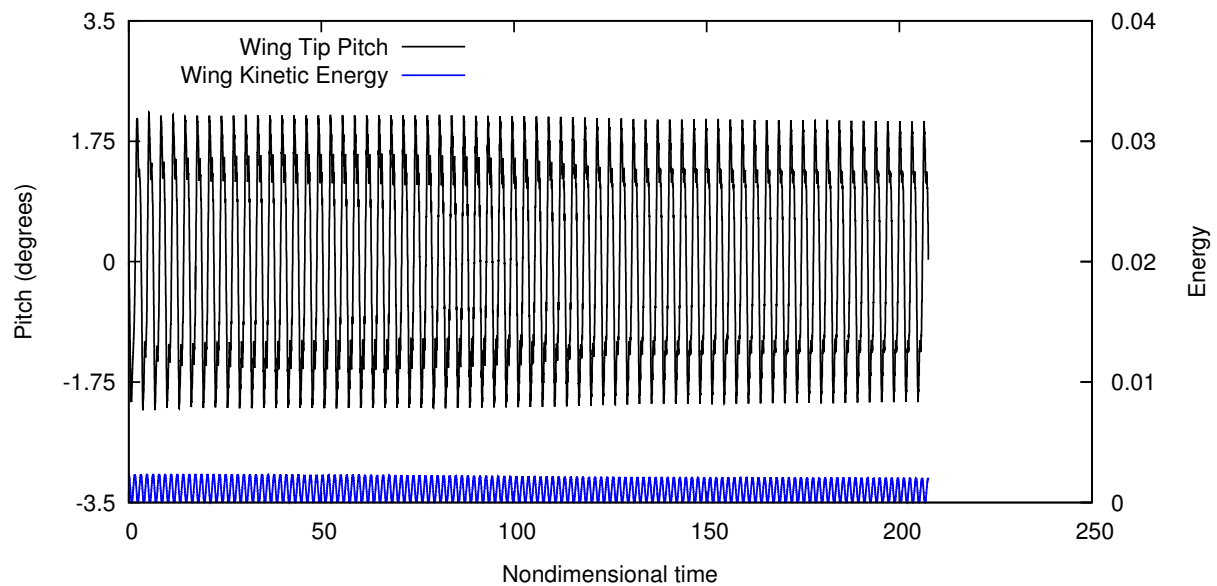


Figure 6.14: *FX-35: Weakly stable pitch response just below the flutter boundary, small hiccups in the response indicate first-torsion participation (Mach 0.93, density 0.079 kg/m³).*

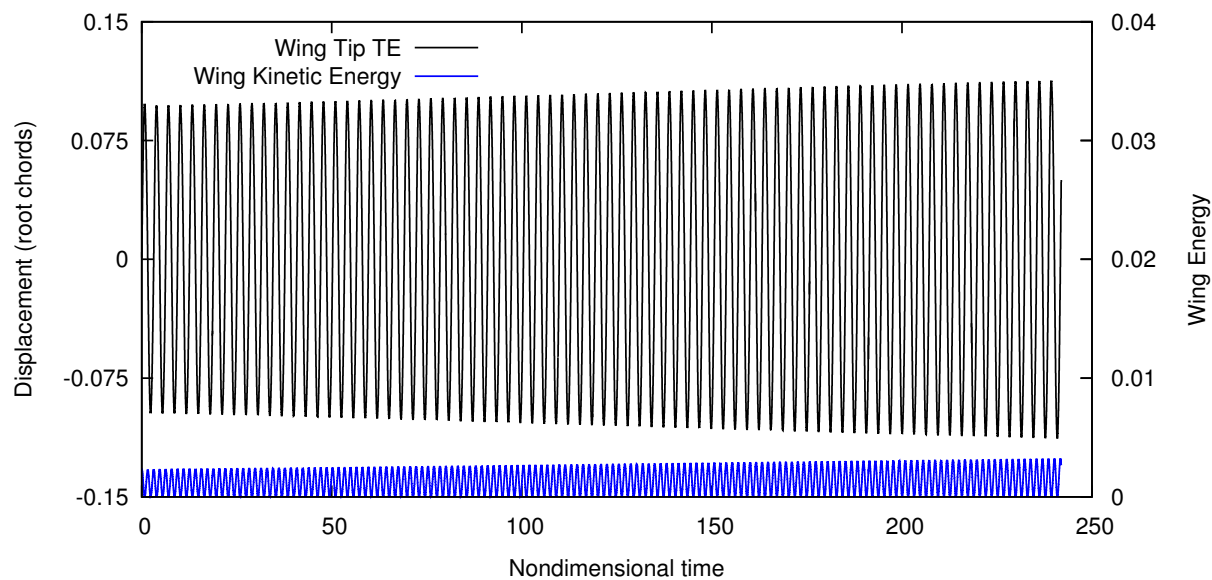


Figure 6.15: *FX-35: Weakly unstable plunge response just above the flutter boundary (Mach 0.93, density 0.08 kg/m³).*

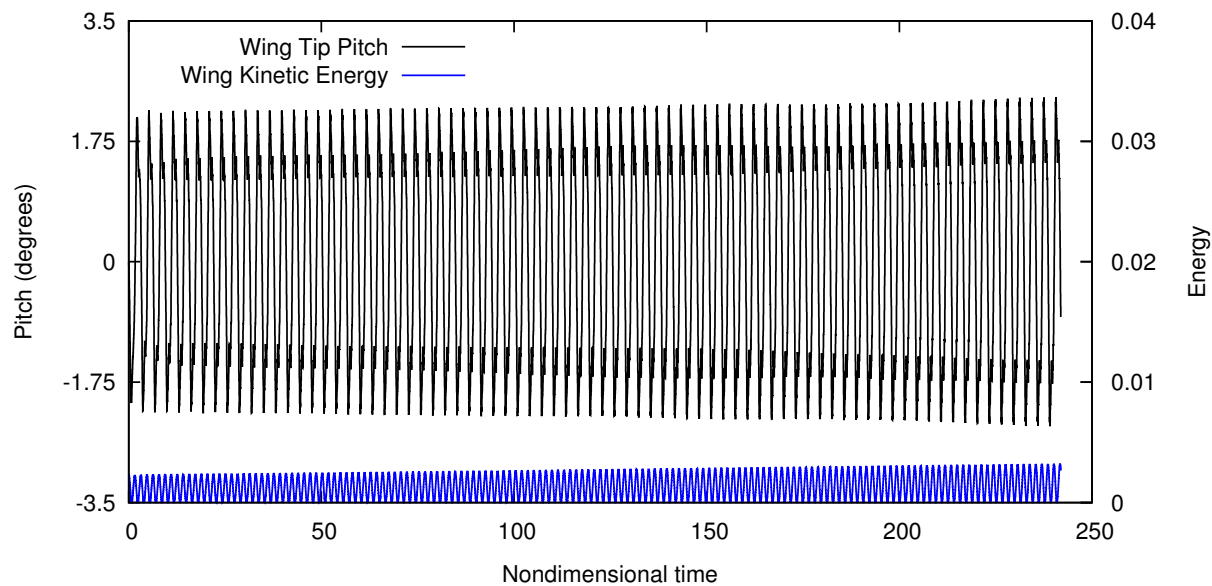


Figure 6.16: *FX-35: Weakly unstable pitch response just above the flutter boundary, small variations in the response indicate first-torsion participation here as well (Mach 0.93, density 0.08 kg/m³).*

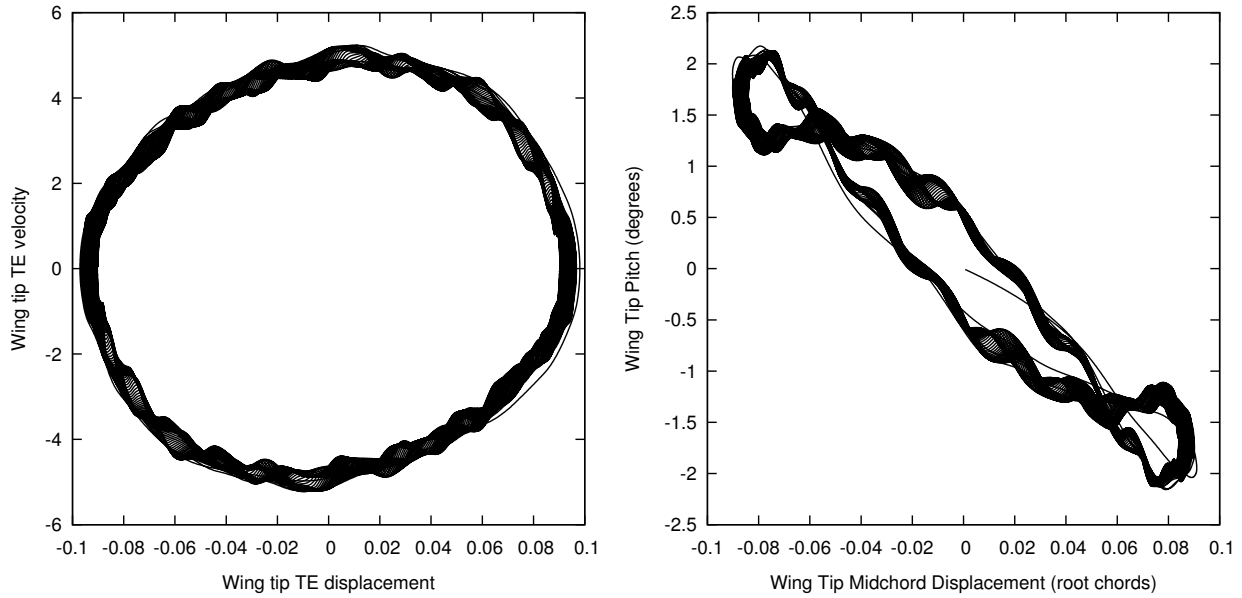


Figure 6.17: *FX-35: Phase plots corresponding to a weakly stable response just below the flutter boundary; showing the slight wavering caused by first-torsion participation (Mach 0.93, density 0.079 kg/m^3).*

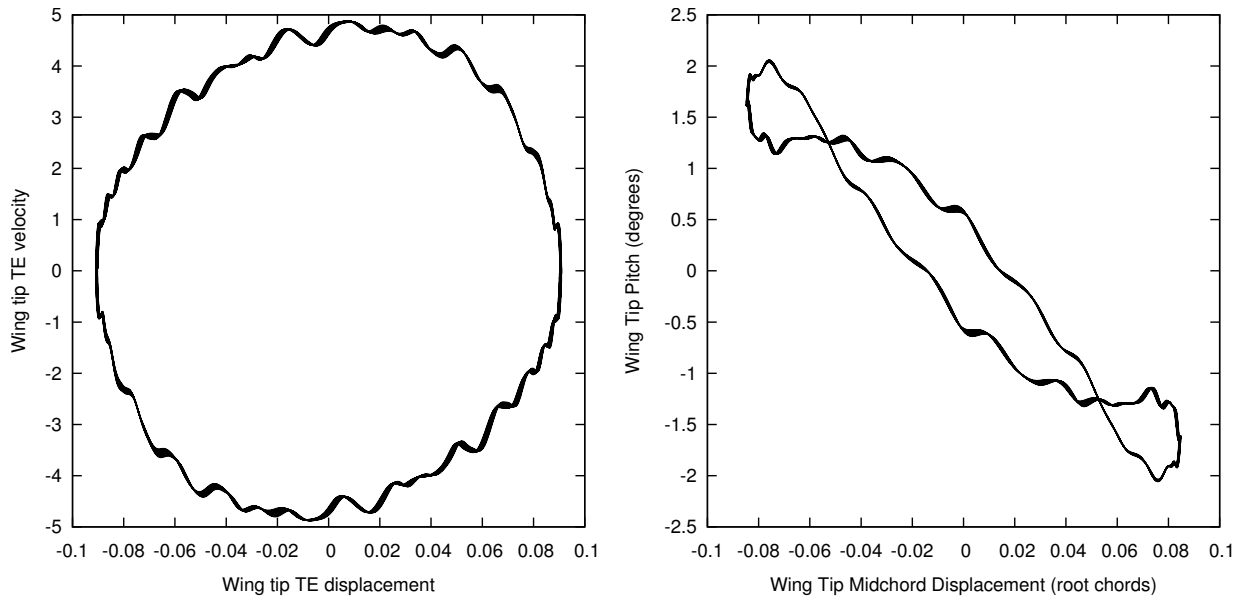


Figure 6.18: *FX-35: Phase plots from a smaller subset of cycles showing the lack of variation within the pattern between cycles at similar amplitudes. The weakness of this coupling effect is most likely due to the relative strength of the modes involved (Mach 0.93, density 0.079 kg/m^3).*

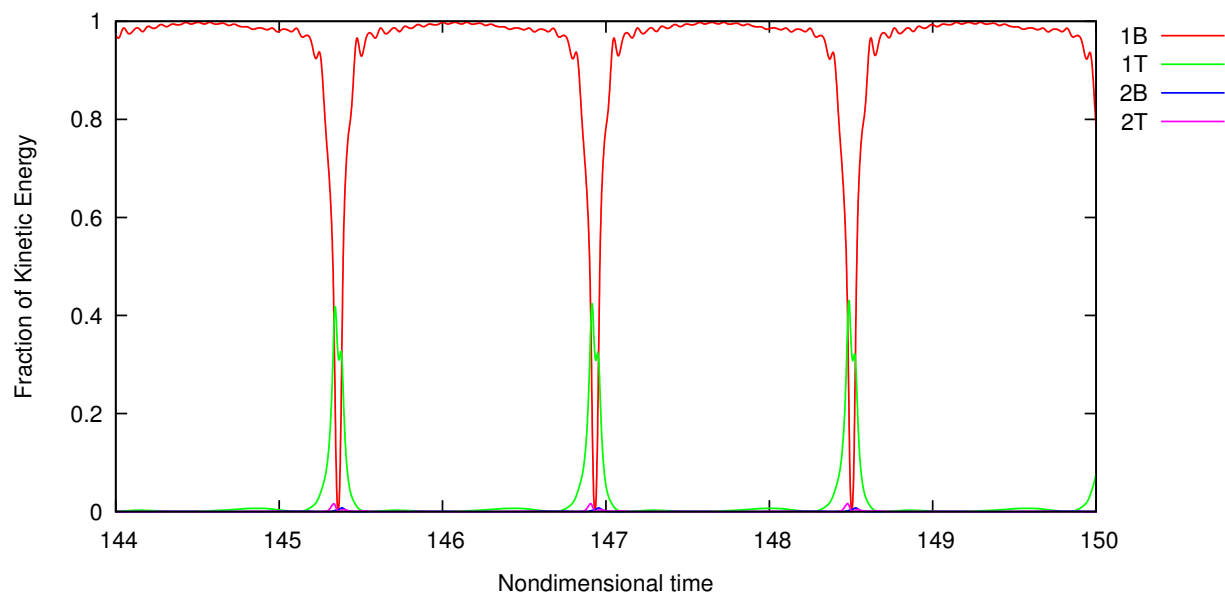


Figure 6.19: *FX-35: Distribution of kinetic energy by mode. Even at a neutrally stable condition, the first-torsion mode participates in the flutter response (Mach 0.93, density 0.079 kg/m³).*

Figures 6.20 through 6.22 show the general stable response for densities sufficiently below the flutter boundary. The steady state for most test points in this region is a decay to near-zero amplitude. If any non-zero steady state solutions do exist, they would be difficult to find due to the large number of test points and the slow speed at which steady state solutions emerge (often taking weeks of computation time to manifest). However, these would most likely be low amplitude flutter oscillations that are of academic interest and would not pose any real danger to either a wind tunnel model or a real aircraft. The distinguishing feature of the stable response is the muting of additional modes besides first-bending. It is clear from the displacement versus velocity phase plot that the wing tip motion transitions to a clean sinusoidal response with a steady rate of decay and no mode coupling.

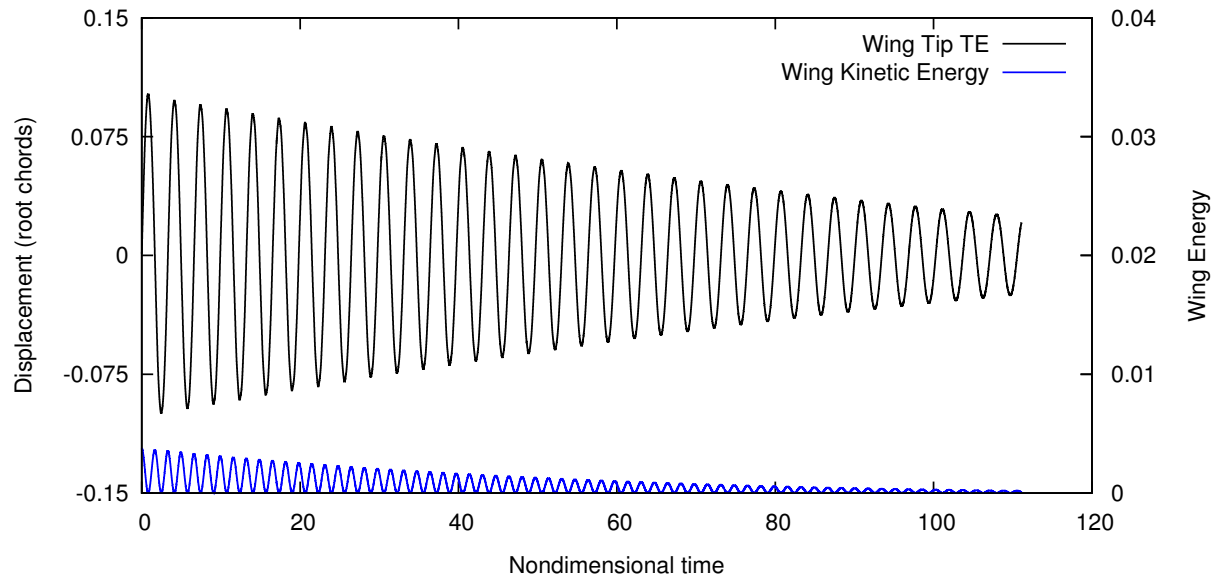


Figure 6.20: *FX-35: Stable plunge response below the flutter boundary (Mach 0.93, density 0.05 kg/m³).*

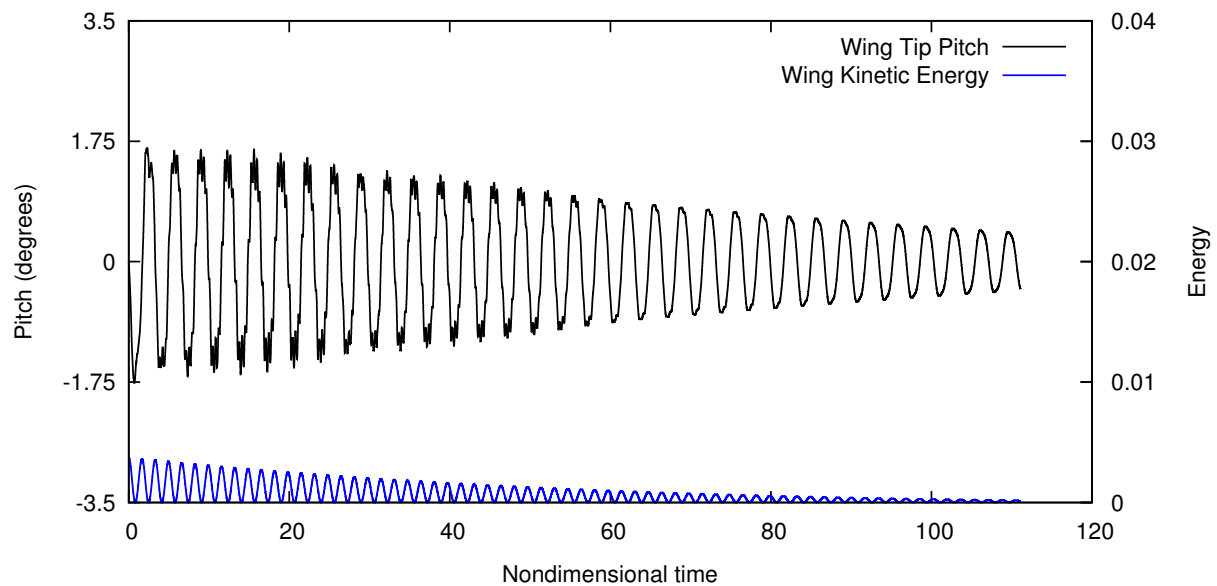


Figure 6.21: *FX-35: Stable pitch response below the flutter boundary (Mach 0.93, density 0.05 kg/m³).*

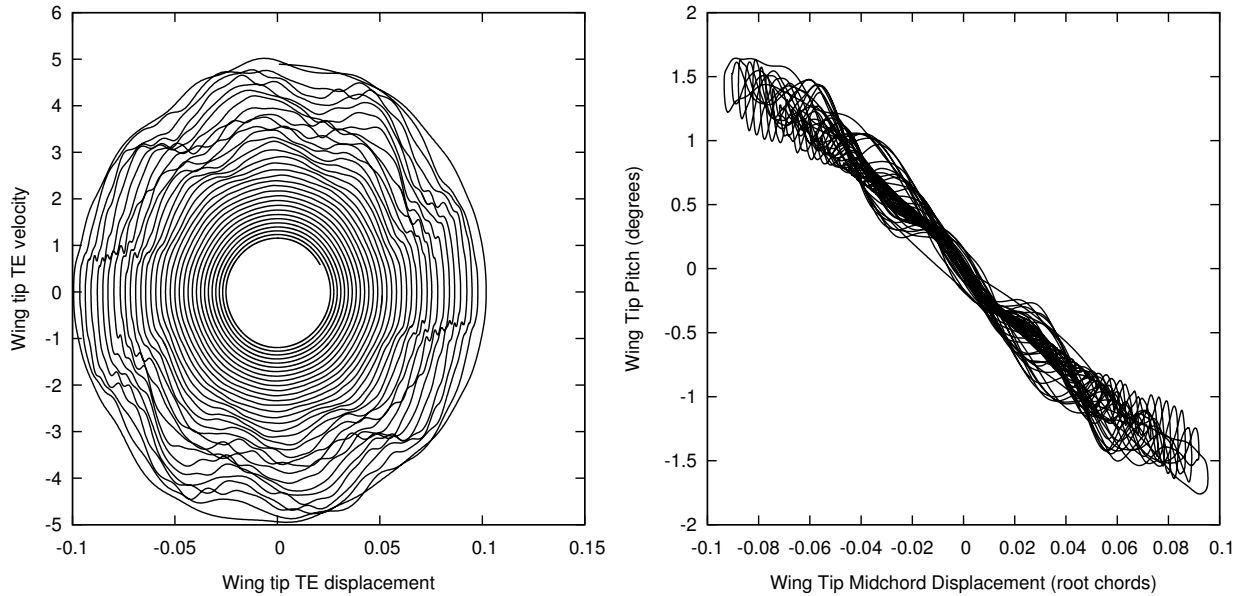


Figure 6.22: *FX-35: Phase plots corresponding to a stable response; the first-torsion mode drops out over time, as evidenced by the transition to a clean sinusoidal decay of the first-bending mode (Mach 0.93, density 0.05 kg/m³).*

6.3.2 F-Wing: Subsonic Stability

The flutter stability boundary for the F-Wing is very similar to that of the FX-35. The first bending mode is still dominant, the neutrally stable density value decreases towards zero as Mach number approaches one, and high densities result in extremely volatile responses. For the purpose of comparison, three conditions will be shown here to demonstrate the behavior of the F-Wing above, along, and below the stability boundary.

Figures 6.23 through 6.26 show a strong, unstable flutter response at Mach 0.93 and a density of 0.2 kg/m³. Apart from the rapid growth in the amplitude of the response, the F-Wing, like the FX-35, encounters first-torsion coupling, manifesting as a proclivity toward reduced pitch amplitude near the peak of the plunge response. This creates a small dip in

the pitch plots, as well as a hooking or looping motion at the end of the phase plot. At especially large amplitudes, the solution begins to break down as the mesh distorts beyond the ability of the program to accommodate.

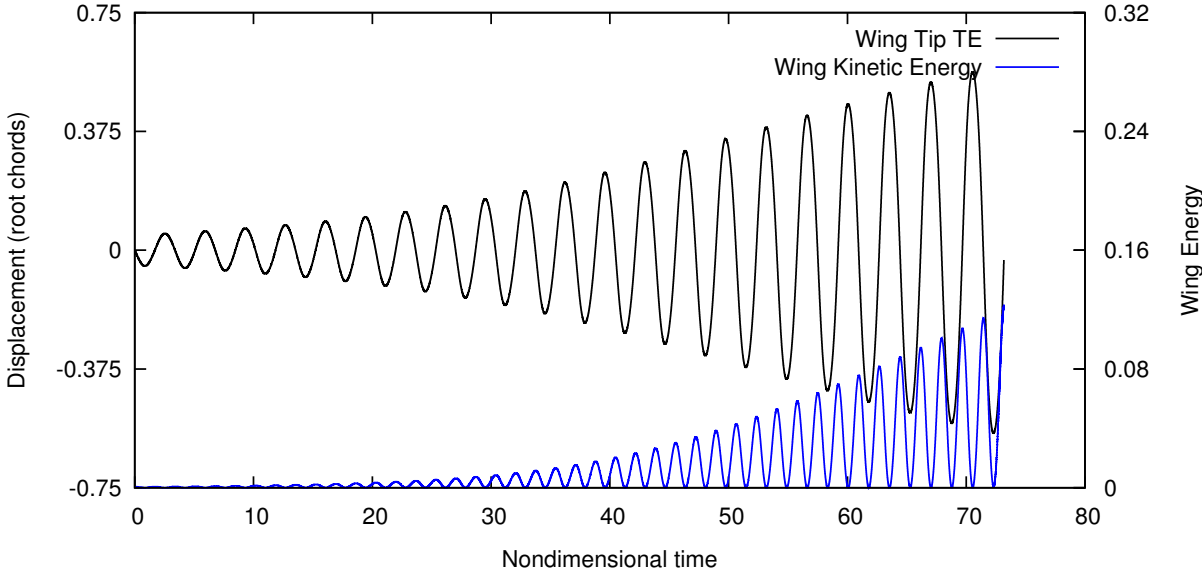


Figure 6.23: *F-Wing: Strong bending-torsion flutter plunge response, demonstrating rapid amplitude growth at increased density (Mach 0.93, density 0.2 kg/m³).*

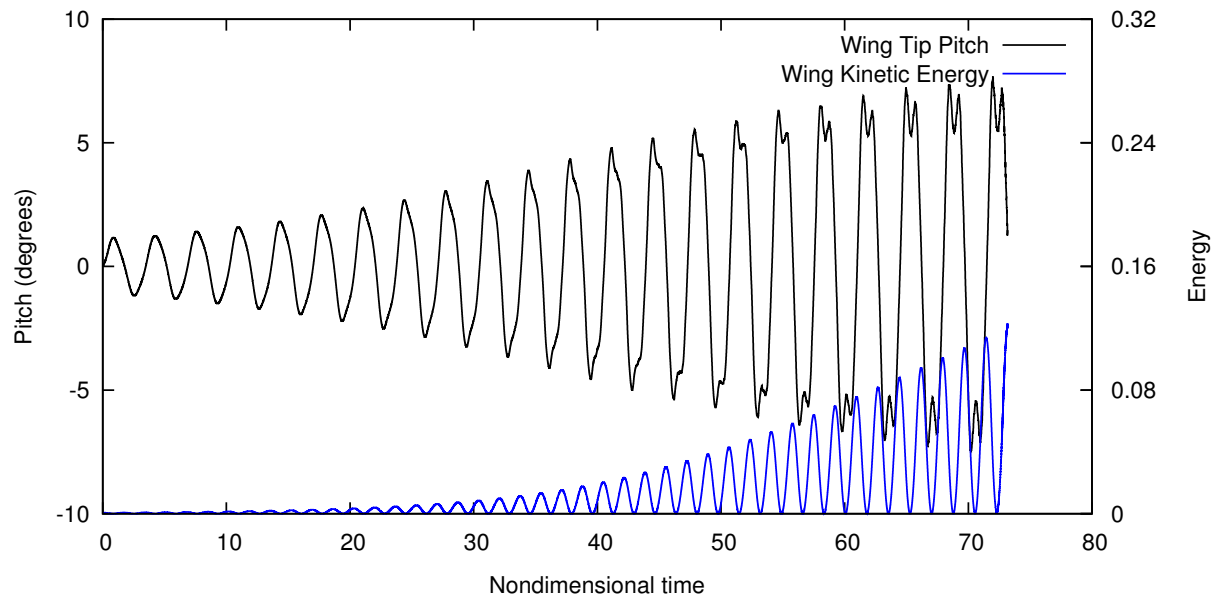


Figure 6.24: *F*-Wing: Strong bending-torsion flutter pitch response, showing first-torsion coupling with the dominant first-bending mode (Mach 0.93, density 0.2 kg/m^3).

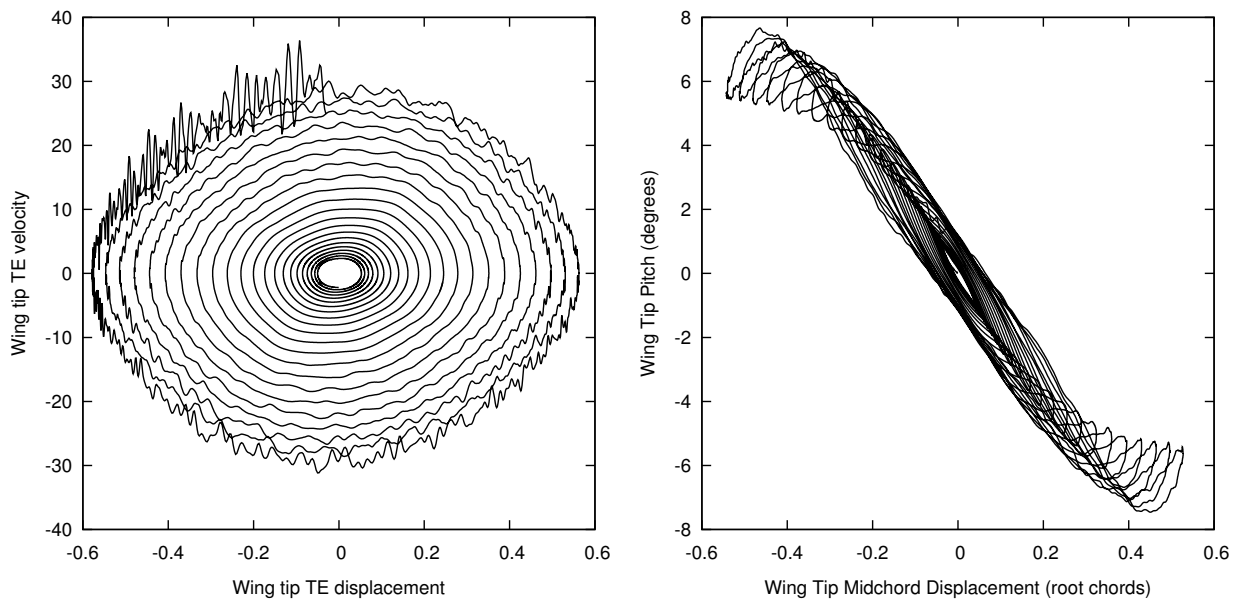


Figure 6.25: *F*-Wing: Phase plots corresponding to strong bending-torsion flutter (Mach 0.93, density 0.2 kg/m^3).

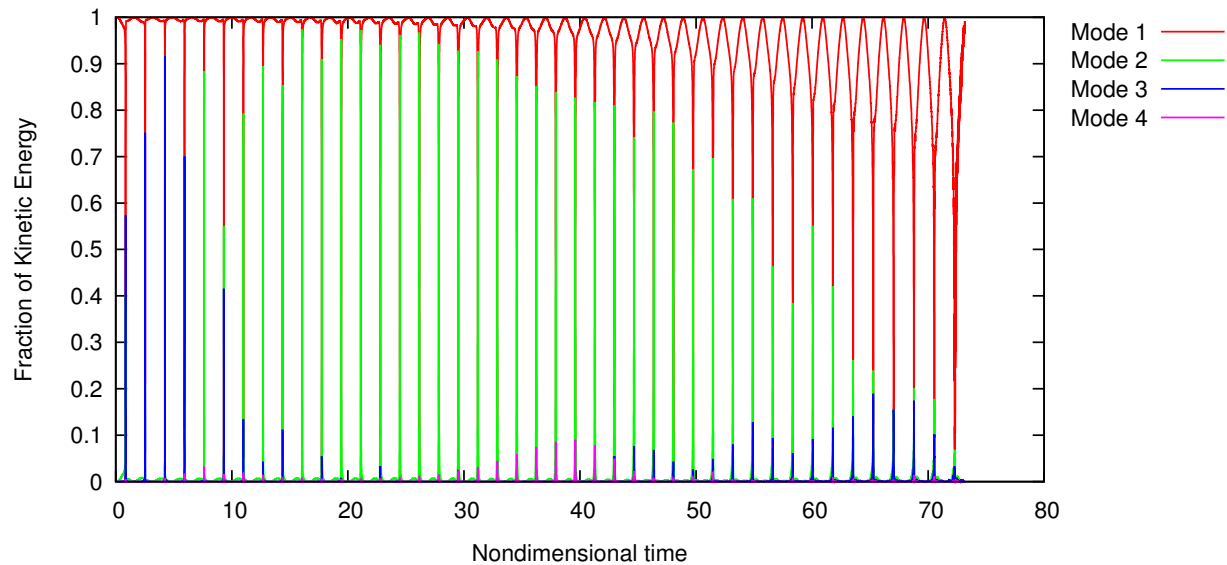


Figure 6.26: *F-Wing: Distribution of kinetic energy by mode (Mach 0.93, density 0.2 kg/m³).*

Figures 6.27 through 6.30 show a neutrally stable response on the flutter boundary at Mach 0.93 and a density of 0.13 kg/m³. The response of the F-Wing is noticeably smoother than the FX-35. This is due to the absence of first-torsion from the stability boundary; it grows in participation with increasing density. By contrast, the FX-35 only shows pure first-bending behavior for stable responses, where the displacement versus velocity phase plots become more circular.

Figures 6.31 through 6.34 show a stable response below the flutter boundary at Mach 0.93 and a density of 0.05 kg/m³. There's not much to say here apart from the aesthetically pleasing quality of the graphs. The response appears to be a decay of a pure first-bending mode.

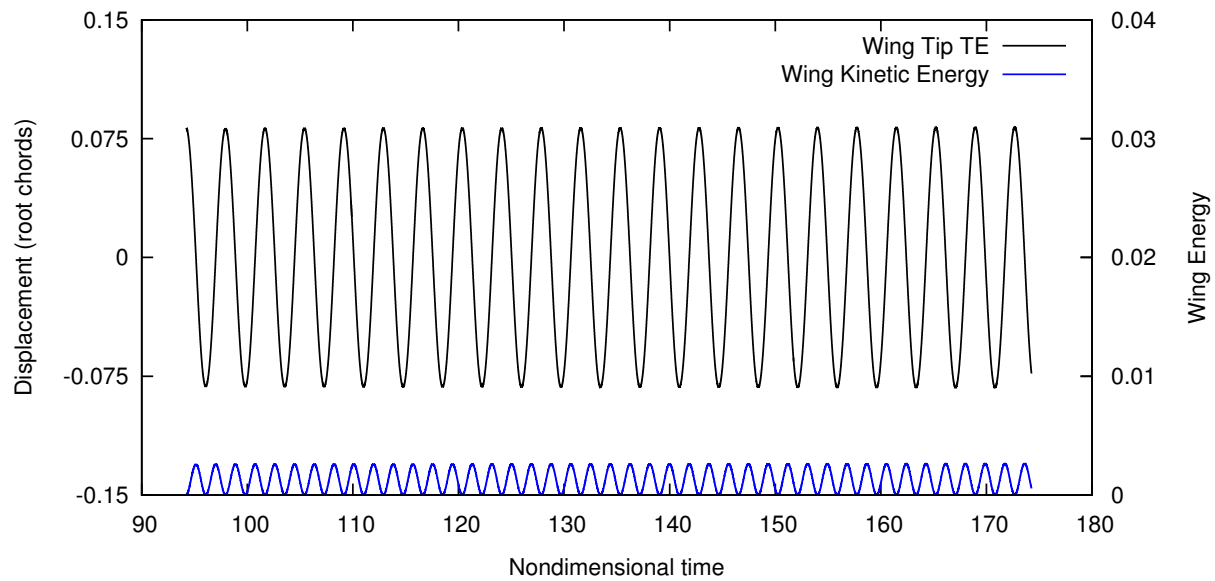


Figure 6.27: *F-Wing: Neutrally stable flutter plunge response (Mach 0.93, density 0.13 kg/m³).*

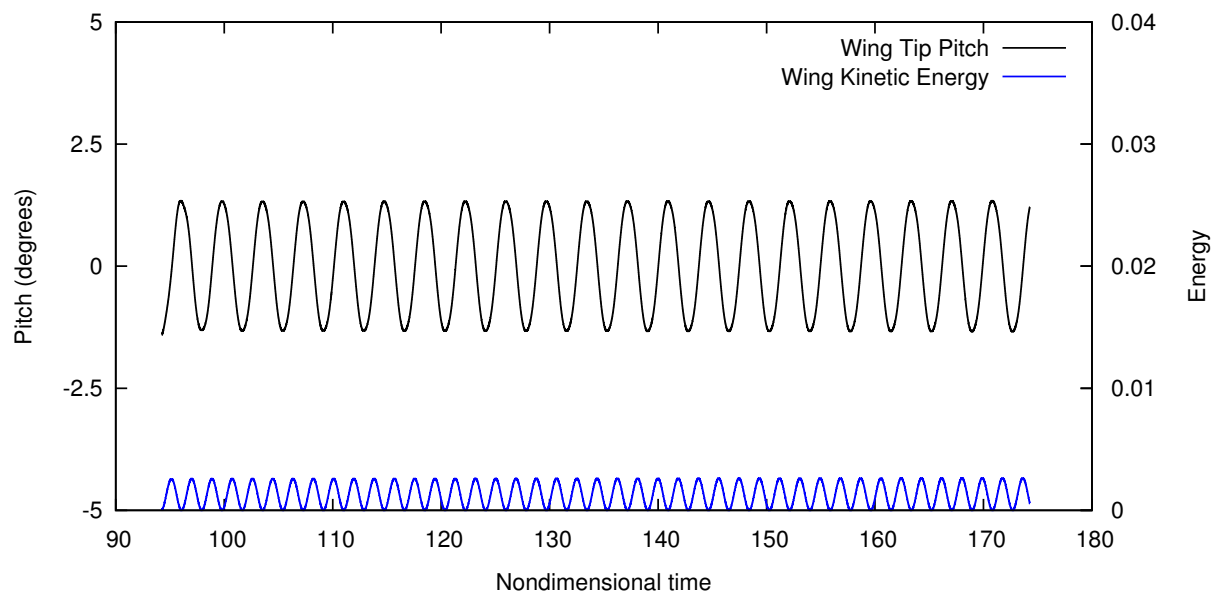


Figure 6.28: *F-Wing: Neutrally stable flutter pitch response (Mach 0.93, density 0.13 kg/m³).*

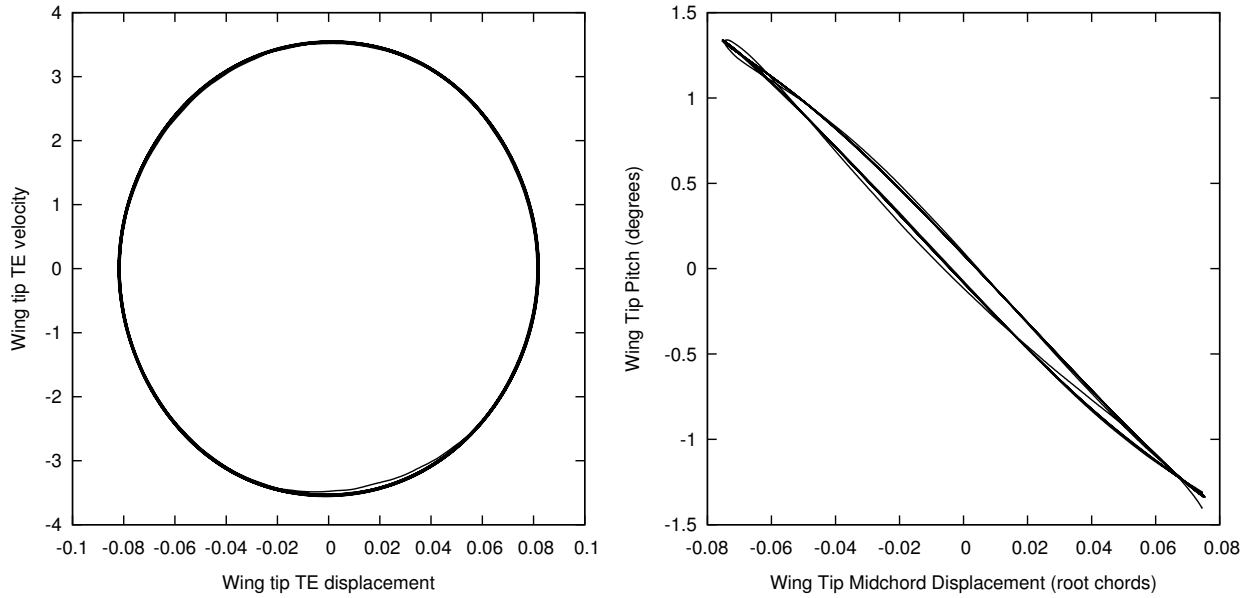


Figure 6.29: *F-Wing: Phase plots corresponding a neutrally stable response; the smooth response shows little to no evidence of mode coupling (Mach 0.93, density 0.13 kg/m³).*

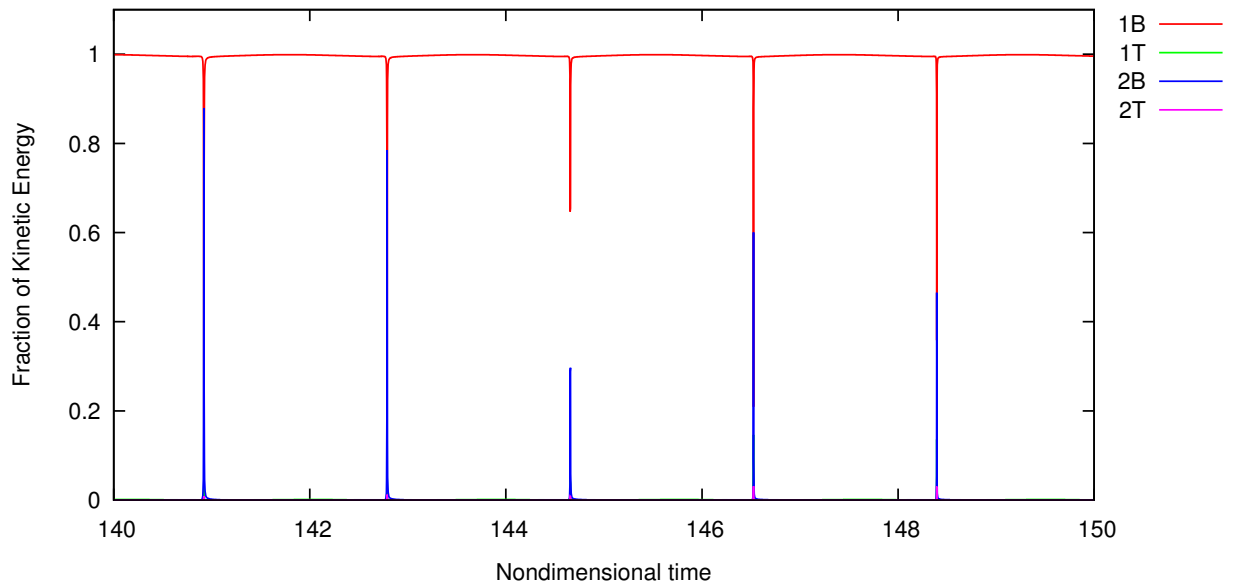


Figure 6.30: *F-Wing: distribution of kinetic energy by mode, the response is almost purely first-bending (Mach 0.93, density 0.13 kg/m³).*

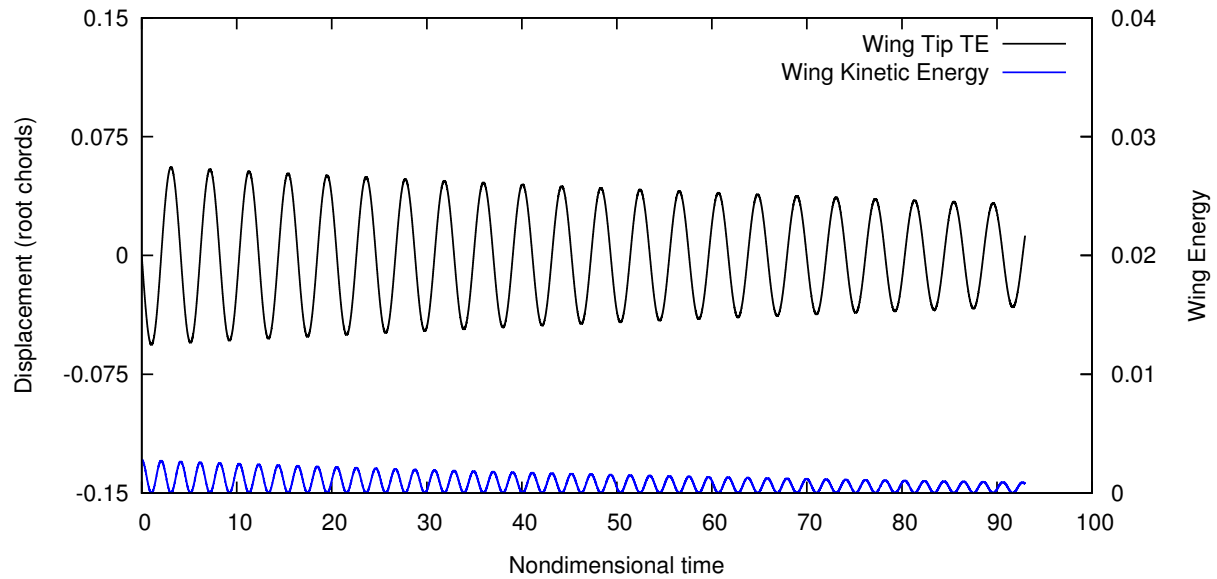


Figure 6.31: *F-Wing: Stable plunge response (Mach 0.93, density 0.05 kg/m³).*

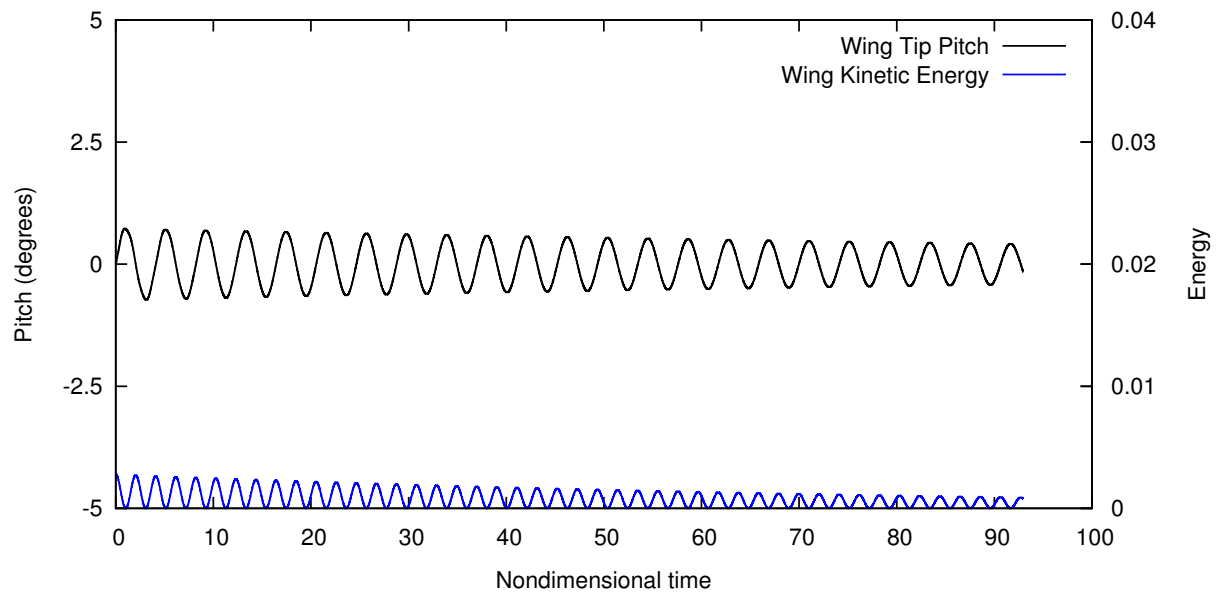


Figure 6.32: *F-Wing: Stable pitch response (Mach 0.93, density 0.05 kg/m³).*

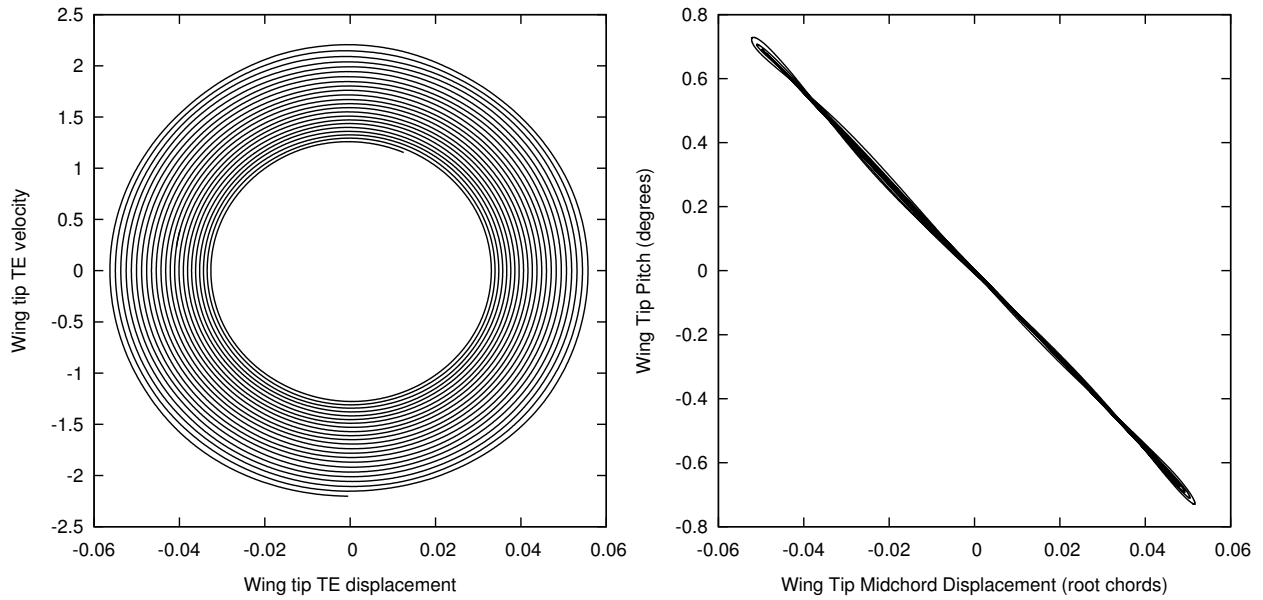


Figure 6.33: *F-Wing*: Phase plots corresponding to a stable response (Mach 0.93, density 0.05 kg/m³).

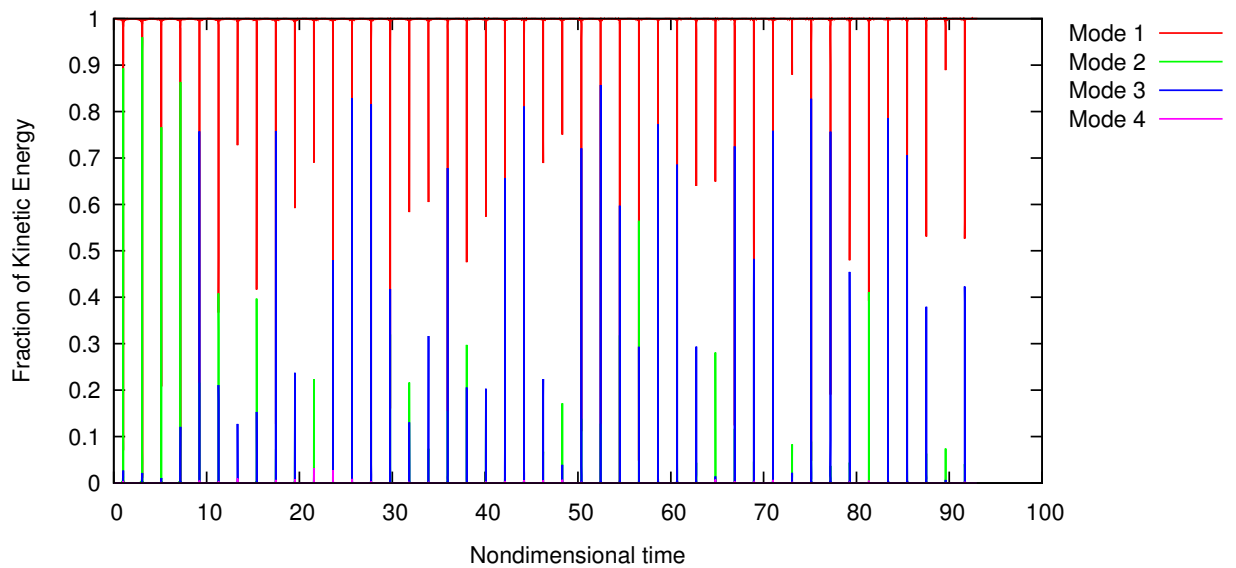


Figure 6.34: *F-Wing*: Distribution of kinetic energy by mode (Mach 0.93, density 0.05 kg/m³).

Identifying the stability boundary and strength of unstable responses is a fairly quick and simple exercise. Generally, all unstable flutter responses result in crashing the code (synonymous with breaking the model in a wind tunnel); it's only a matter of how long it takes the response to grow. Stable conditions either asymptotically approach zero or begin to show signs of transitioning to a different type of response through a change in modal participation. Transitions can take weeks or months of continuous computation to emerge; one can never be certain that some unknown solution isn't hiding between data points or farther along in time. The majority of long term computation was invested in low density test points between Mach 0.95 and Mach 1.00, in a region designated as the "chimney", where a known mode transition is expected to occur.

6.4 Chimney Transition

The transition from the initial condition to clear chimney behavior can take a long time to manifest, but it has a certain "you'll know it when you see it" quality. Any subsonic test point at low density is characterized by the slow decay of the first-bending mode initial condition, which continues down to a near negligible amplitude. What's leftover in the steady state is not noise, but instead is a clearly defined second-bending response. What determines the boundary of the chimney region is whether or not the second-bending steady state suddenly grows to a neutrally stable finite amplitude. The new amplitude is generally much smaller than it would be in a neutrally stable first-bending response, but it is still larger than mere noise. Notably, the steady state solution also follows limit-cycle behavior, making it the first response that can properly be called a limit-cycle oscillation (LCO). The LCO response

appears suddenly once the Mach number threshold is crossed and continues down to near-zero density, creating a chimney shape in the stability graph. The range of Mach numbers for the chimney transition is shown in Figure 6.35.

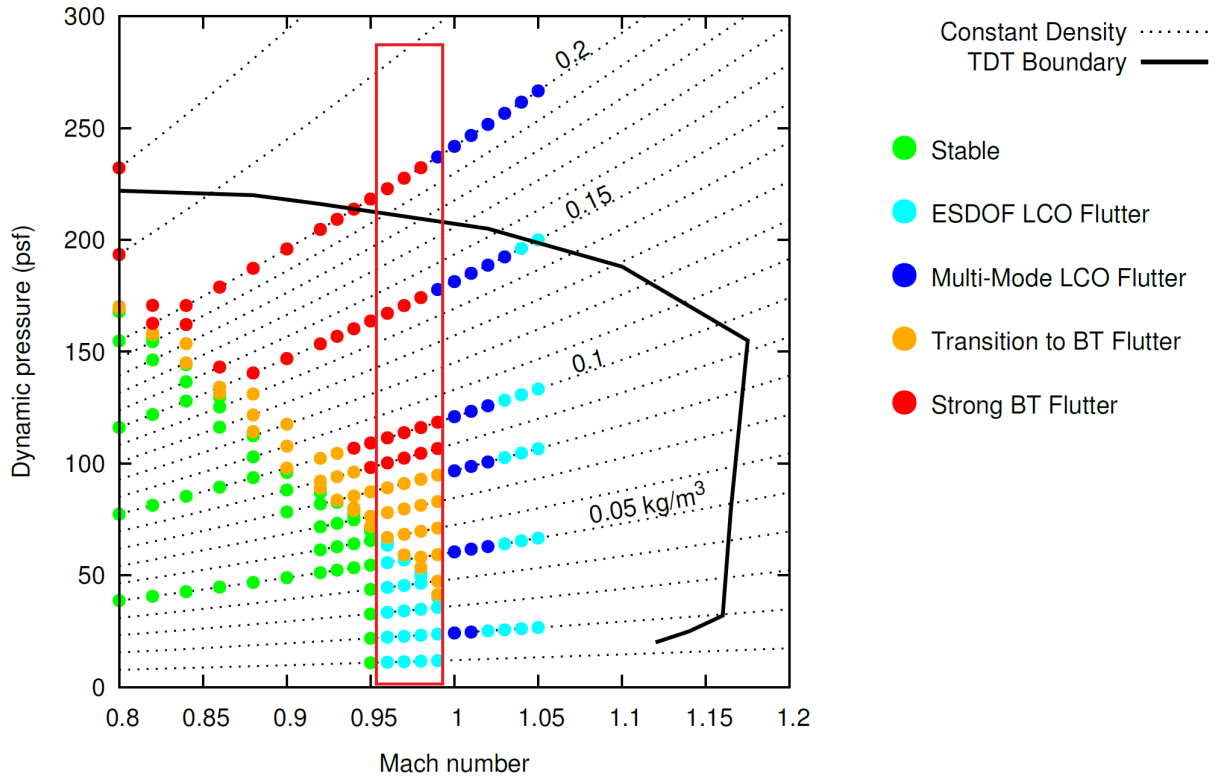


Figure 6.35: Indication of the Chimney Transition free stream Mach number range.

6.4.1 FX-35: Chimney

Figures 6.36 through 6.39 show long term stable responses for wing tip plunge and pitch from a first-bending initial condition on either side of the chimney transition Mach number. Outside the chimney, at Mach 0.95, both plunge and pitch asymptotically approach zero. Inside the chimney, at Mach 0.96, the response eventually transitions to a small, finite amplitude for both plunge and pitch. Figure 6.40 shows a series of plunge and pitch chimney

transitions for Mach 0.96 through Mach 0.99. Higher Mach numbers transition more quickly, but the final amplitudes are similar across all test points. The steady state for every chimney transition is an LCO dominated by the second-bending mode.

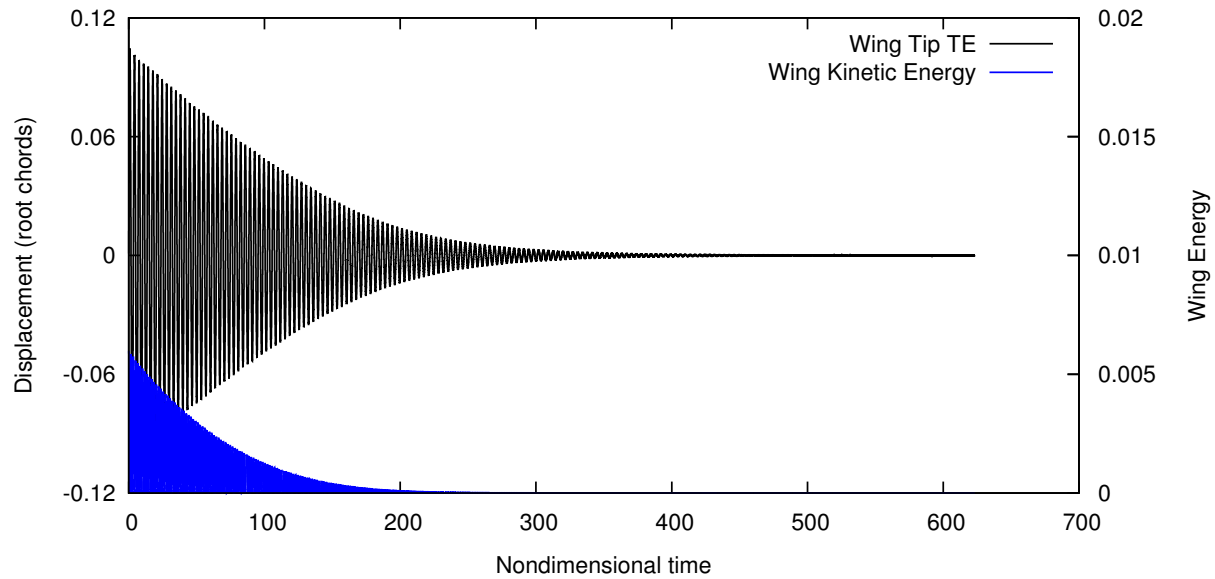


Figure 6.36: *FX-35: Steady state plunge asymptotically approaching zero (Mach 0.95, density 0.03 kg/m^3).*

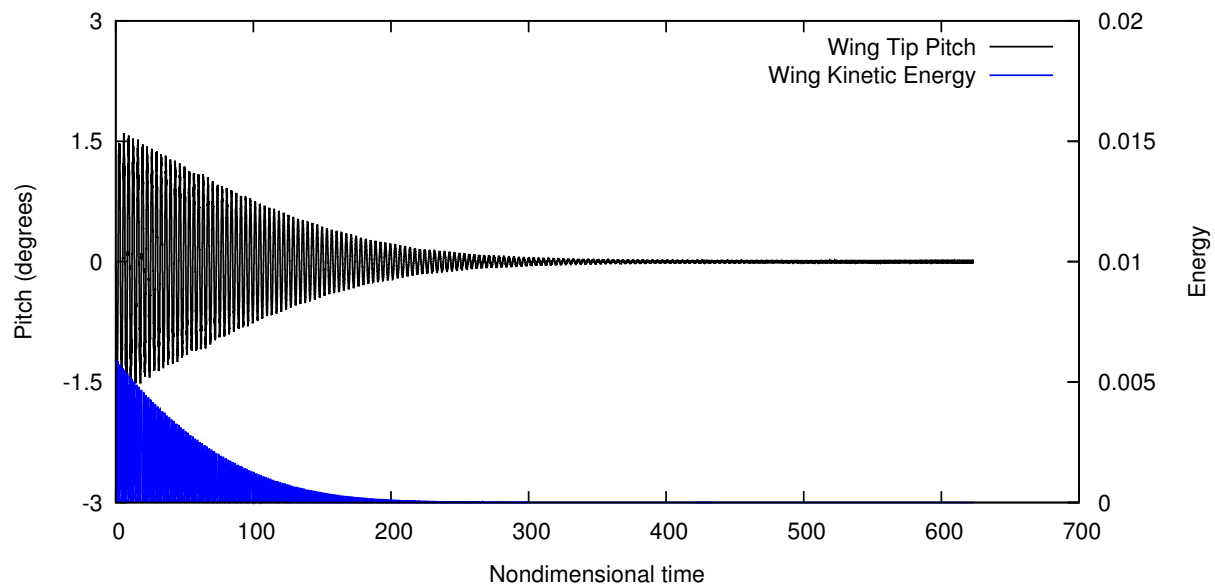


Figure 6.37: *FX-35: Steady state pitch asymptotically approaching zero (Mach 0.95, density 0.03 kg/m^3).*

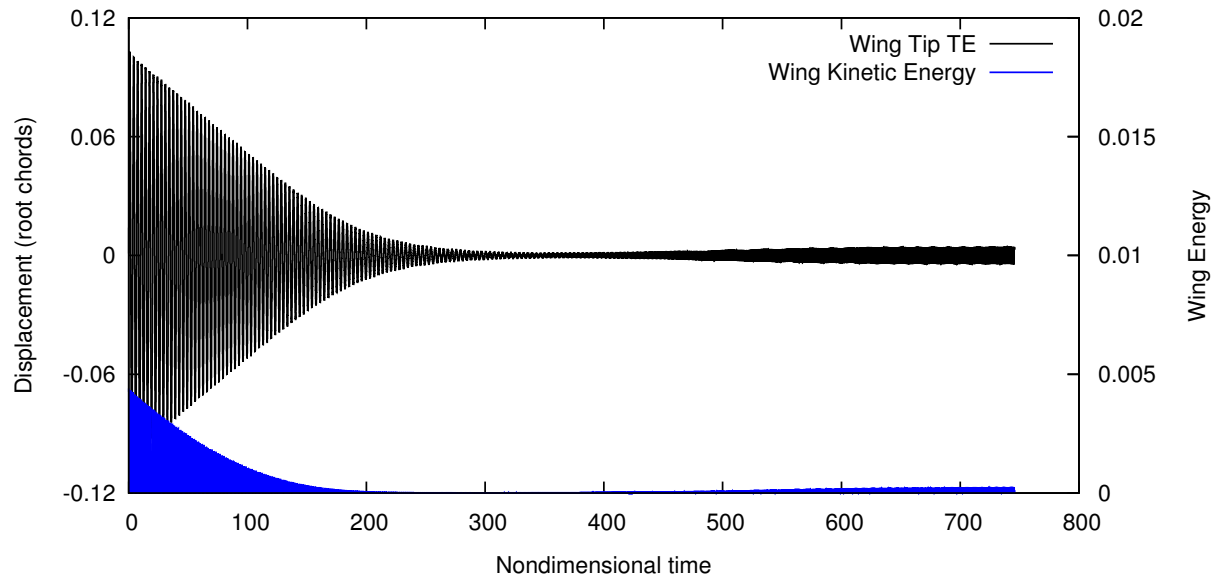


Figure 6.38: *FX-35: Steady state plunge transitioning to a neutrally stable second-bending mode (Mach 0.96, density 0.04 kg/m³).*

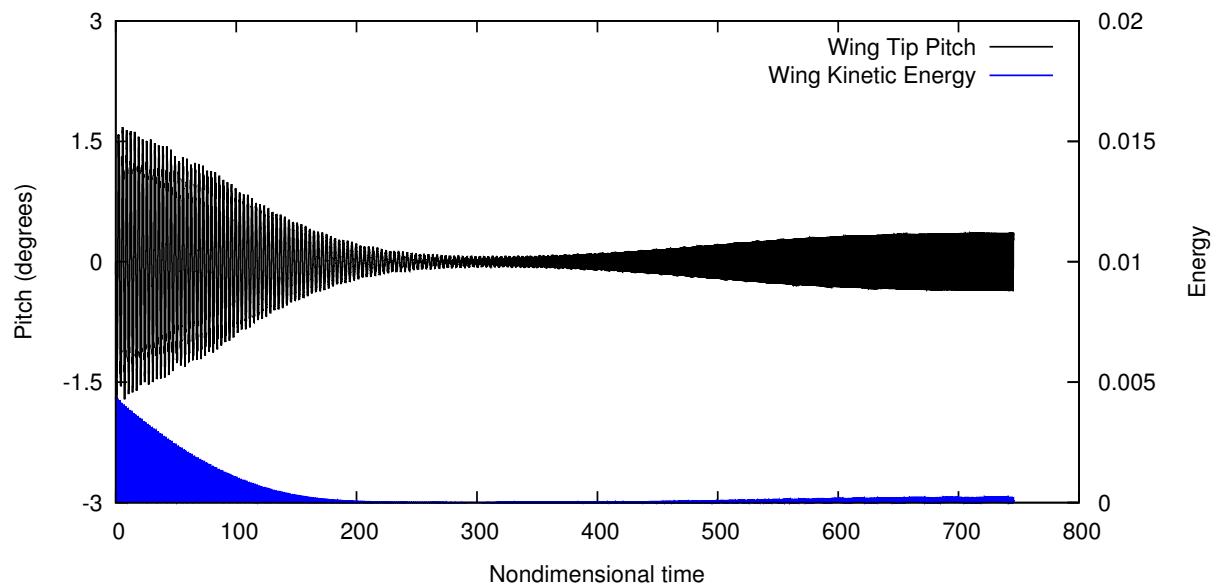


Figure 6.39: *FX-35: Steady state pitch transitioning to a neutrally stable second-bending mode (Mach 0.96, density 0.04 kg/m³).*

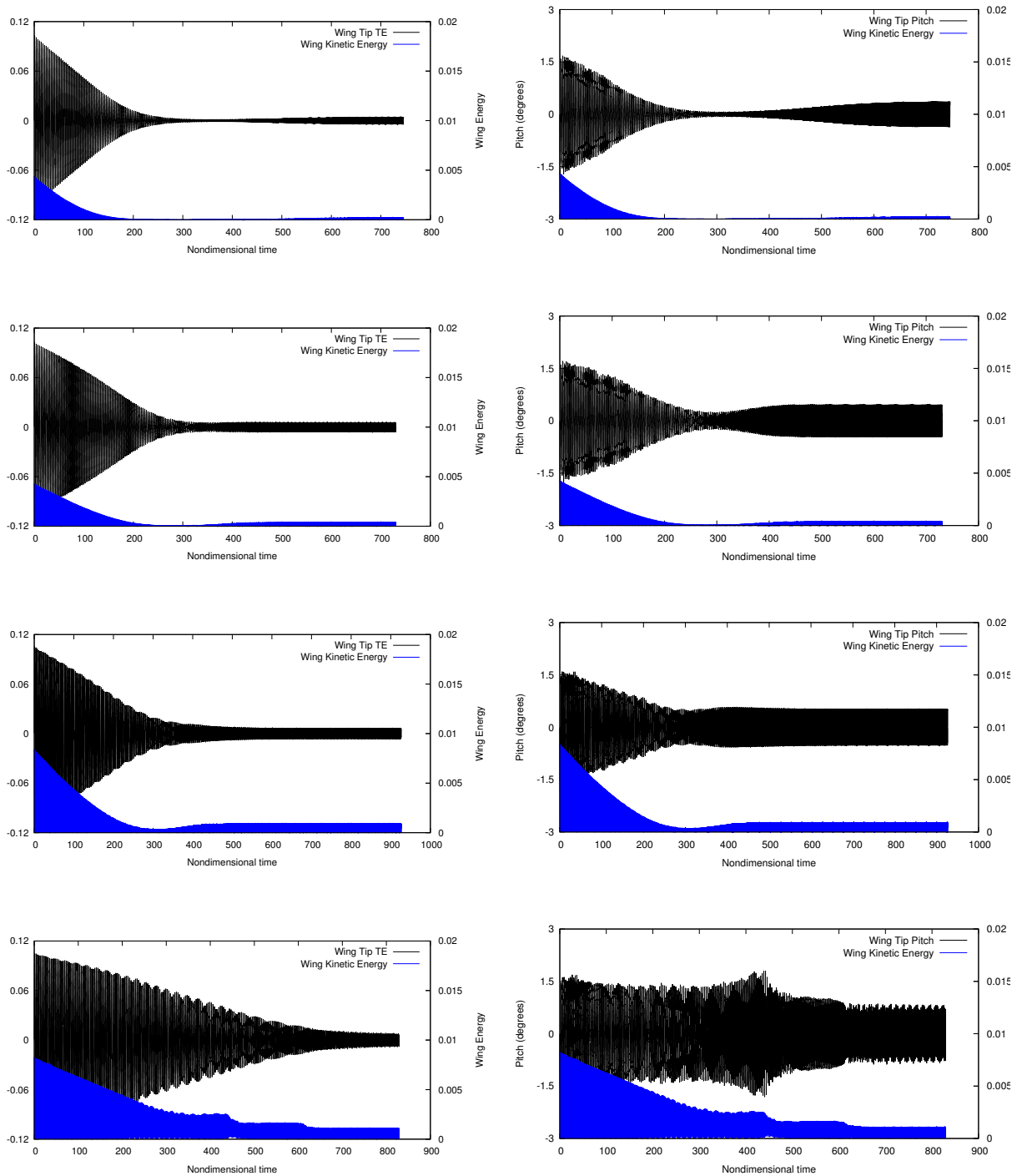


Figure 6.40: *FX-35: Plunge (left) and pitch (right) chimney region LCO transitions for Mach 0.96 through Mach 0.99 at low density (0.05 kg/m^3 or lower).*

Details of the LCO responses can be obtained from their corresponding phase plots. Figure 6.41 shows the entire lifespan phase plots for wing tip plunge versus velocity and pitch at Mach 0.96 just after the chimney boundary. The plots are rather muddled because of duration of the response contained within them, but they both contain some characteristic features of the chimney transition than can only be shown from start to finish. First, in displacement versus velocity, there is a criss-crossing striation pattern visible as the first-bending mode decays and the second-bending mode grows. Secondly, in the midchord displacement versus pitch plot, it is clearly visible that there is a change in the phase between the wing tip plunge and pitch from the initial condition to the steady state. The relative amplitudes are much smaller, but the result is clear. The cause of this phase reversal is the natural pitching cause by the different bending mode shapes. Plunge and pitch are out of phase at the wing tip for first-bending and in phase for second-bending, making this an excellent early indicator of chimney mode transition.

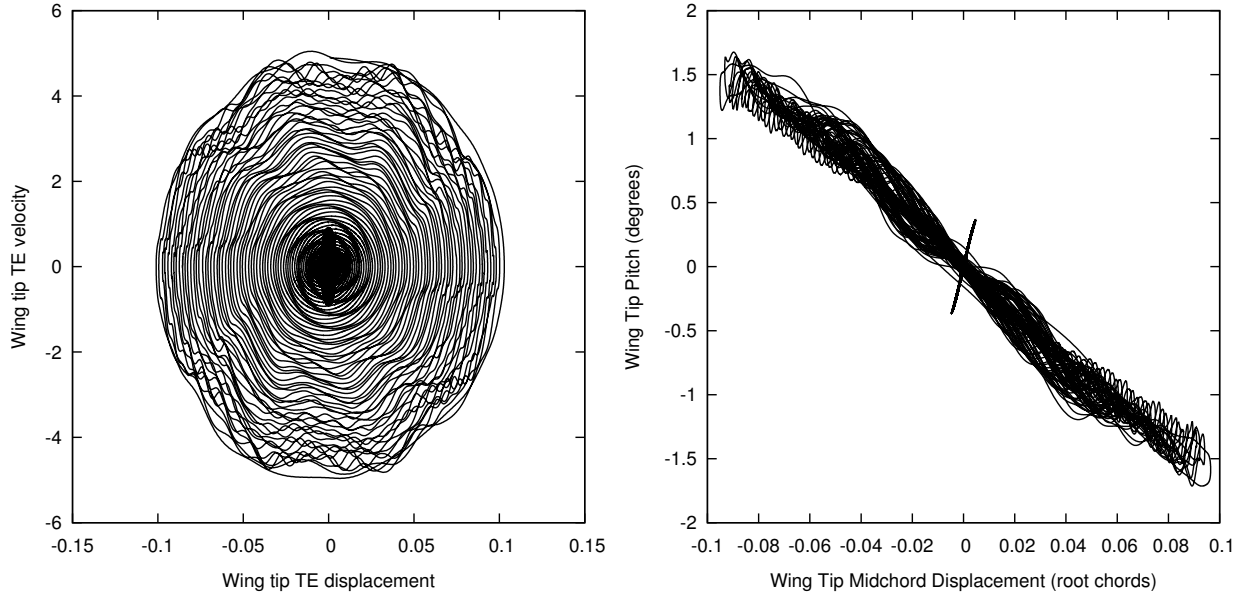


Figure 6.41: *FX-35: Lifetime phase plots for a first-bending to second-bending chimney transition (Mach 0.96, density 0.04 kg/m³).*

The general transient phase plot characteristics are shared by all the chimney transitions presented here, but only specific aspects are unique to the chimney region. Similar characteristics are observable at the Mach 0.95 condition, which does not also experience the resurgence of amplitude seen at the chimney test points. Figure 6.42 clearly shows the criss-crossing striations and the phase reversal associated with the second-bending mode (looking at a subset of oscillation cycles), but the final amplitudes are insignificantly small. It seems to be something in between noise and a clean second-bending response.

When looking in closer detail at the chimney test points, using a subset of oscillations from the steady state response, there is a clearly defined pattern of motion as shown in the phase and kinetic energy distribution plots in Figures 6.43 through 6.48. Notably, the cleanest second-bending response is directly after the chimney boundary, with some other

mode showing increased influence as Mach number increases. The kinetic energy distribution clearly shows a dip in second-bending with nothing else to take its place, but that is because only the first four modes are normally plotted. In Figure 6.48 the modes are increased to eight, and they can clearly be seen weakly participating. It is very rare for these modes to make any meaningful appearance; even second-torsion barely deserves to be on the list.

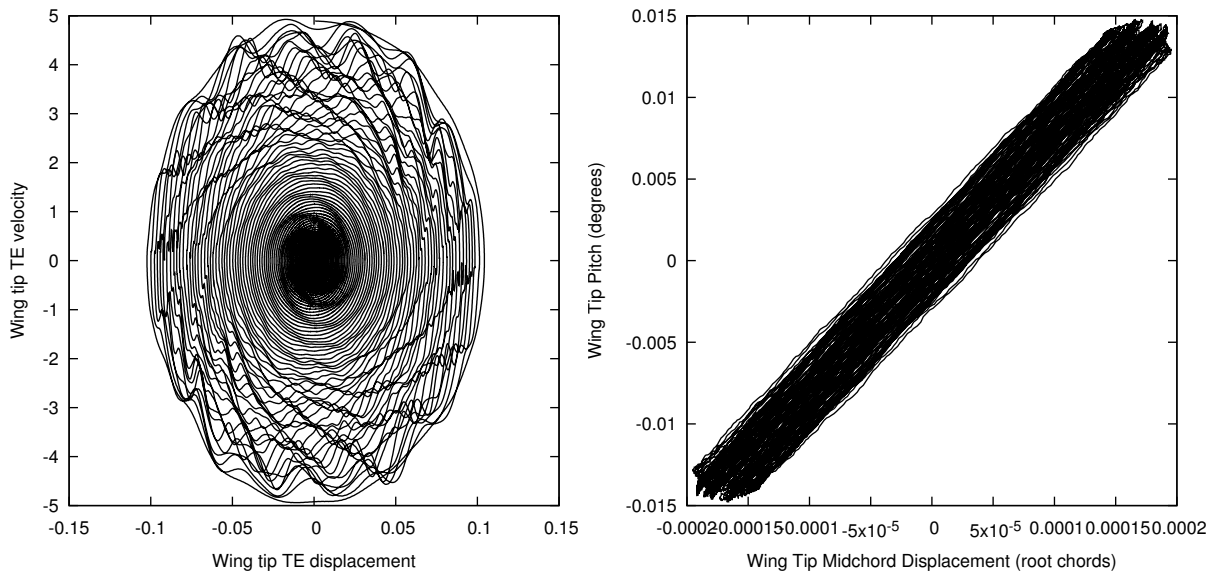


Figure 6.42: *FX-35: Lifetime (left) and steady state (right) phase plots showing similar chimney characteristics prior to the chimney region (Mach 0.95, density 0.03 kg/m³).*

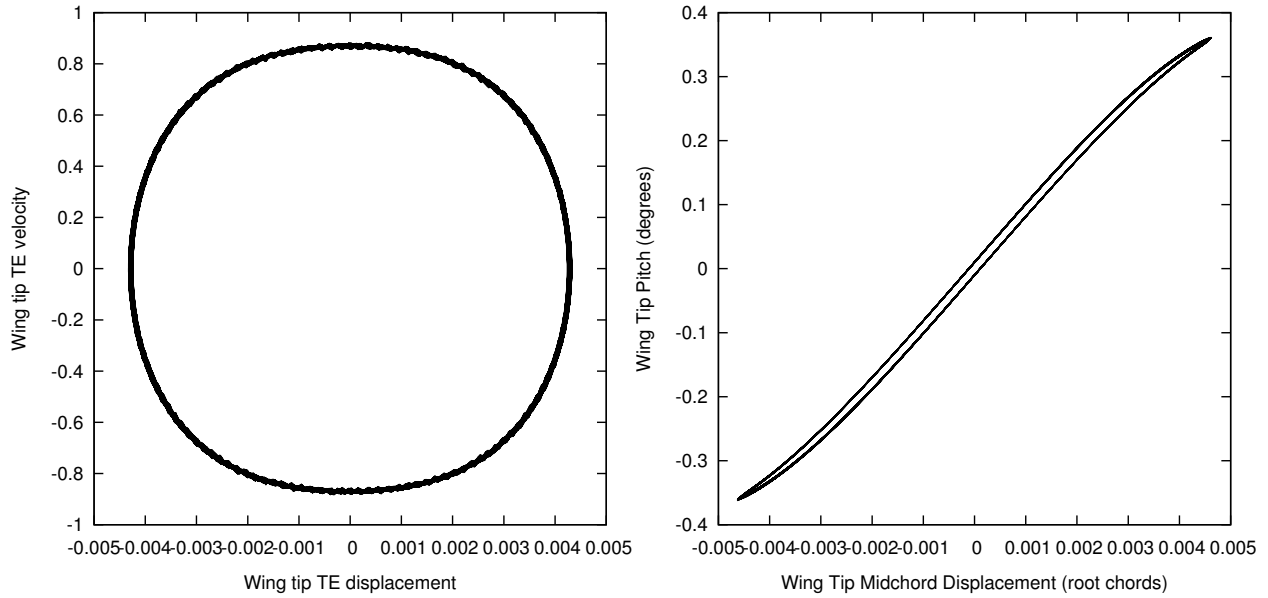


Figure 6.43: *FX-35: Steady state chimney response phase plots over a subset of oscillations showing a well defined pattern of second-bending motion (Mach 0.96, density 0.04 kg/m^3).*

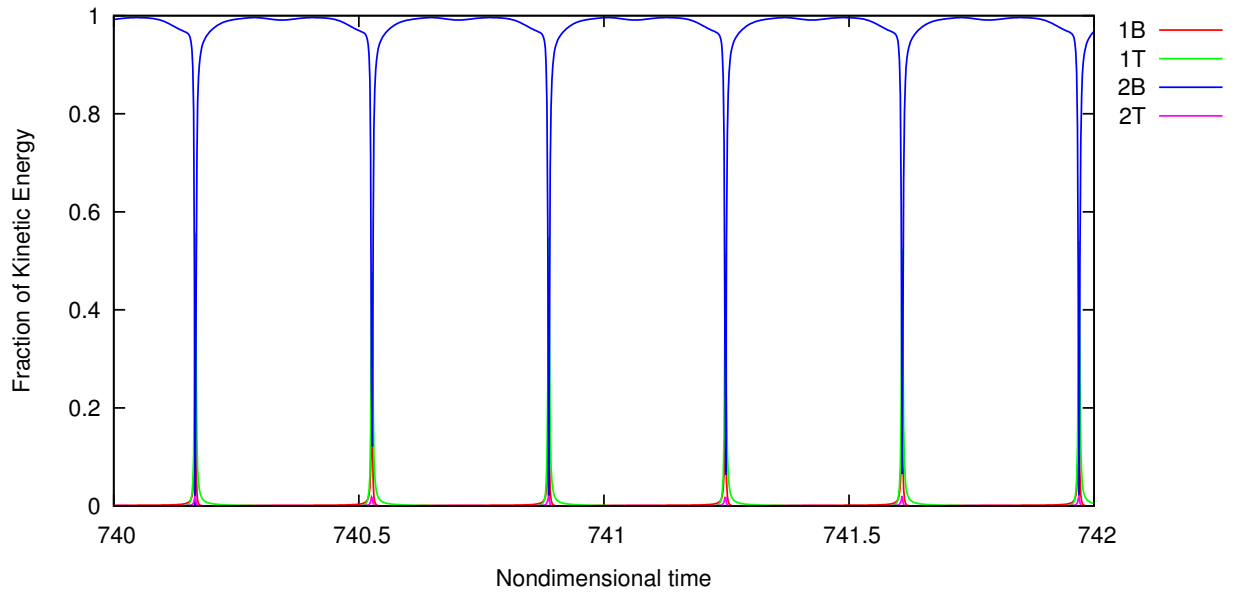


Figure 6.44: *FX-35: Distribution of kinetic energy by mode in the chimney, showing dominant second-bending motion (Mach 0.96, density 0.04 kg/m^3).*

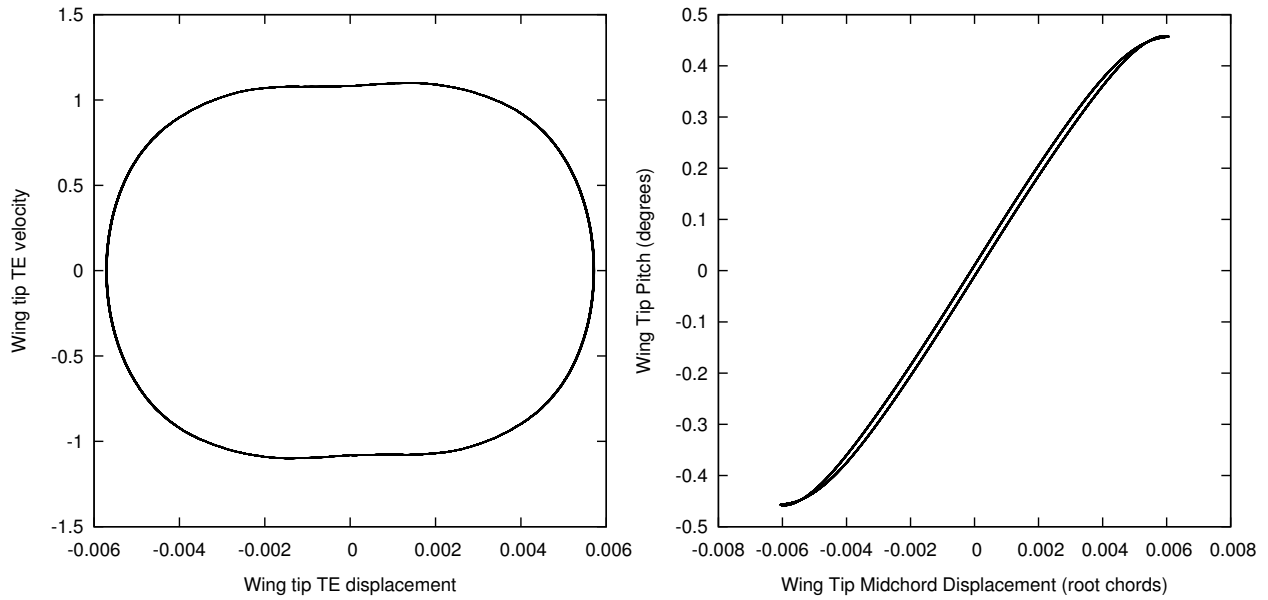


Figure 6.45: *FX-35: Steady state chimney response phase plots over a subset of oscillations showing the beginnings of multi-mode influence (Mach 0.97, density 0.04 kg/m^3).*

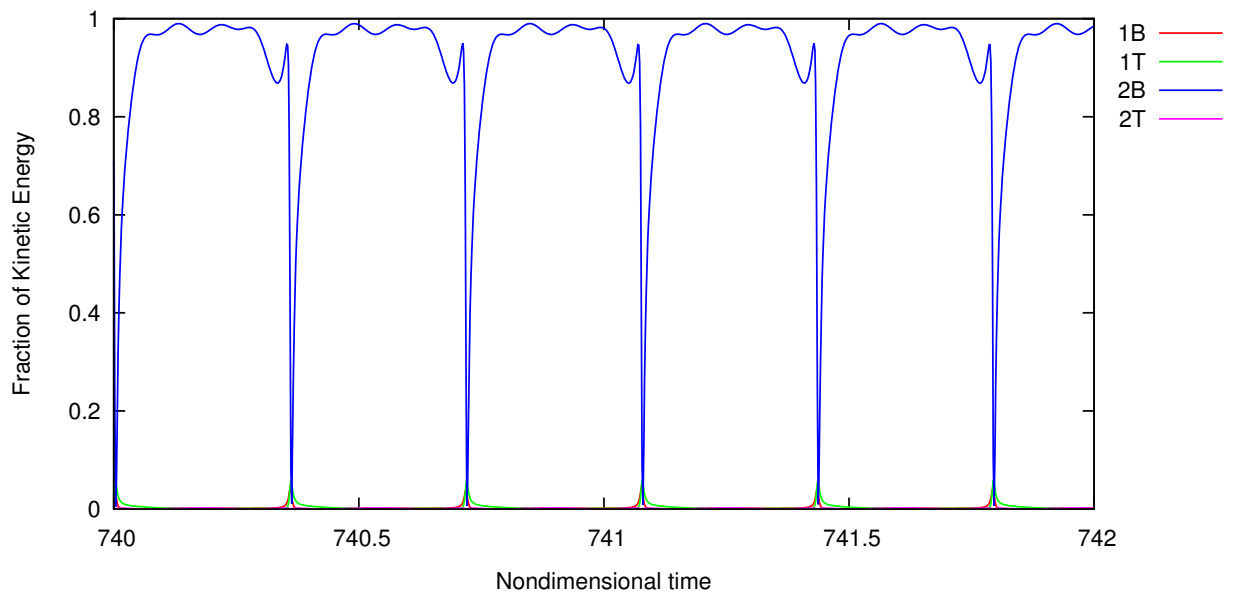


Figure 6.46: *FX-35: Distribution of kinetic energy by mode in the chimney, showing dominant second-bending motion (Mach 0.97, density 0.04 kg/m^3).*

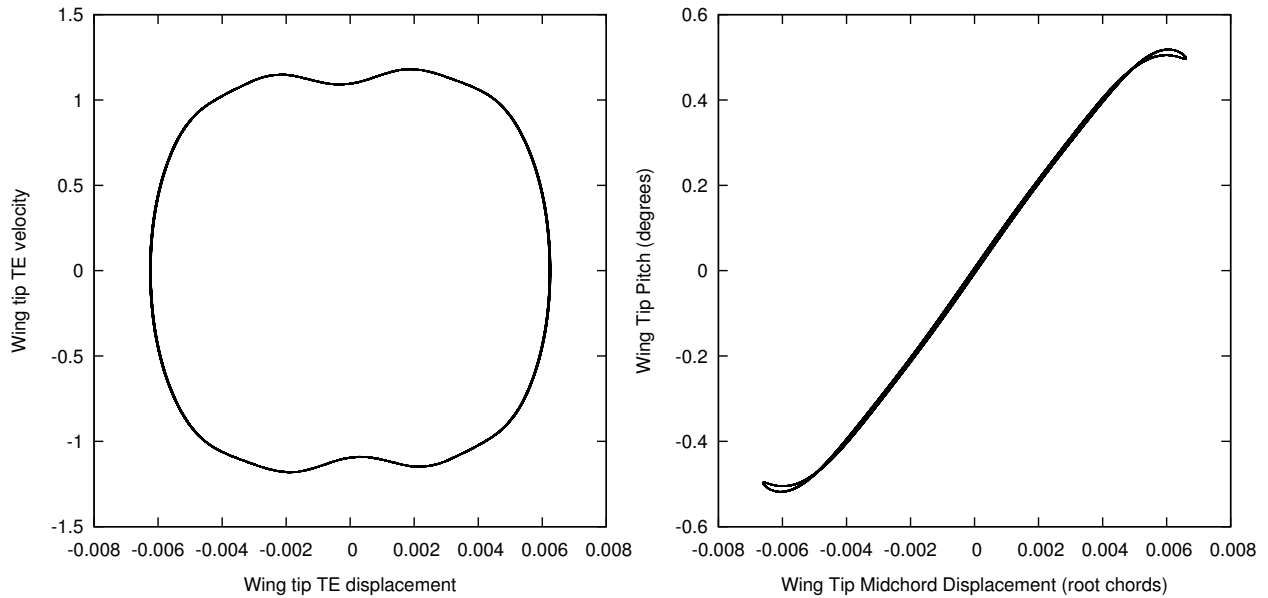


Figure 6.47: *FX-35: Steady state chimney response phase plots over a subset of oscillations showing the influence of other modes on the second-bending pattern (Mach 0.98, density 0.02 kg/m³).*

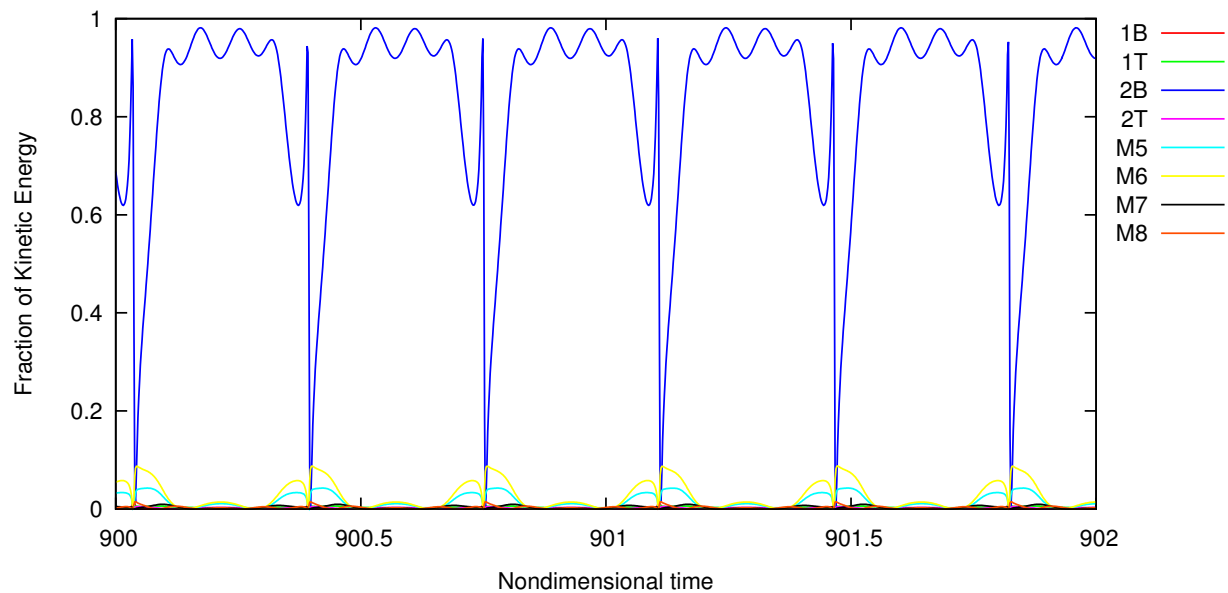


Figure 6.48: *FX-35: Distribution of kinetic energy by mode in the chimney, showing dominant second-bending motion and unexpected participation from additional modes beyond the first four (Mach 0.98, density 0.02 kg/m³).*

6.4.2 F-Wing: Chimney

Figures 6.49 through 6.52 show the long term wing tip responses on either side of the chimney boundary for the F-Wing. Before the boundary, at Mach 0.94, both plunge and pitch asymptotically approach zero. After the boundary, at Mach 0.95, the response eventually begins the transition to non-zero finite amplitudes for plunge and pitch. Figure 6.53 shows plunge and pitch chimney transitions for Mach 0.95 through Mach 0.98. Similar to the FX-35, higher Mach numbers result in faster transitions, however, the steady state response at all Mach numbers involves both second-bending and first-torsion, resulting in much higher pitching amplitudes relative to plunge.

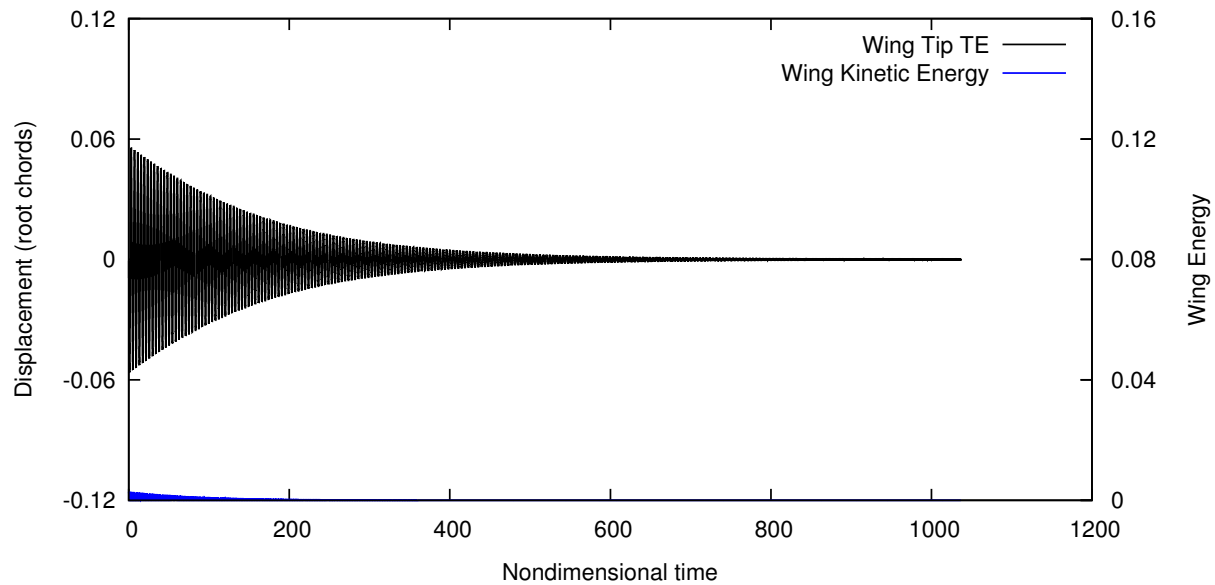


Figure 6.49: *F-Wing: Steady state plunge asymptotically approaching zero prior to the chimney boundary (Mach 0.94, density 0.05 kg/m³).*

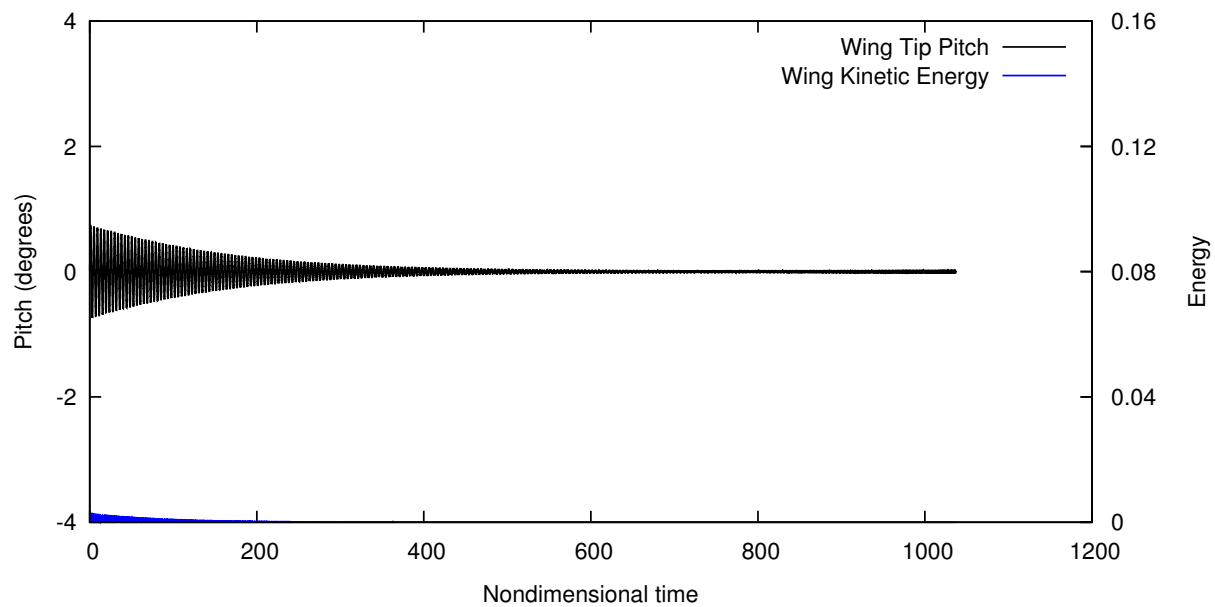


Figure 6.50: *F-Wing: Steady state pitch asymptotically approaching zero prior to the chimney boundary (Mach 0.94, density 0.05 kg/m³).*

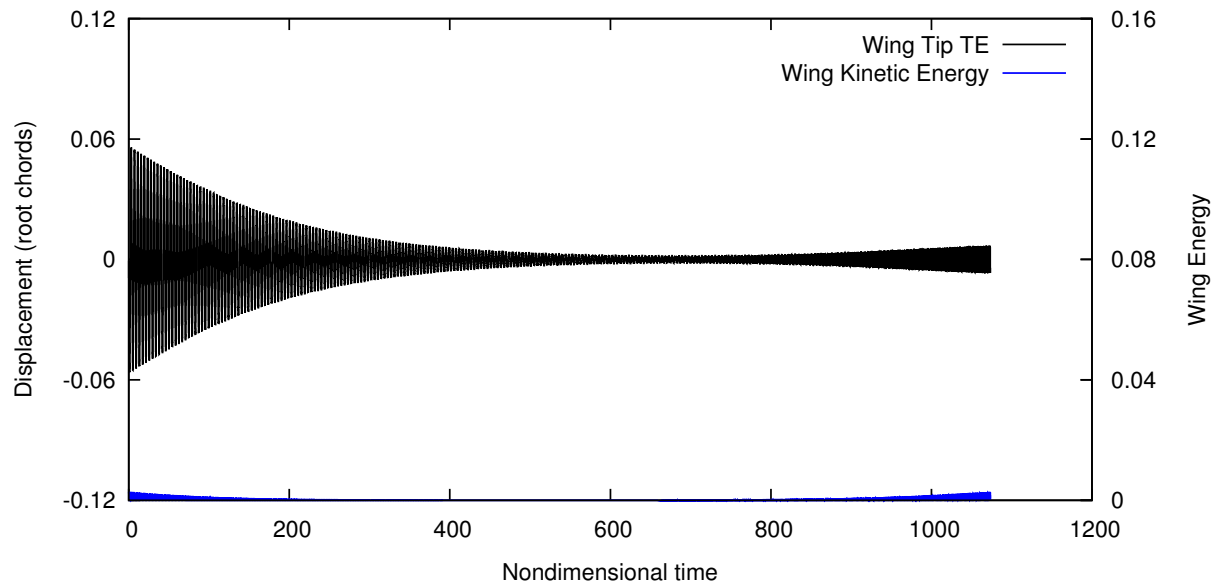


Figure 6.51: *F-Wing: Steady state plunge transitioning to a neutrally stable coupled first-torsion and second-bending response after the chimney boundary (Mach 0.94, density 0.05 kg/m³).*

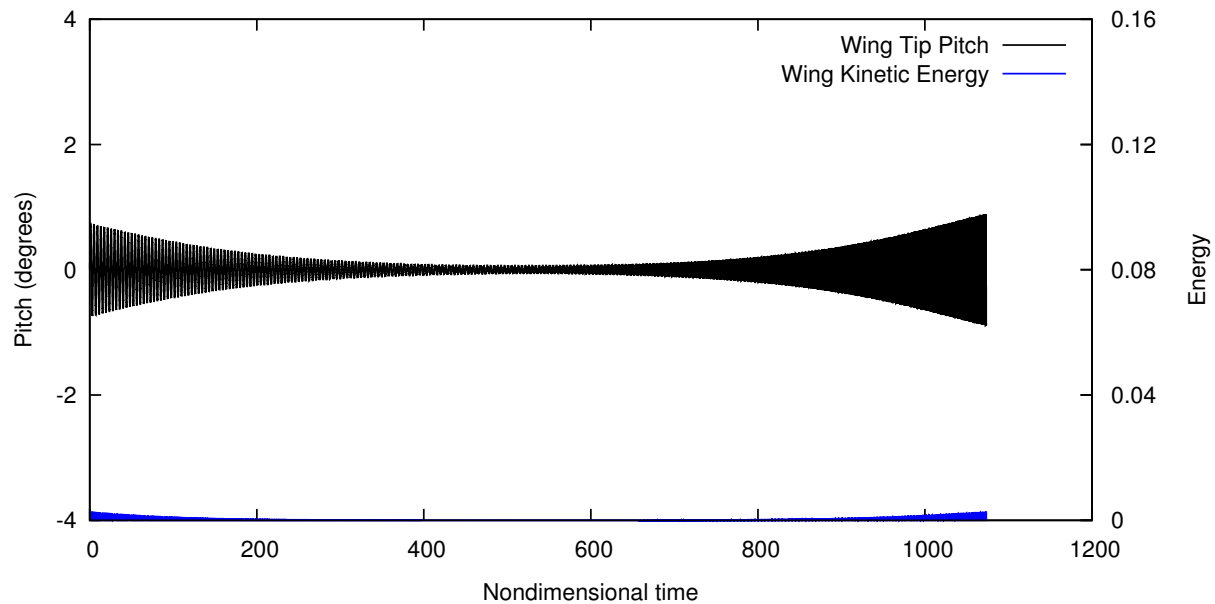


Figure 6.52: *F-Wing: Steady state pitch transitioning to a neutrally stable coupled first-torsion and second-bending response after the chimney boundary (Mach 0.94, density 0.05 kg/m³).*

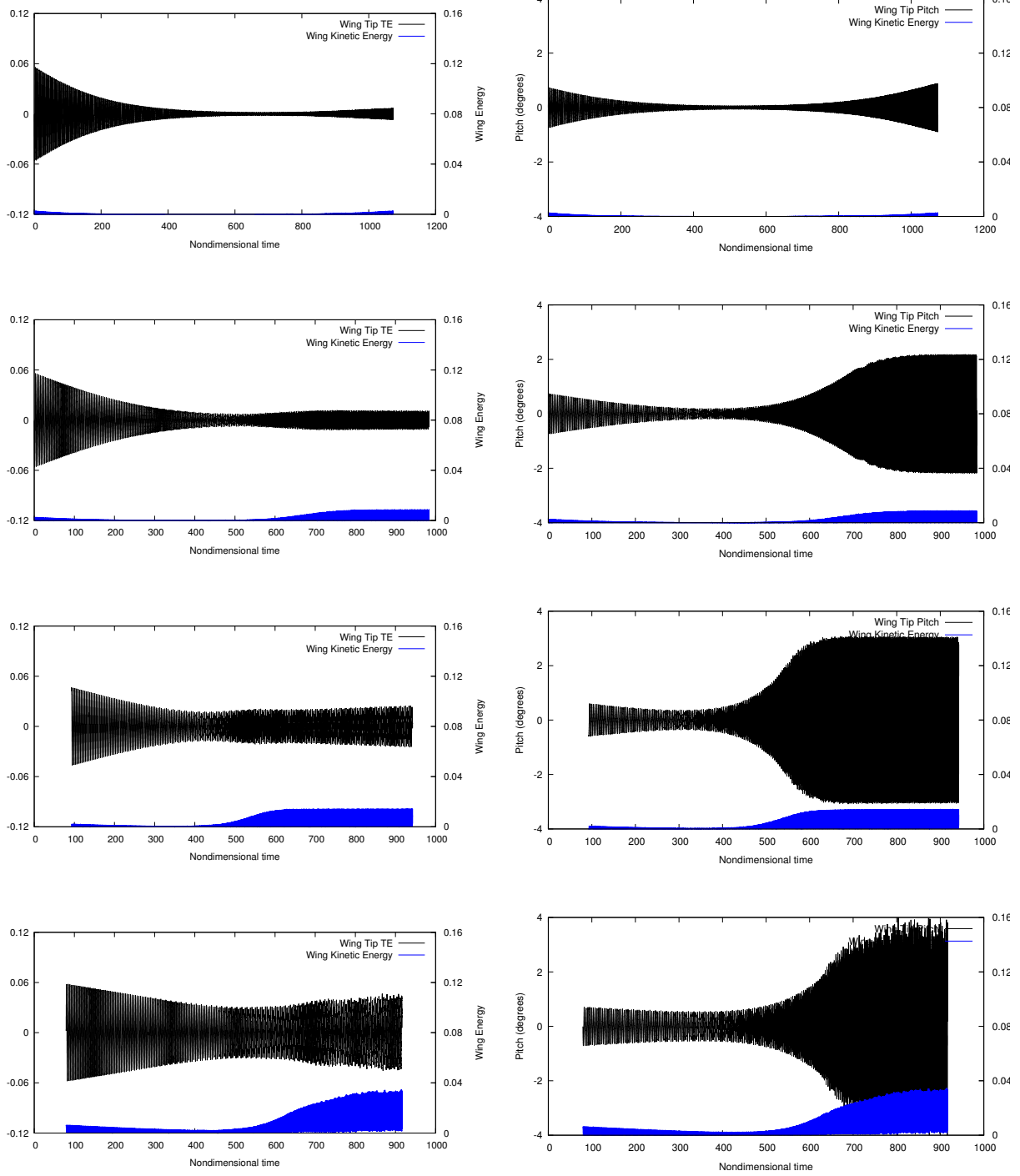


Figure 6.53: *F*-Wing: Plunge (left) and pitch (right) chimney transitions for Mach 0.95 through Mach 0.98.

As usual, the phase plots can be used to help categorize an additional level of detail to compare and contrast the various chimney responses. Figures 6.54 and 6.55 show the entire life-span phase plots for wing tip plunge versus velocity and pitch at Mach 0.94 and Mach 0.95 on either side of the chimney boundary. Because of the increased pitch amplitude inside the chimney for the F-Wing, the pitch-plunge phase reversal when transitioning from first-bending to second-bending creates a stark contrast between the Mach 0.94 and Mach 0.95 phase plots.

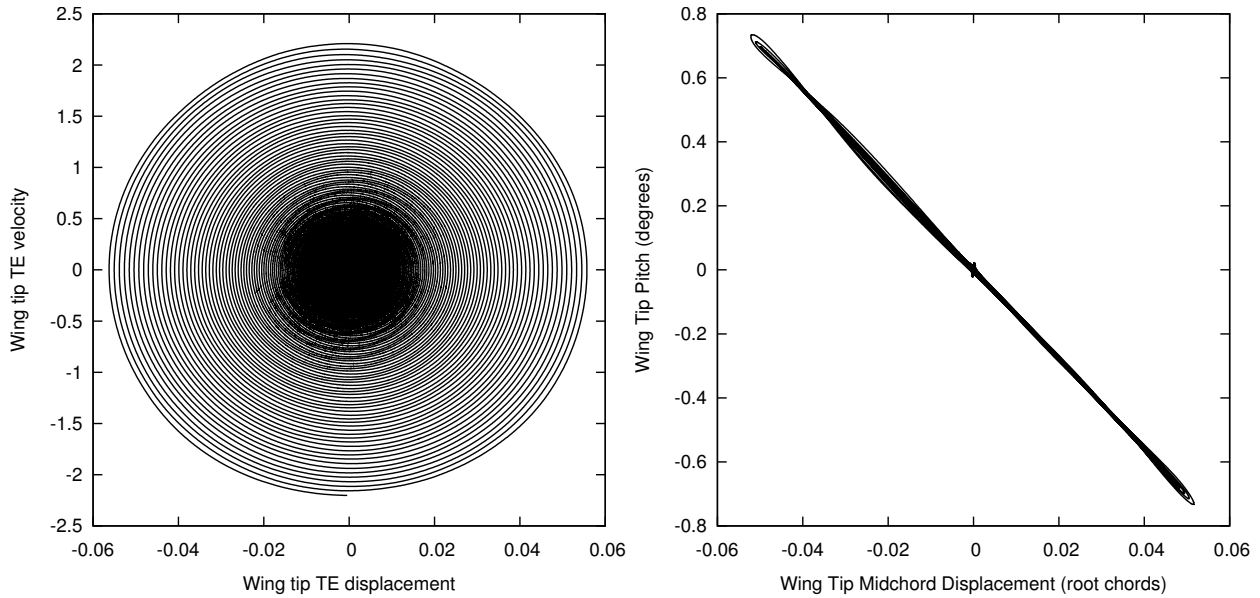


Figure 6.54: *F-Wing: Complete lifetime phase plots prior to the chimney transition (Mach 0.94, density 0.05 kg/m^3).*

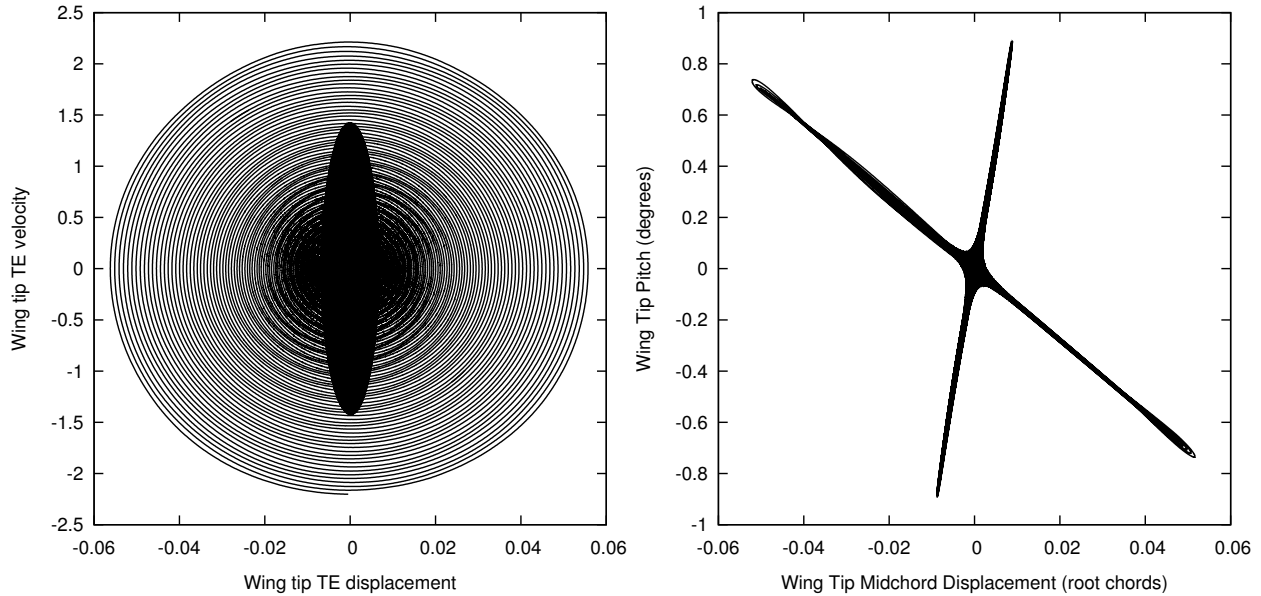


Figure 6.55: *F-Wing: Complete lifetime phase plots just after the chimney transition, showing the phase reversal between wing tip pitch and plunge associated with the switch from first-bending to second-bending (Mach 0.95, density 0.05 kg/m³).*

Comparing points from within the chimney, there is a startling difference between the specific patterns that emerge with increasing Mach number. Figures 6.56 through 6.63 show wing tip phase plots and kinetic energy distribution by mode for Mach 0.95 through Mach 0.98, focusing on smaller subsets of oscillations near the steady state response. Immediately after the chimney boundary, at Mach 0.95, the response is almost a pure second-bending mode. The phase pattern is a relatively smooth sinusoidal loop and the kinetic energy shows only the slightest involvement of first-torsion. At Mach 0.96, first-torsion establishes itself more firmly as a constant presence in the kinetic energy distribution. The pitch phase begins to wander back and forth, and the sinusoidal pattern becomes deformed. At Mach 0.97, first-bending occasionally joins in, and the phase plots show wild looping patterns that cover a broad area. Eventually, at Mach 0.98, the response becomes too chaotic for any patterns to

be discernible. The active modes shift around at sharp angles and the phase plots look like scribbles. There is still a defined area in which the scribbling happens, but the individual patterns of each cycle have been lost.

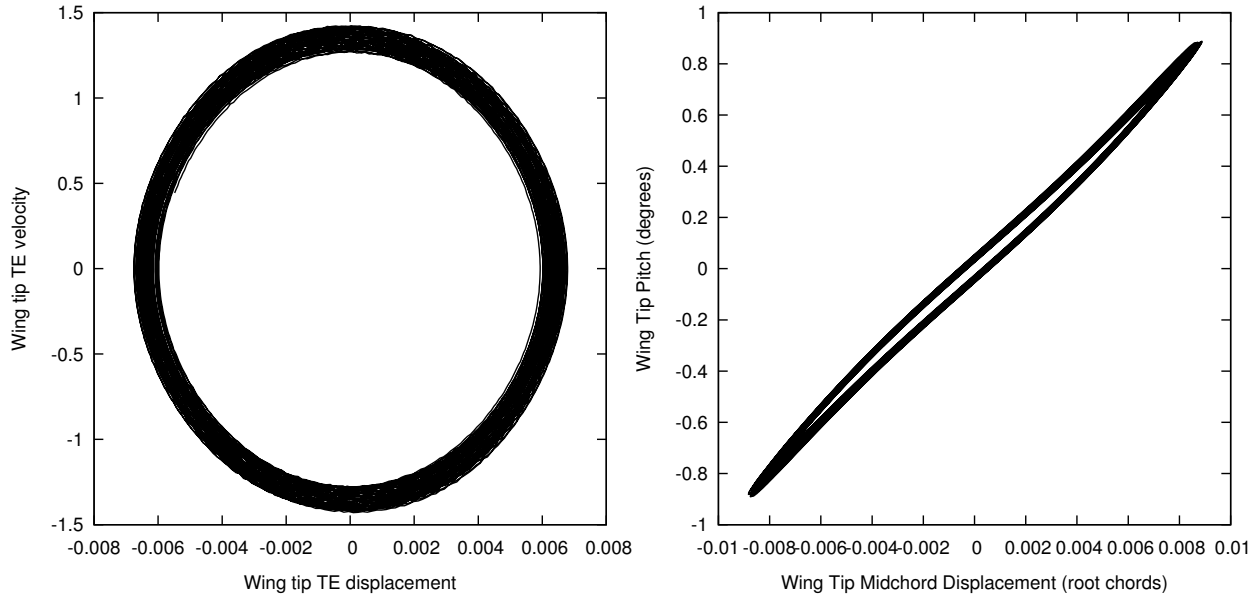


Figure 6.56: *F-Wing: Steady state chimney response phase plots over a subset of oscillations showing the well defined pattern of motion (Mach 0.95, density 0.05 kg/m³).*

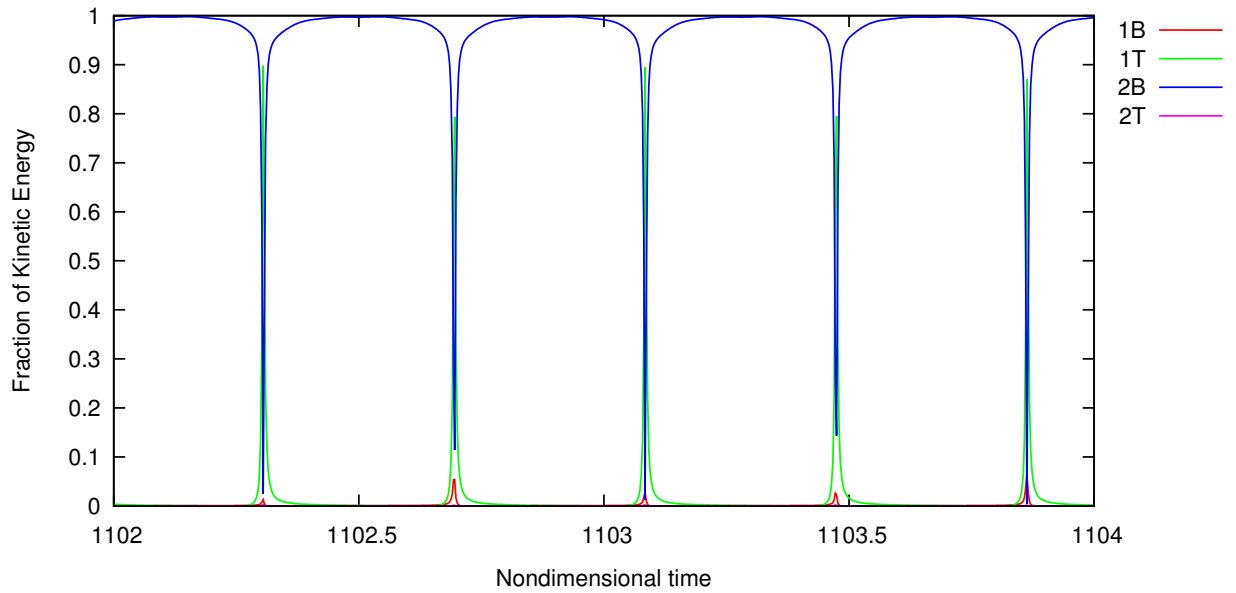


Figure 6.57: *F-Wing: Distribution of kinetic energy by mode in the chimney, showing dominant second-bending motion (Mach 0.95, density 0.05 kg/m³).*

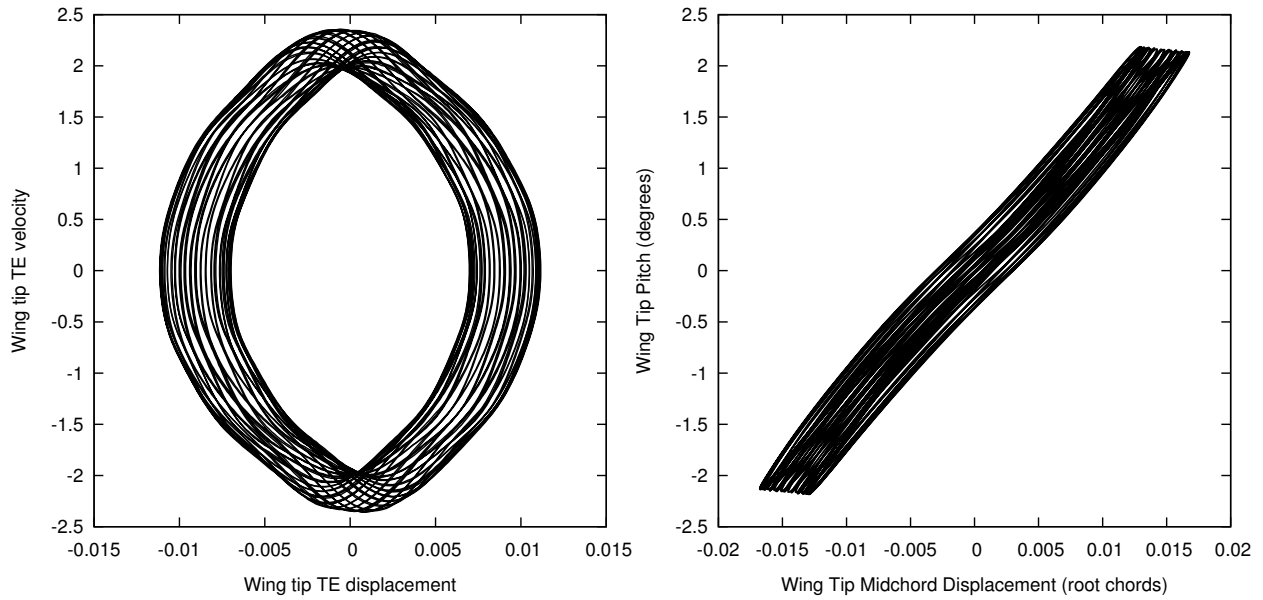


Figure 6.58: *F-Wing: Steady state chimney response phase plots for the F-Wing over a subset of oscillations showing a transition to wandering phase behavior (Mach 0.96, density 0.05 kg/m³).*

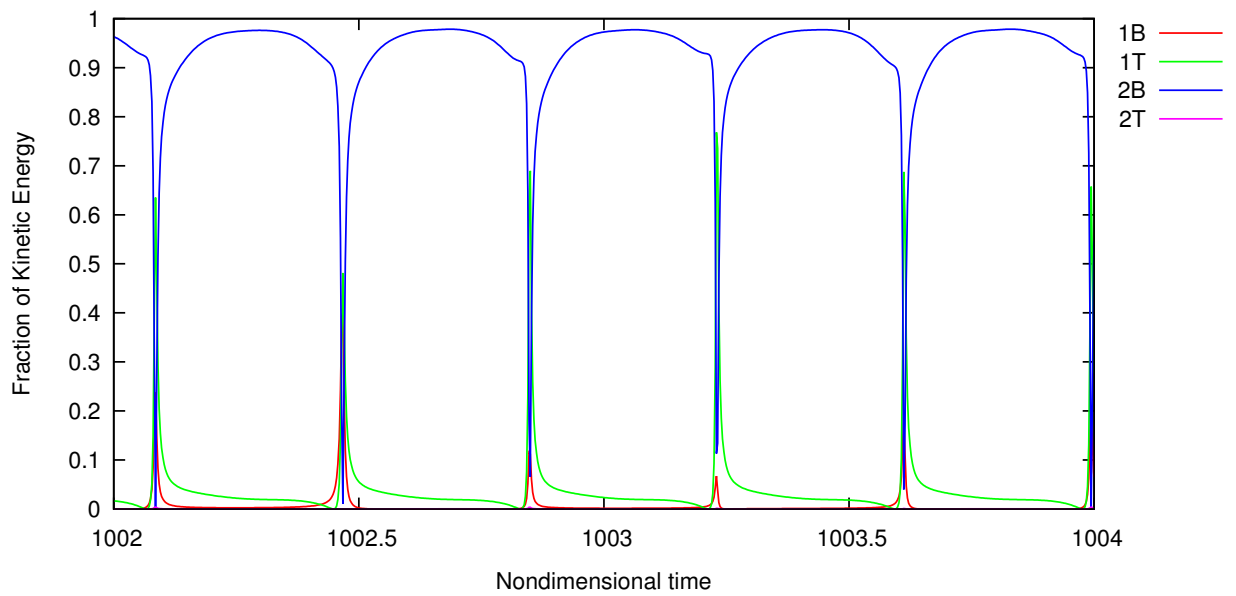


Figure 6.59: *F-Wing: Distribution of kinetic energy by mode in the chimney, showing an increase in first-torsion (Mach 0.96, density 0.05 kg/m³).*

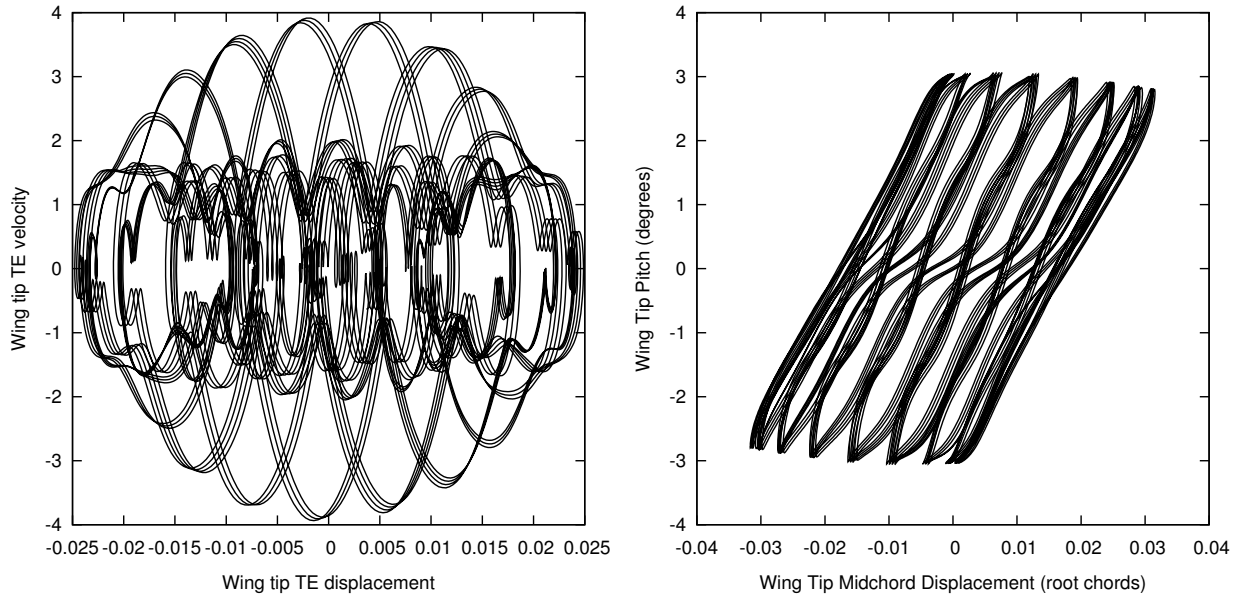


Figure 6.60: *F-Wing: Steady state chimney response phase plots for the F-Wing over a subset of oscillations showing a complex pattern that sweeps out a slightly different space with each cycle (Mach 0.97, density 0.04 kg/m³).*

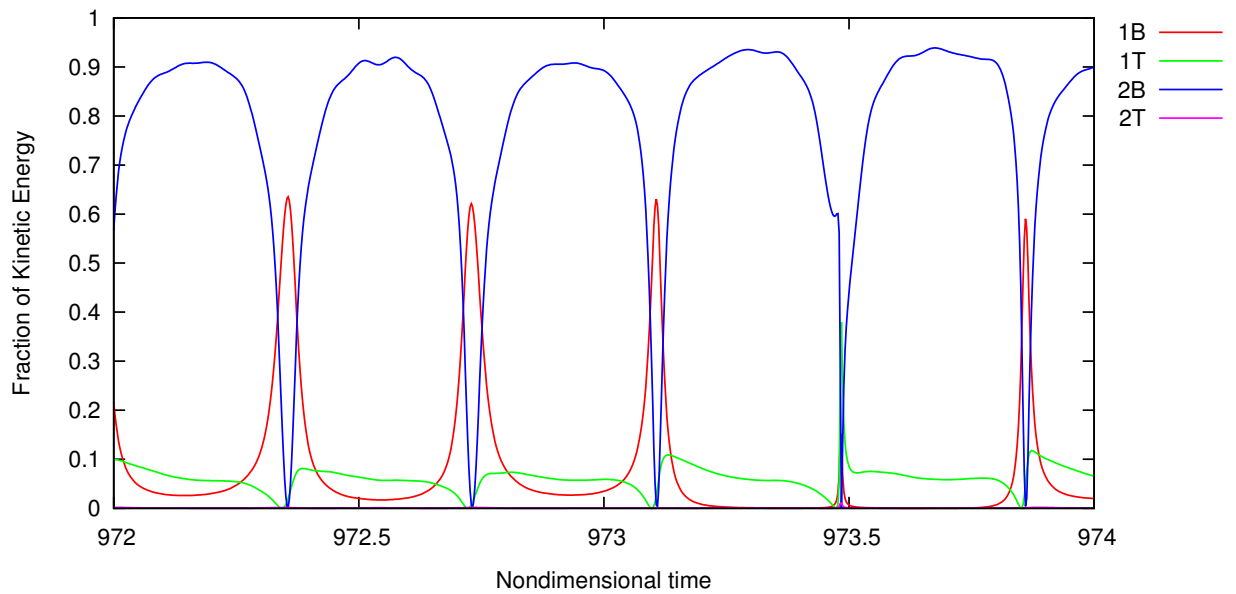


Figure 6.61: *F-Wing: Distribution of kinetic energy by mode in the chimney, showing the addition of first-bending for a three mode response (Mach 0.97, density 0.04 kg/m³).*

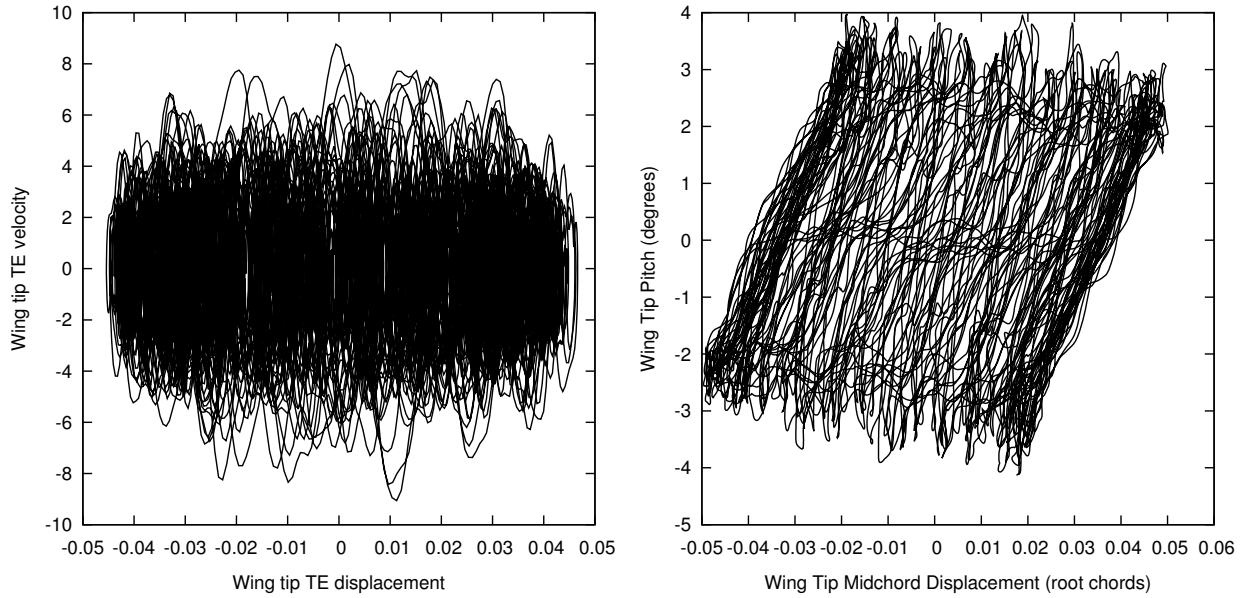


Figure 6.62: *F-Wing: Steady state chimney response phase plots for the F-Wing over a subset of oscillations revealing erratic behavior due the cacophony of mode interactions (Mach 0.98, density 0.02 kg/m^3).*

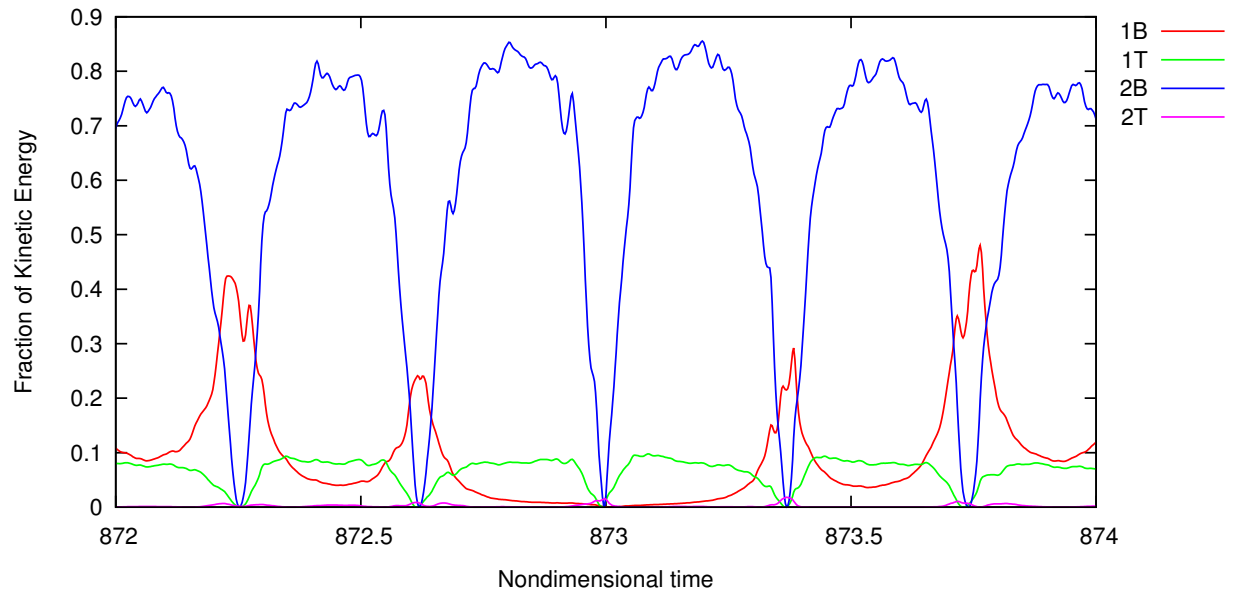


Figure 6.63: *F-Wing: Distribution of kinetic energy by mode in the chimney, showing how established patterns begin to break down on approach to Mach one (Mach 0.98, density 0.02 kg/m^3).*

6.5 Mach Number Freeze

The constant amplitude steady state responses seen at low densities at the beginning of the chimney region are a precursor to the Mach number freeze, a phenomenon that weakens flutter responses around and after Mach 1. Before the Mach number freeze, increasing density continues to produce strong flutter dominated by the first bending mode. However, at the same density just on the other side of the freeze boundary, the result is a neutrally stable or weakly unstable response. The test range for these behaviors is shown in Figure 6.64.

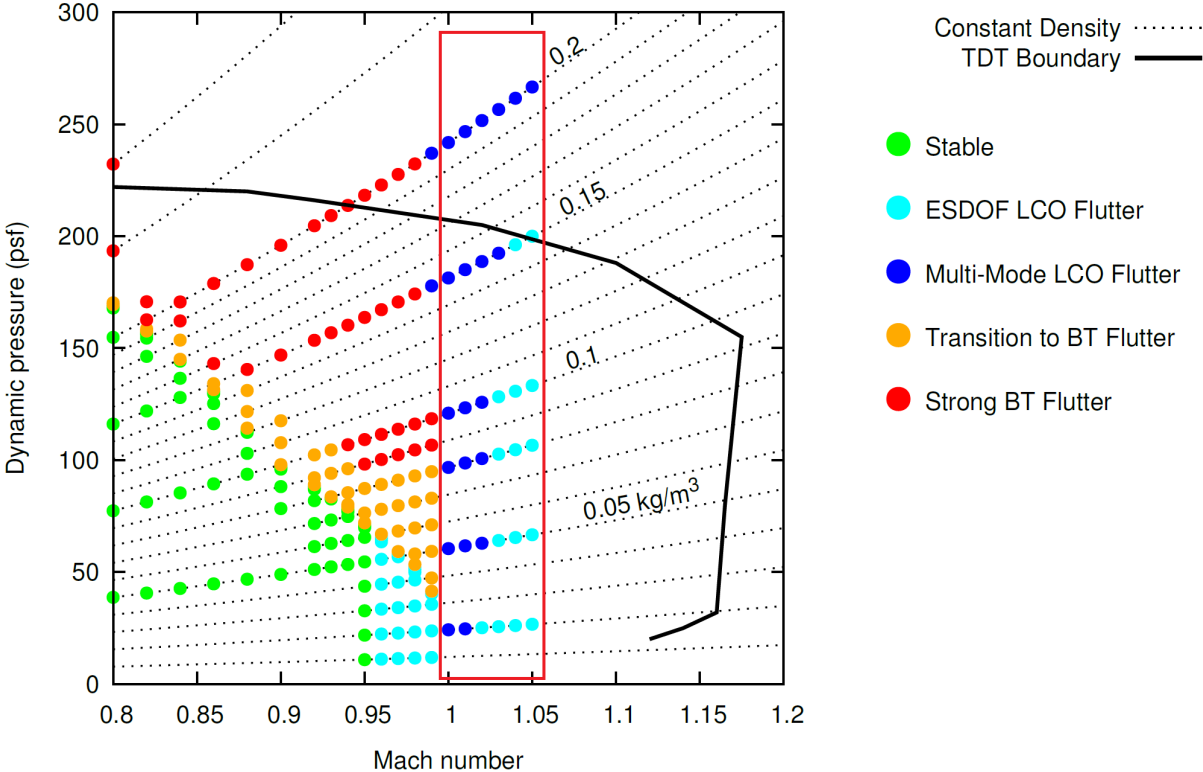


Figure 6.64: Indication of the Mach Freeze region free stream Mach number range.

6.5.1 FX-35: Mach Freeze

Figure 6.65 shows a series of plunge and pitch responses for increasing Mach number at a density of 0.2 kg/m^3 . Normally, this is a strong flutter condition as seen in the first row at Mach 0.97. Starting at Mach 0.98, the strength of the response shows signs of being muted, and by Mach 0.99 appears to be a neutrally stable condition. At Mach 1.00, shown in the last row, the result is a low energy, multi-mode response; a stark contrast to the explosive, bending-torsion flutter from just before the freeze.

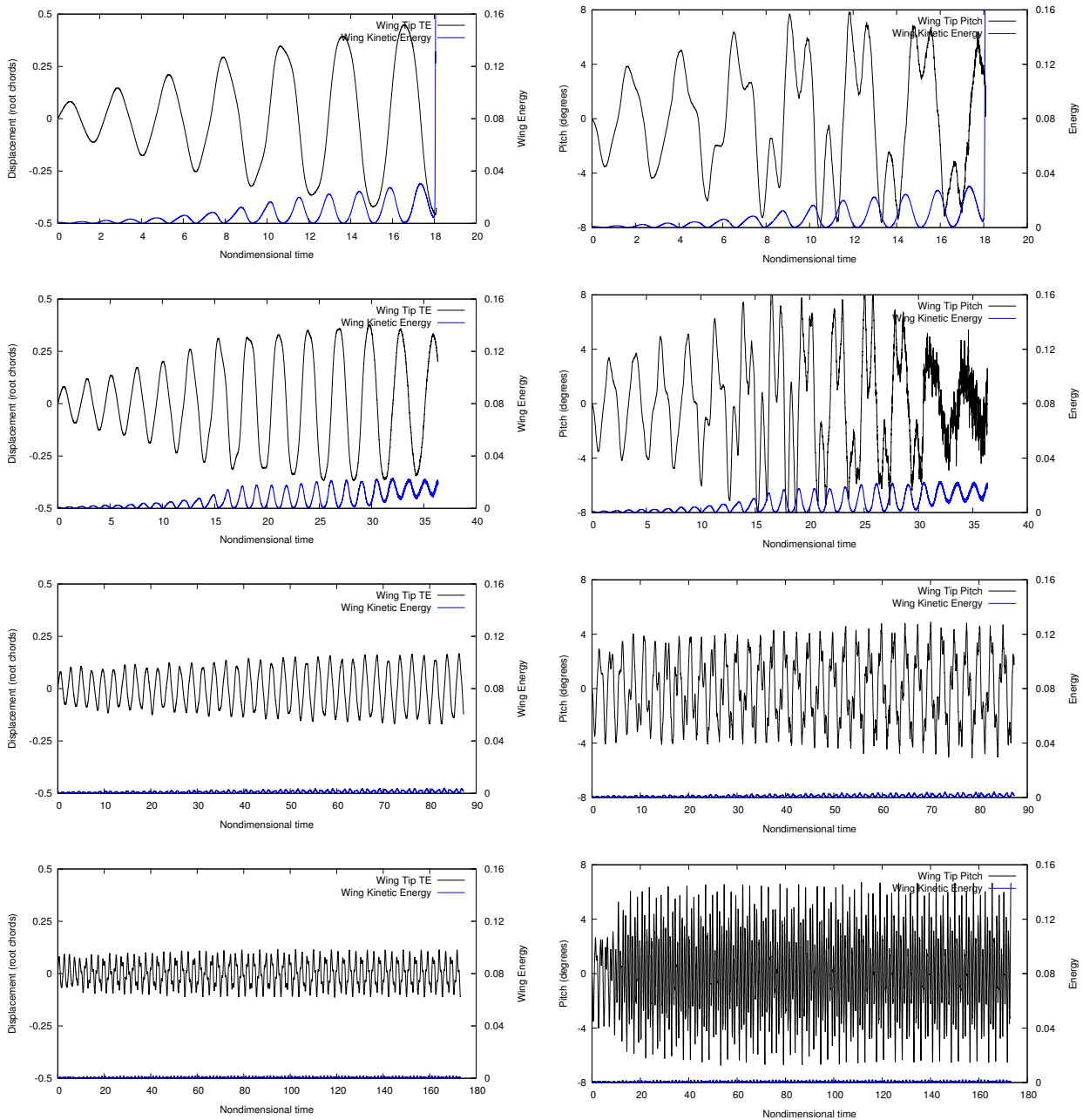


Figure 6.65: *FX-35: Plunge (left) and pitch (right) responses for Mach 0.97 through Mach 1.00 (density 0.2 kg/m^3) showing the quenching effect of the Mach number freeze starting around Mach 0.99.*

An interesting characteristic of the responses in the freeze region is that, instead of exhibiting patterns of stable or unstable behavior, they follow patterns of mode participation. All of the responses maintain the wing kinetic energy supplied by the initial condition, but each morphs over time into a different solution; redistributing that energy between various natural modes.

Figures 6.66 and 6.75 show an enlarged view of the Mach 1.00 plunge and pitch plots from the series above. The semblance of a pattern can be seen in both plots, but at the same time they appear volatile. The phase plots over a handful of cycles, seen in Figure 6.68, show a very complicated but somewhat reliable pattern being carved out repeatedly. The variety of modes participating to create this behavior is shown in Figure 6.69. Neutrally stable responses with clean phase patterns are usually dominated by either the first- or second-bending modes. In this case, the first-bending, first-torsion, and second-bending modes are all present and fluctuate in strength over time.

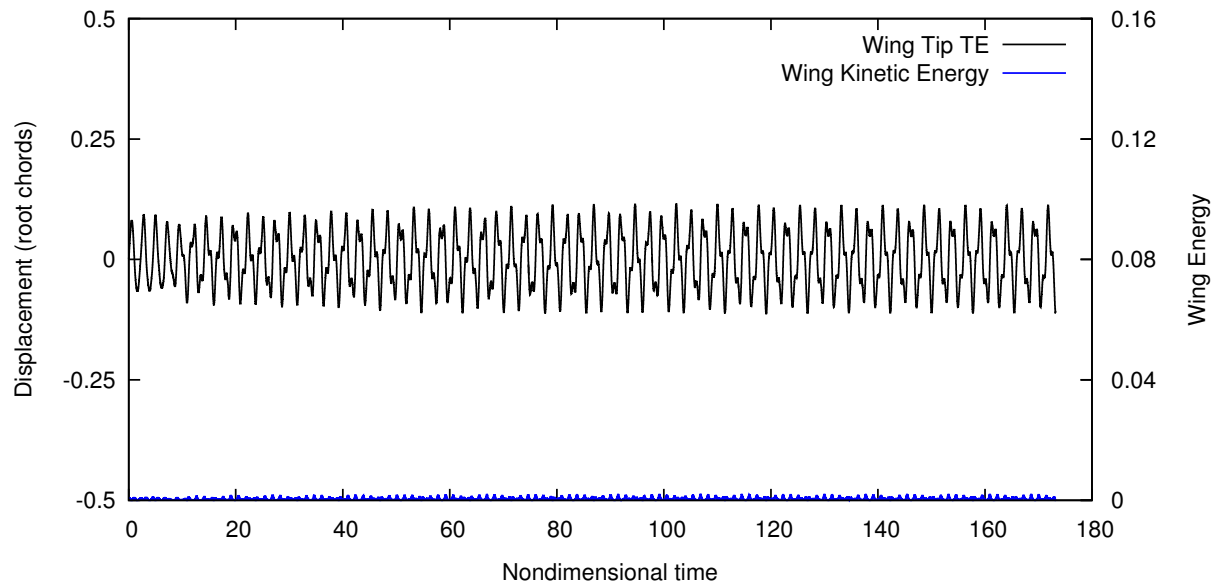


Figure 6.66: *FX-35: Neutrally stable plunge response just after the Mach freeze (Mach 1.00, density 0.2 kg/m^3).*

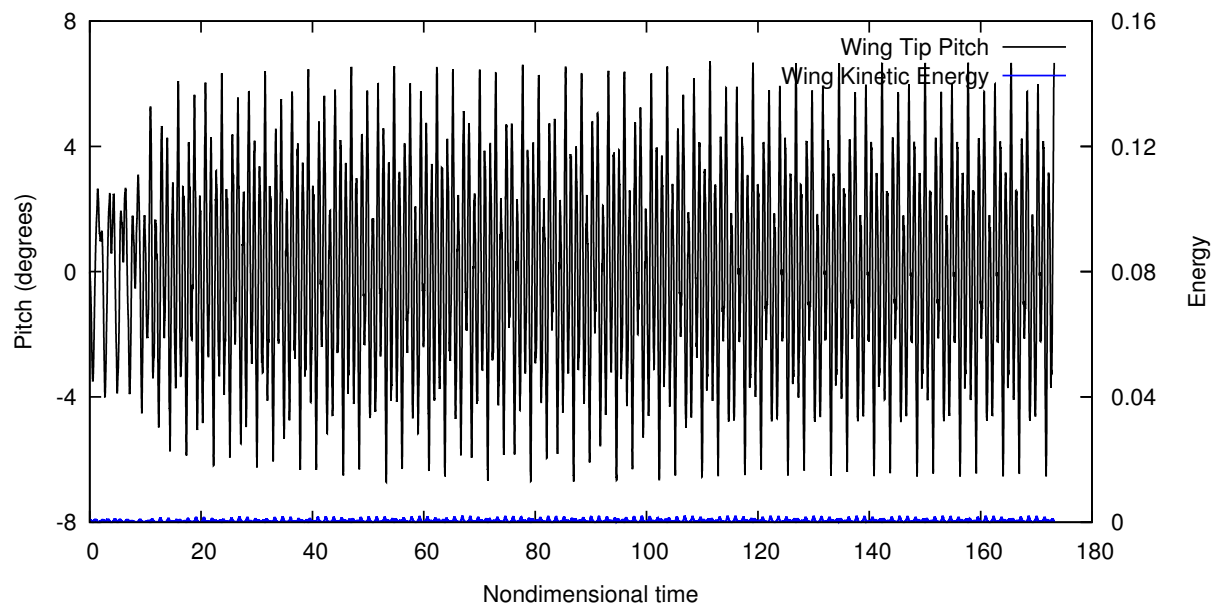


Figure 6.67: *FX-35: Neutrally stable pitch response just after the Mach freeze (Mach 1.00, density 0.2 kg/m^3).*

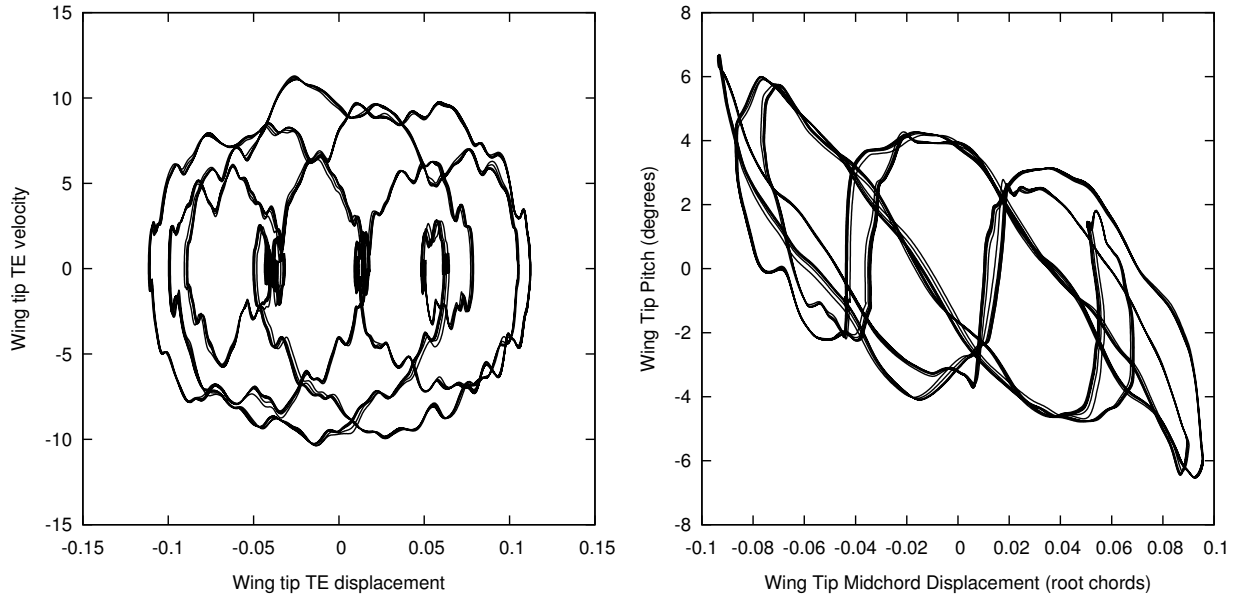


Figure 6.68: *FX-35*: Mach freeze phase plots showing the complex patterns resulting from a multi-mode response (Mach 1.00, density 0.2 kg/m^3).

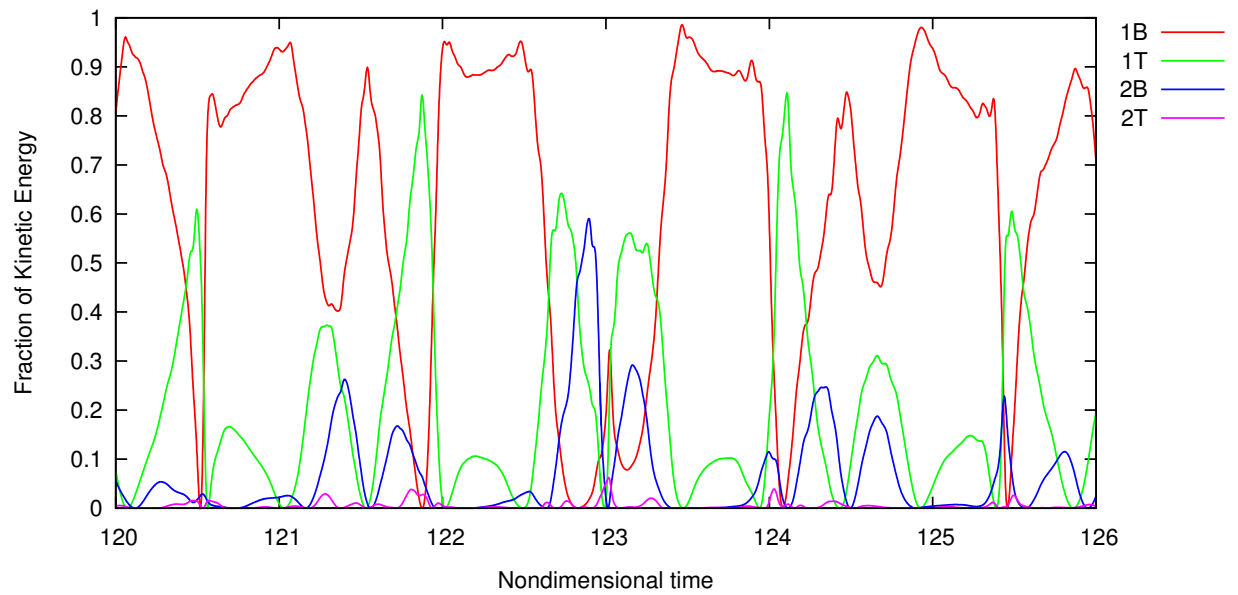


Figure 6.69: *FX-35*: Distribution of kinetic energy across natural modes, highlighting the interplay of modes responsible for complex responses seen after the Mach freeze (Mach 1.00, density 0.2 kg/m^3).

Cutting the density to 0.1 kg/m^3 , Figures 6.70 and 6.71 show a slightly more subdued response in the plunge and pitch. The transition from the initial condition appears to be occurring more slowly, and the form of the final solution is less apparent than it was at 0.2 kg/m^3 . The kinetic energy, however, shows that the response is not growing or decaying, only changing. Even though the wing tip motion looks more controlled in this case, the phase plots for this test point, seen in Figure 6.72, don't show any discernible pattern. Looking at the modal participation, Figure 6.73 shows a back and forth between the first-bending and second-bending. It is somewhat unintuitive that what appears to be a simpler interaction between fewer modes results in the loss of a clean pattern.

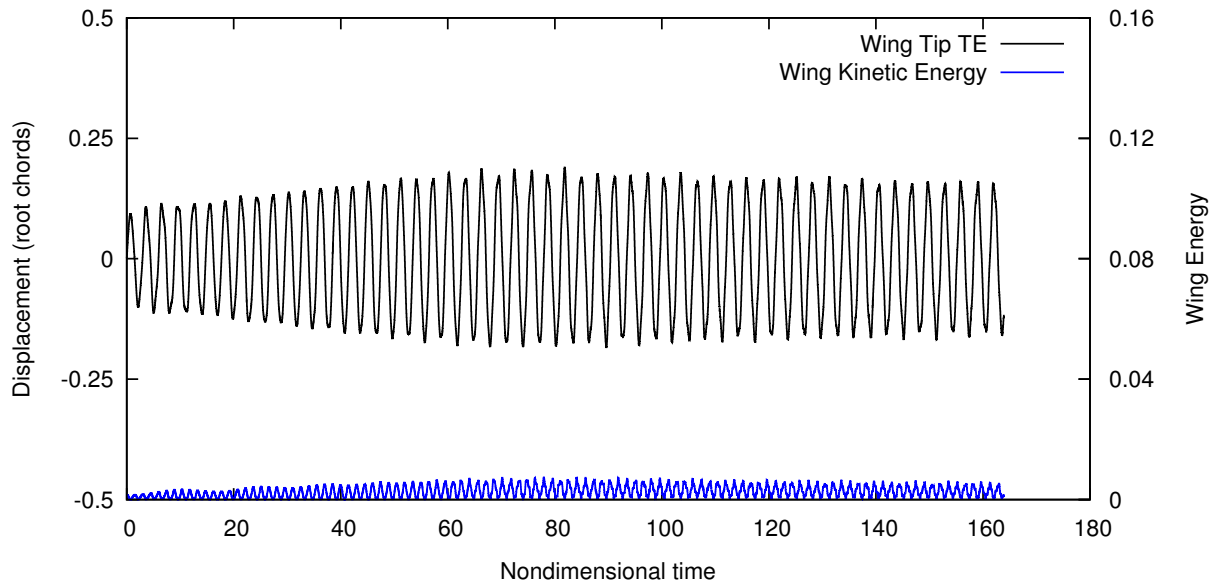


Figure 6.70: *FX-35: A more subdued neutrally stable plunge response just after the Mach freeze (Mach 1.00, density 0.1 kg/m^3).*

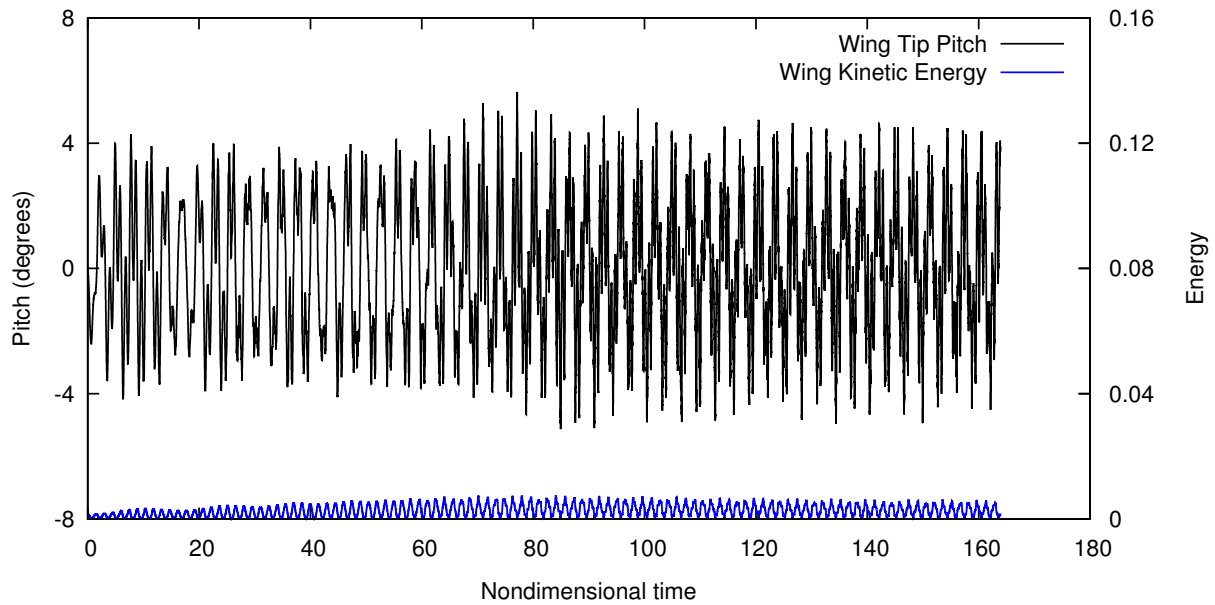


Figure 6.71: *FX-35: A more subdued neutrally stable pitch response just after the Mach freeze (Mach 1.00, density 0.1 kg/m³).*

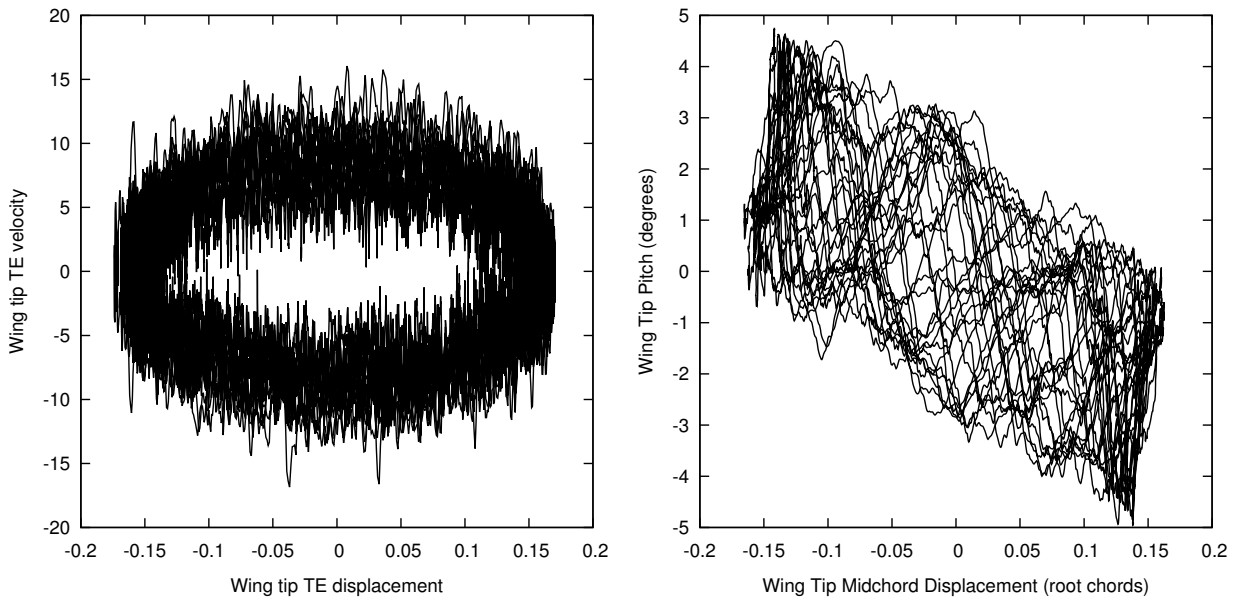


Figure 6.72: *FX-35: Mach freeze phase plots showing the smearing effect of the first-bending and second-bending mode interaction (Mach 1.00, density 0.1 kg/m³).*

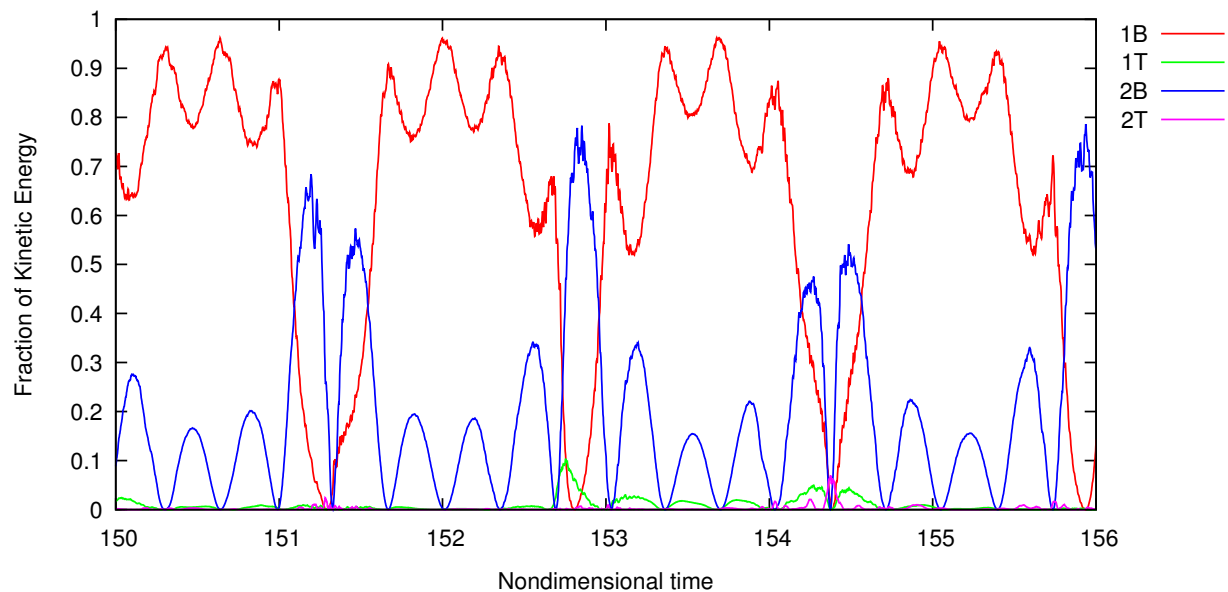


Figure 6.73: *FX-35* distribution of kinetic energy across natural modes, revealing a tug of war between first-bending and second-bending (Mach 1.00, density 0.1 kg/m^3).

Reducing the density again to 0.05 kg/m^3 , Figures 6.74 and 6.75 show a similar transition to what was seen at 0.1 kg/m^3 , only occurring at a slower rate. The phase and mode plots, Figures 6.76 and 6.77 seem to confirm this observation. The overall pattern, moving from high to low density, is similar in all of the test points from Mach 1.00 to Mach 1.05. The second-bending mode has a constant presence and will compete with first-bending to create chaotic behavior; only seeming to yield a specific pattern if first-torsion is involved.

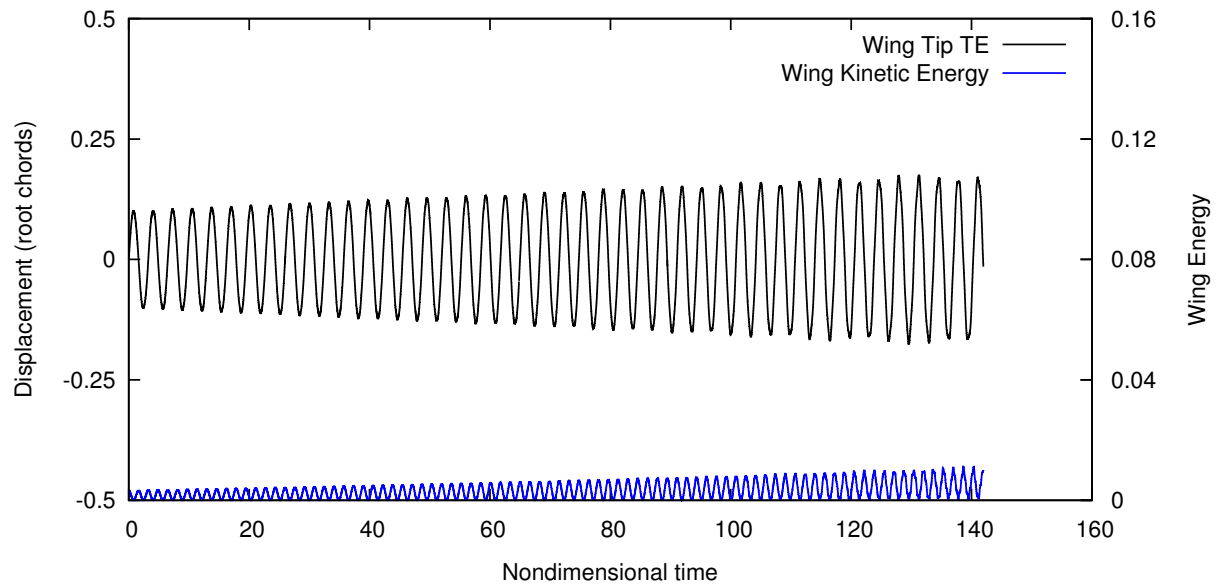


Figure 6.74: *FX-35: Neutrally stable plunge response just after the Mach freeze, which is slowed down by the decreased density (Mach 1.00, density 0.05 kg/m³).*

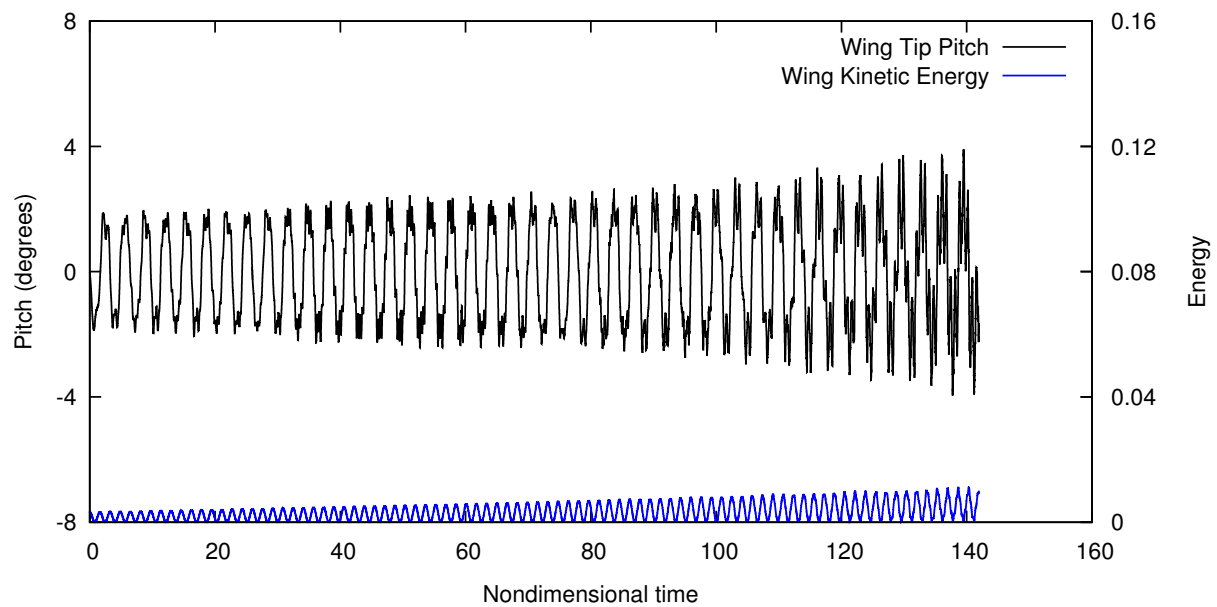


Figure 6.75: *FX-35: Neutrally stable pitch response just after the Mach freeze, which is slowed down by the decreased density (Mach 1.00, density 0.05 kg/m³).*

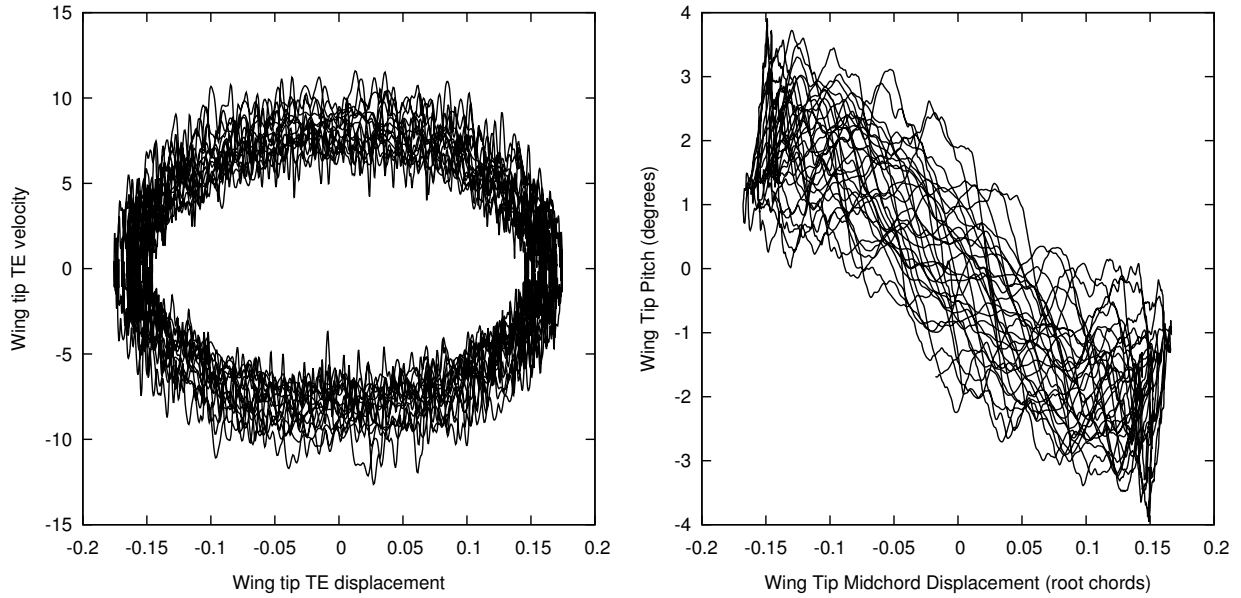


Figure 6.76: *FX-35: Mach freeze phase plots showing the smearing effect of the first-bending and second-bending mode interaction (Mach 1.00, density 0.05 kg/m³).*

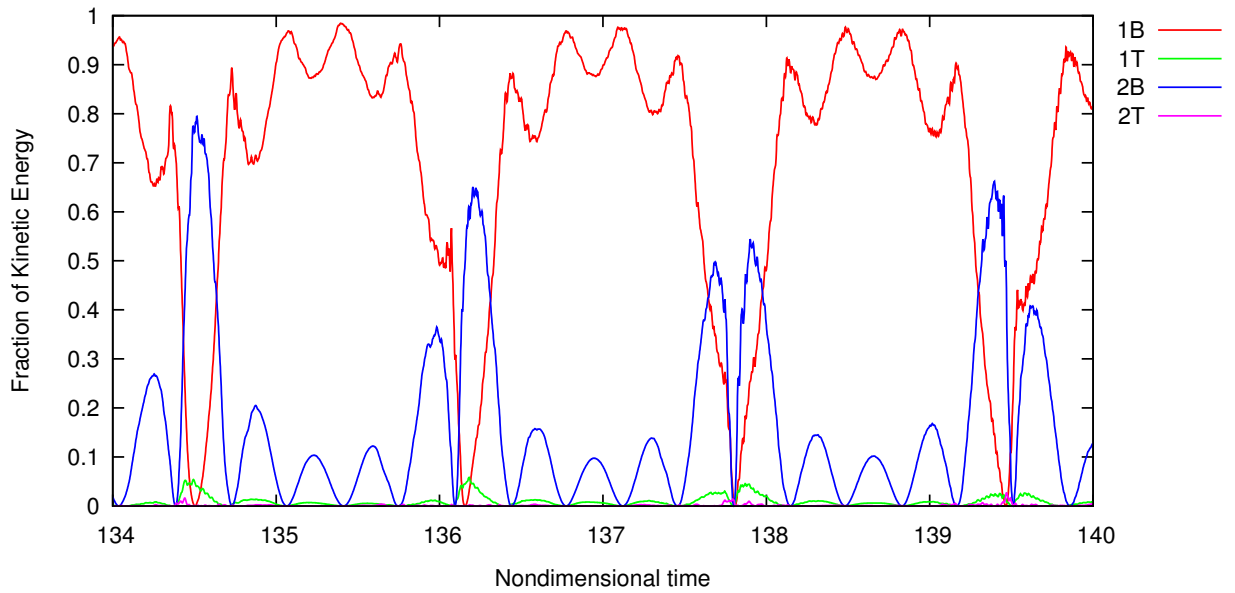


Figure 6.77: *FX-35: Distribution of kinetic energy across natural modes; neither of the modes present appear to be taking control of the response (Mach 1.00, density 0.05 kg/m³).*

The supersonic Mach freeze region has another observable pattern with respect to changing Mach number. The participation of the second-bending mode peaks at Mach 1.01, then falls off as Mach number increases. This appears to have a stabilizing effect on mode coupling, allowing the first-bending mode to exist essentially by itself. Figures 6.78 through 6.85 show how the highly complex multi-mode response from Mach 1.00 density 0.2 kg/m^3 loses its second-bending participation as Mach number increases. The patterns evident in the phase plots lose their intricacy as the coupling effects diminish, leaving responses similar to those seen in the subsonic region below Mach 0.96 where the first-bending mode dominates.

The most telling evidence for this transition is in the plunge versus pitch phase plot, which has a full 90 degree rotation when comparing a pure first-bending response to a pure second-bending response. When both modes are present, the effect is to make the pattern wider as the modes compete to drag the plot towards opposite corners. Especially at lower densities, the behavior gets closer and closer to an essentially single degree of freedom first-bending response, as shown in Figures 6.86 through 6.89.

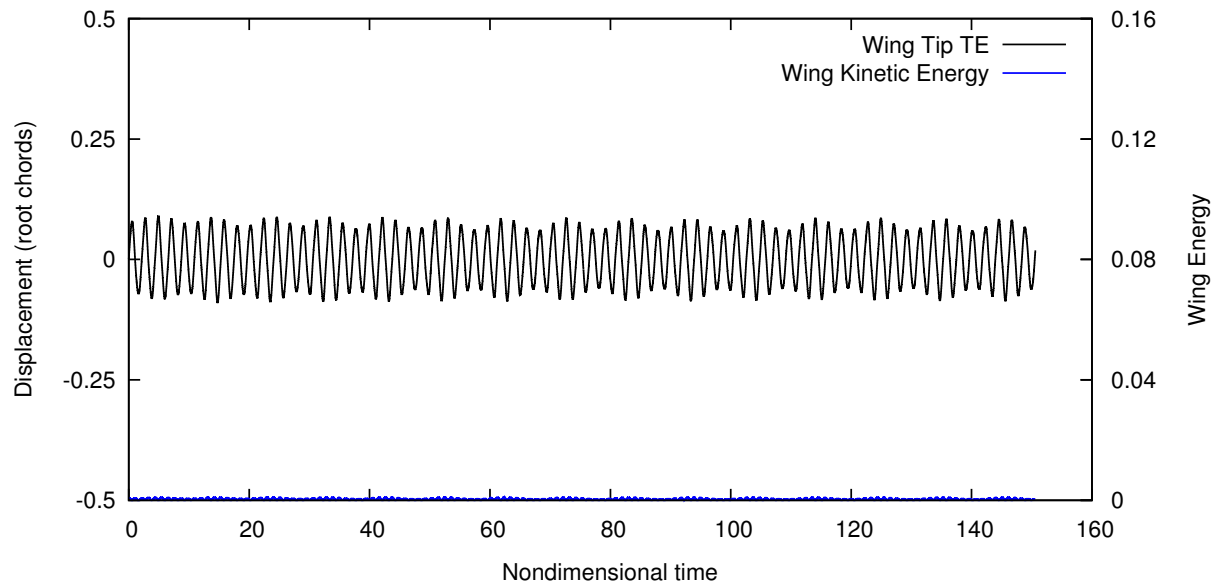


Figure 6.78: *FX-35: Neutrally stable plunge response in the Mach freeze region; modes besides first-bending begin to drop off as Mach number increases (Mach 1.03, density 0.2 kg/m^3).*

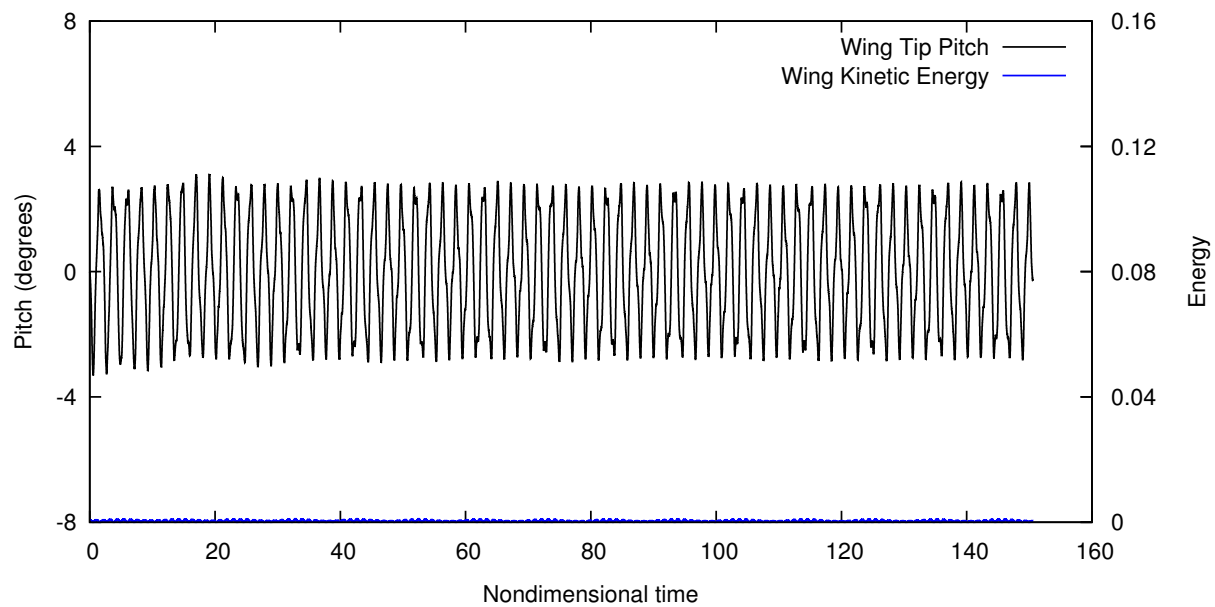


Figure 6.79: *FX-35: Neutrally stable pitch response in the Mach freeze region; modes besides first-bending begin to drop off as Mach number increases (Mach 1.03, density 0.2 kg/m^3).*

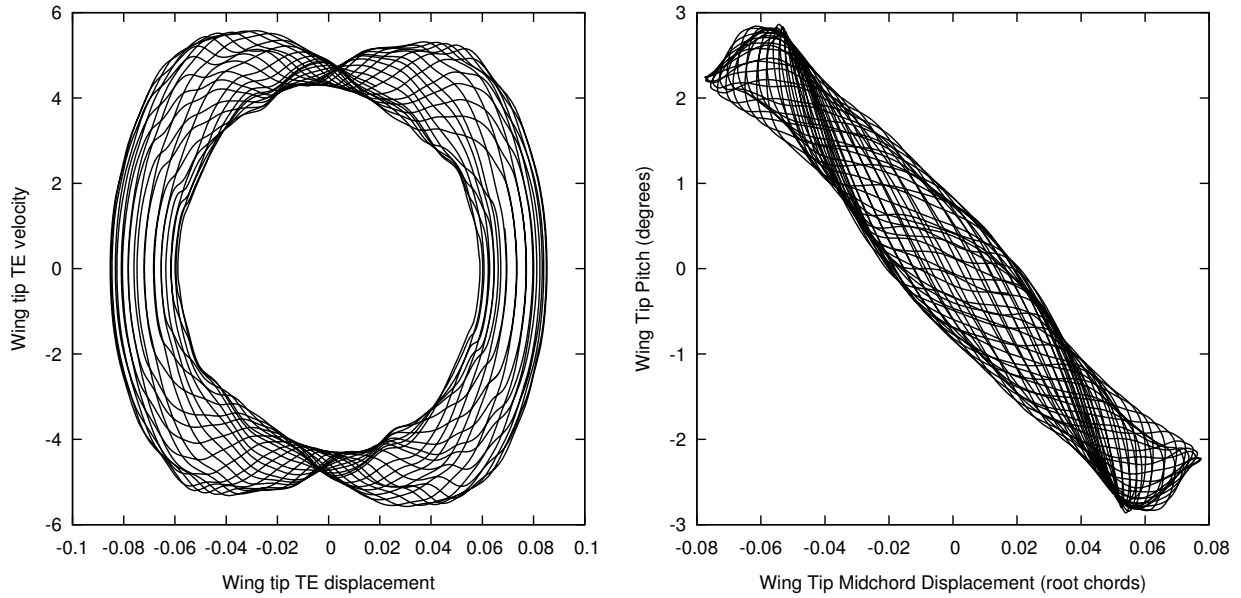


Figure 6.80: *FX-35: Mach freeze region phase plots showing the decreasing participation of second-bending (Mach 1.03, density 0.2 kg/m³).*

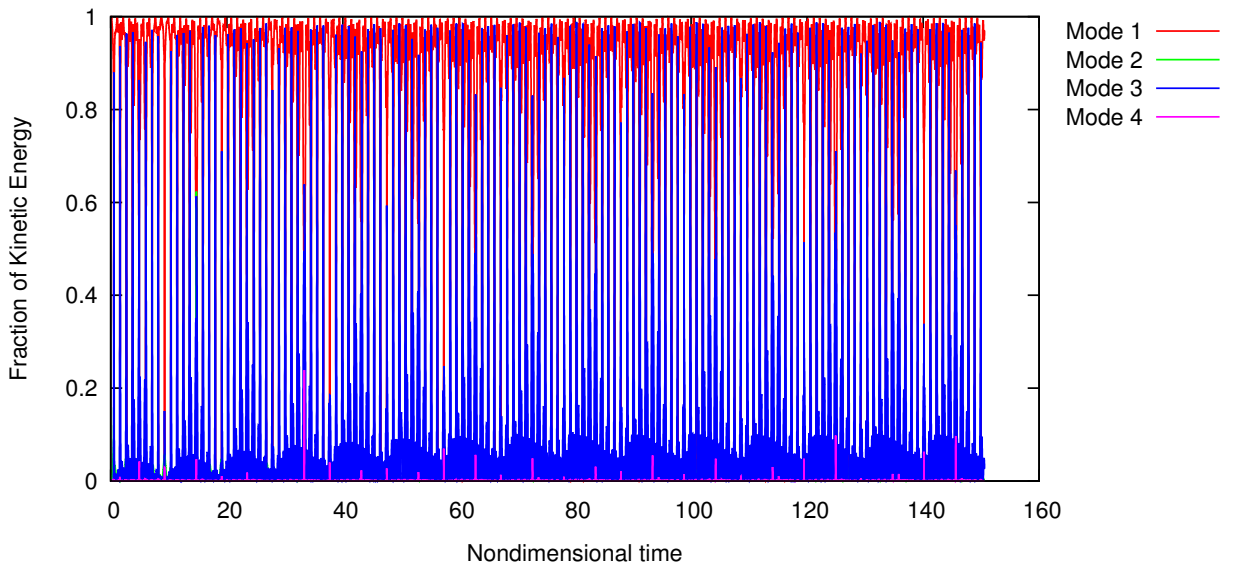


Figure 6.81: *FX-35: Distribution of kinetic energy across natural modes over time (Mach 1.03, density 0.2 kg/m³).*

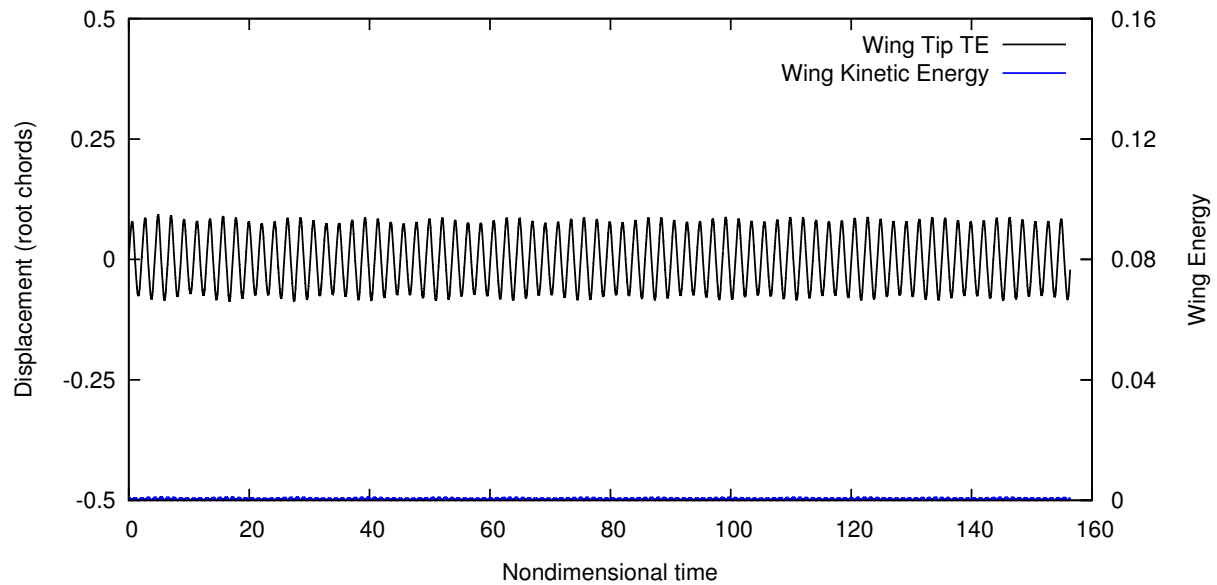


Figure 6.82: *FX-35: Neutrally stable plunge response in the Mach freeze region (Mach 1.05, density 0.2 kg/m^3).*

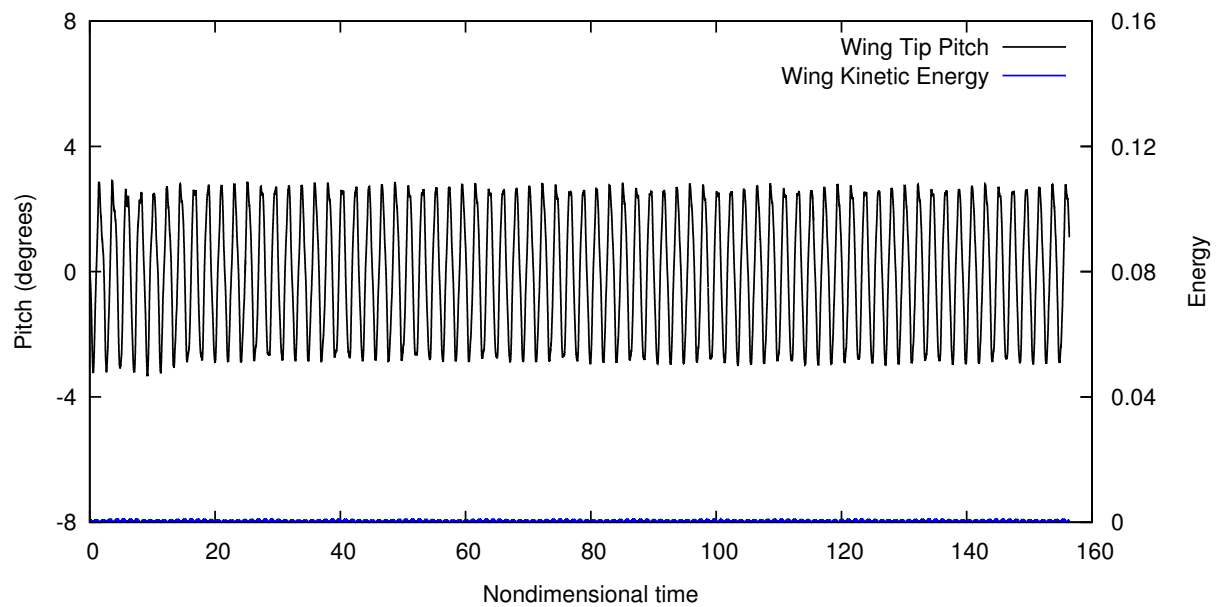


Figure 6.83: *FX-35: Neutrally stable pitch response in the Mach freeze region (Mach 1.05, density 0.2 kg/m^3).*

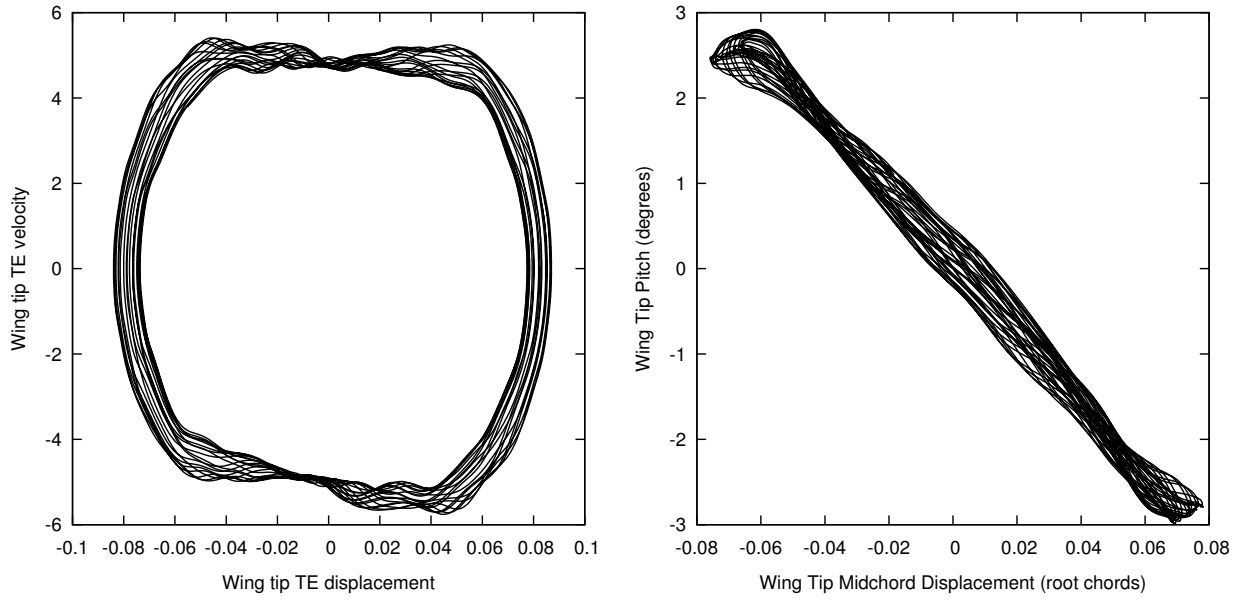


Figure 6.84: *FX-35: Mach freeze region phase plots showing a return to pure first-bending patterns at higher Mach number (Mach 1.05, density 0.2 kg/m^3).*

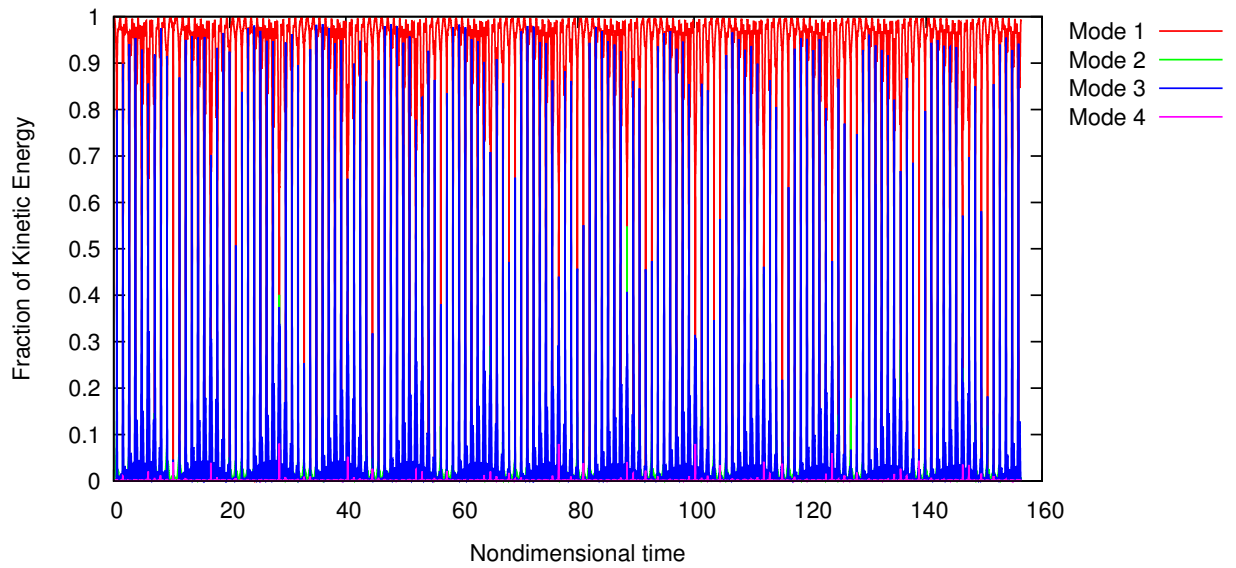


Figure 6.85: *FX-35: Distribution of kinetic energy across natural modes over time (Mach 1.05, density 0.2 kg/m^3).*

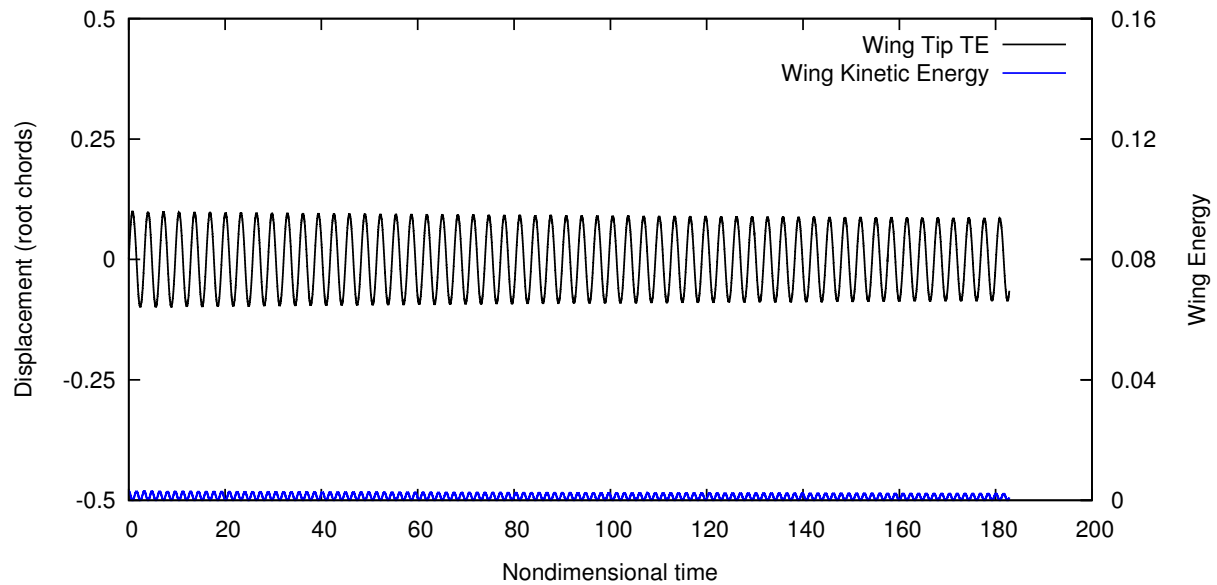


Figure 6.86: *FX-35: Neutrally stable plunge response in the Mach freeze region (Mach 1.04, density 0.05 kg/m^3).*

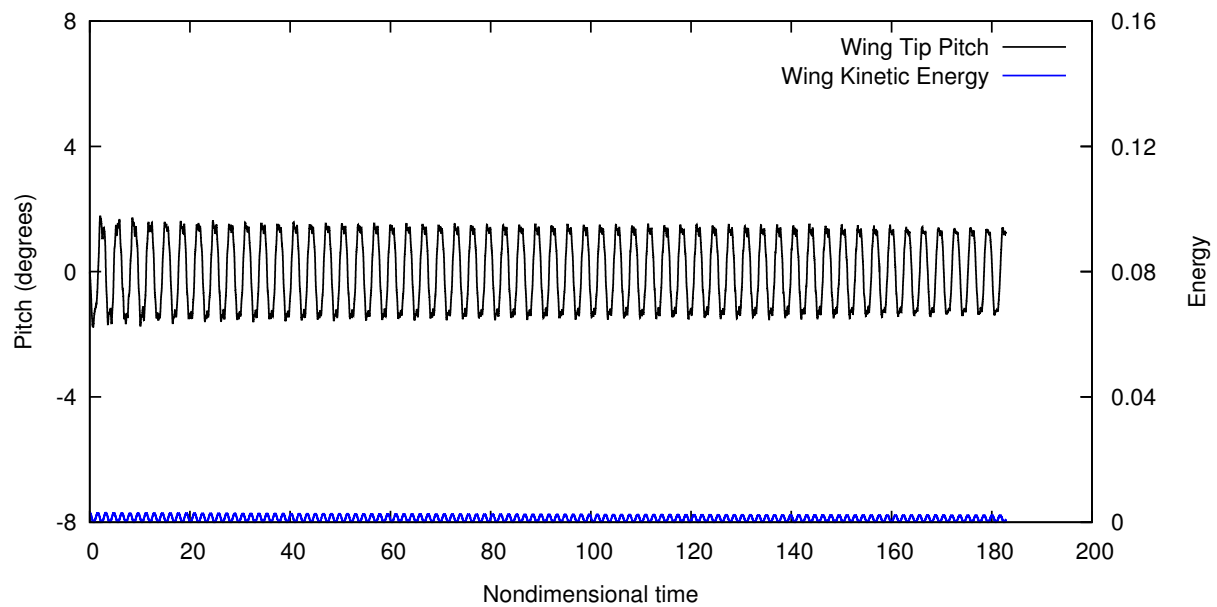


Figure 6.87: *FX-35: Neutrally stable pitch response in the Mach freeze region (Mach 1.04, density 0.05 kg/m^3).*

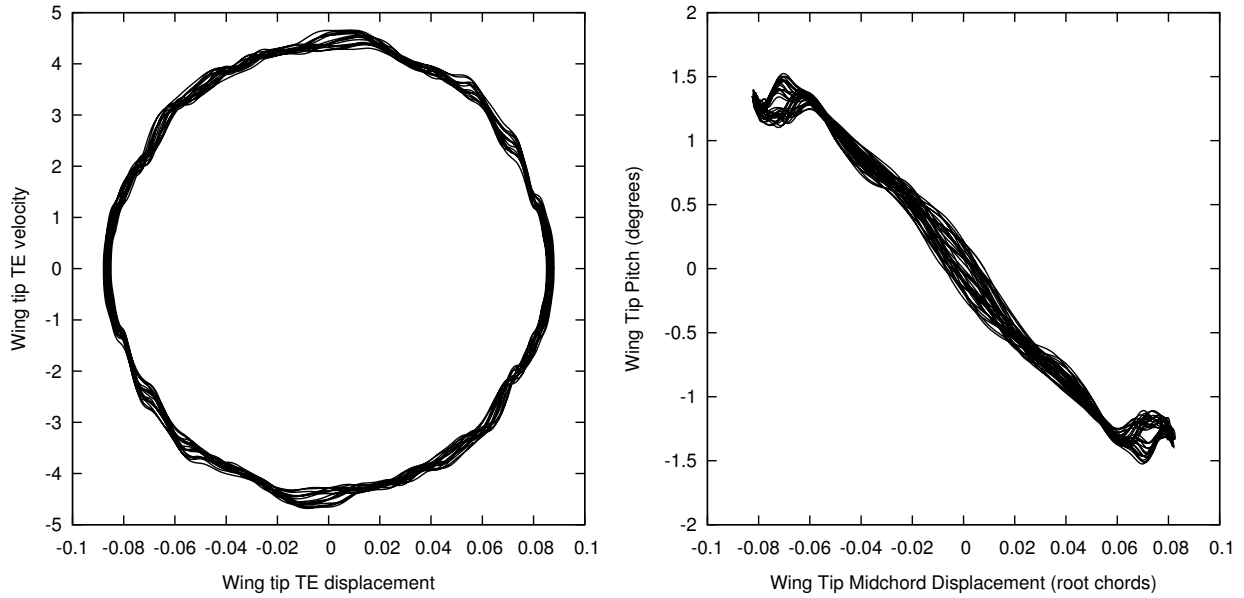


Figure 6.88: *FX-35: Mach freeze region phase plots showing a return to pure first-bending patterns at higher Mach number (Mach 1.04, density 0.05 kg/m^3).*

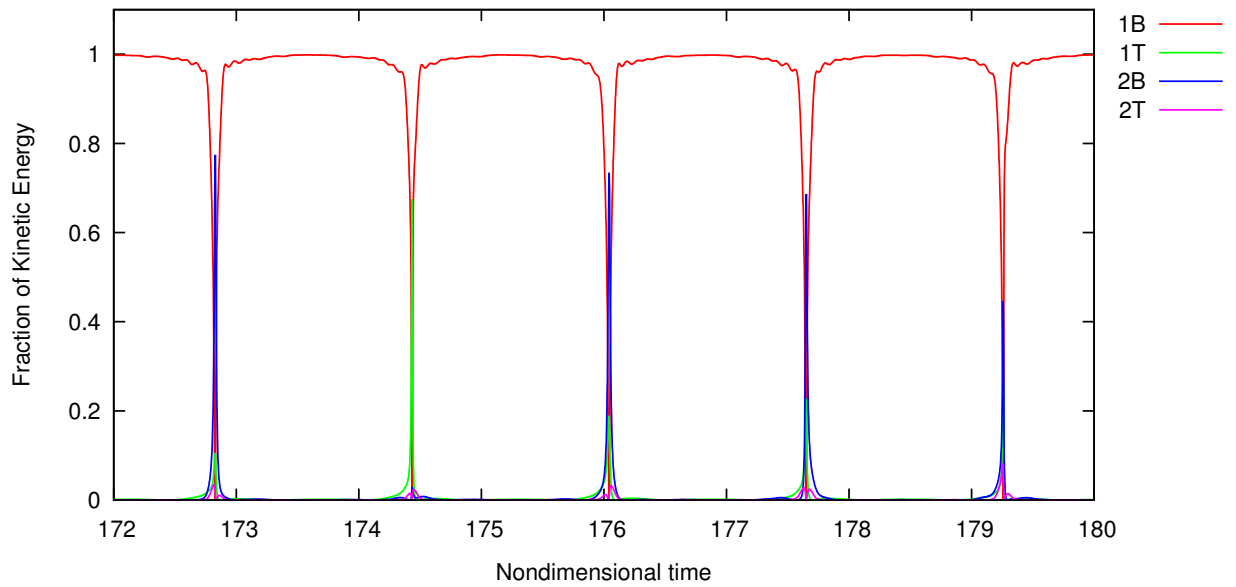


Figure 6.89: *FX-35: Distribution of kinetic energy across natural modes over time (Mach 1.04, density 0.05 kg/m^3).*

6.5.2 F-Wing: Mach Freeze

The Mach freeze for the F-Wing is not so blatantly obvious as it was for the FX-35. The same general effect is present, which is that the strength of the flutter response is tempered considerably for a small increase in Mach number when passing Mach 1.00. The difference is that the FX-35 switched very suddenly from explosive first-bending flutter to a neutrally stable response with moderate amplitude, and the F-Wing doesn't. Instead, many test points maintain first-bending flutter with a drop in rate of growth or have slow growing multi-mode responses. Lower density test points still become neutrally stable, but higher densities do not experience the powerful quenching. It's possible that the same result exists at higher densities for the FX-35, and that the F-Wing pattern occurs over a more compact range.

Figure 6.90 shows a high density series of wing tip plunge and pitch plots from Mach 0.98 to Mach 1.01. The drop in rate of growth between Mach 0.99 and Mach 1.00 is still significant, but the response picks up again right away at Mach 1.01. Overall, the F-Wing shows considerably less proclivity towards neutrally stable responses in this region when compared to the FX-35. Because higher densities are so far outside the TDT test range, they were not considered, and as a result there are simply not enough test points to make a determination about what sort of cap may exist on the reach of the Mach freeze effect based on this data alone. Suffice it to say, the effect is still present here, but with more underwhelming results.

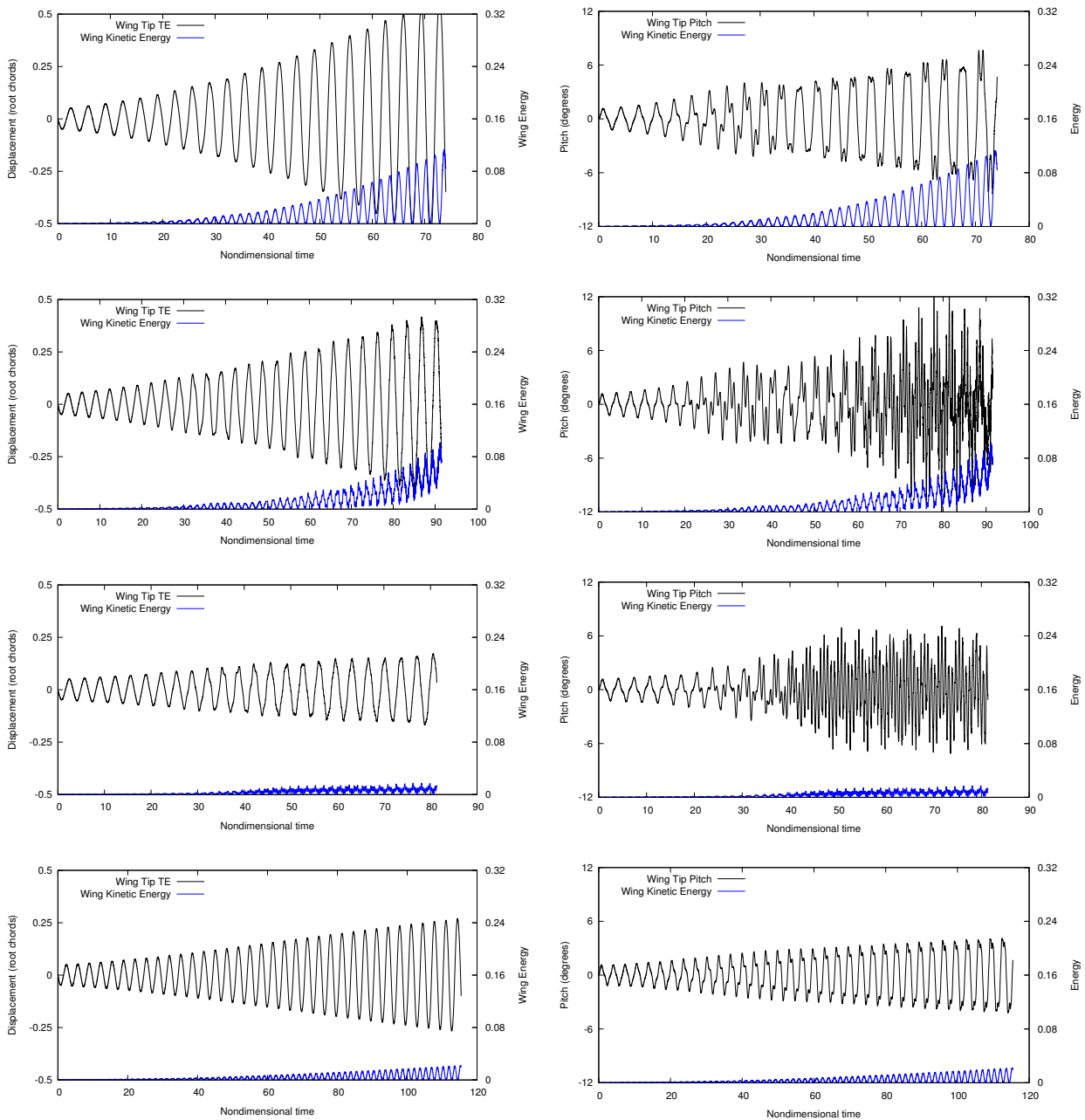


Figure 6.90: *F-Wing: Plunge (left) and pitch (right) responses for Mach 0.98 through Mach 1.01 (density 0.2 kg/m^3) showing the tempering effect of the Mach number freeze starting around Mach 1.00.*

The supersonic F-Wing response is divided very sharply between Mach 1.00 and the rest of the region. In the series shown above, the Mach freeze causes the response to transition from bending-torsion flutter at Mach 0.98 to bending-bending at Mach 1.00, which then immediately transitions back to bending-torsion at Mach 1.01. Overall, Mach 1.00 sees heavy participation of the second-bending mode, which then disappears almost entirely for the remainder of the supersonic test points.

The Mach 1.00 test points show no significant involvement of torsion modes and no multi-mode LCO responses. Even at very low density the response is weakly unstable, as seen in Figure 6.91. Looking at the kinetic energy distribution in Figure 6.92, the first-bending mode is dominant, but hints of other modes can be seen. As density increases, so does second-bending participation, until eventually both modes are present in nearly equal force. Figures 6.93 through 6.96 show the response created from heavy competition between the first two bending modes.

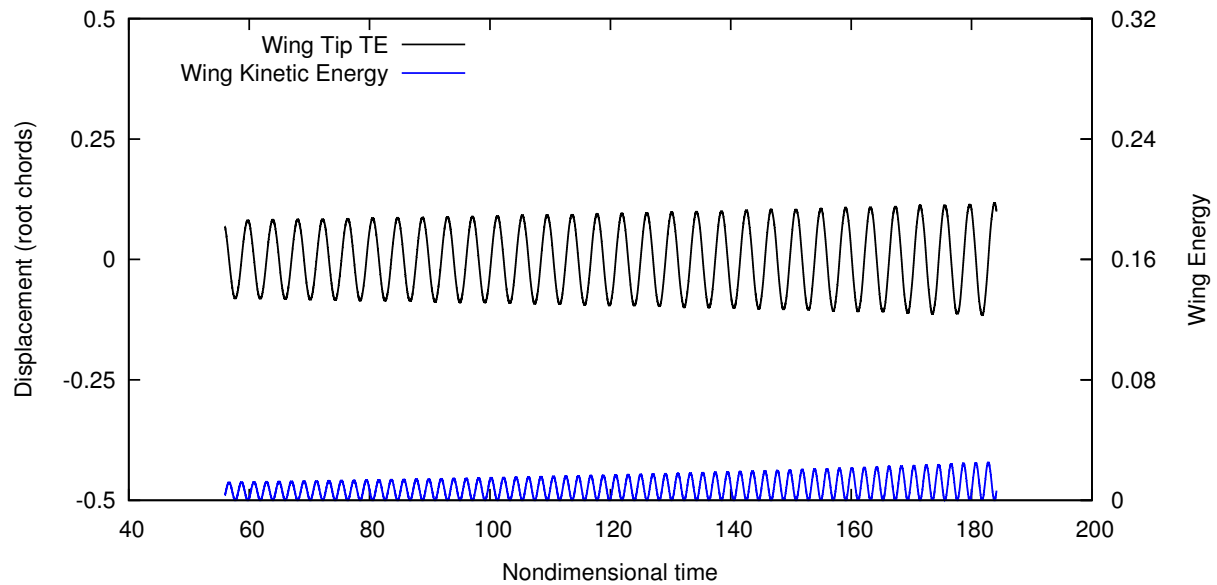


Figure 6.91: *F-Wing*: Weakly unstable plunge response in the Mach freeze region (Mach 1.00, density 0.02 kg/m^3).

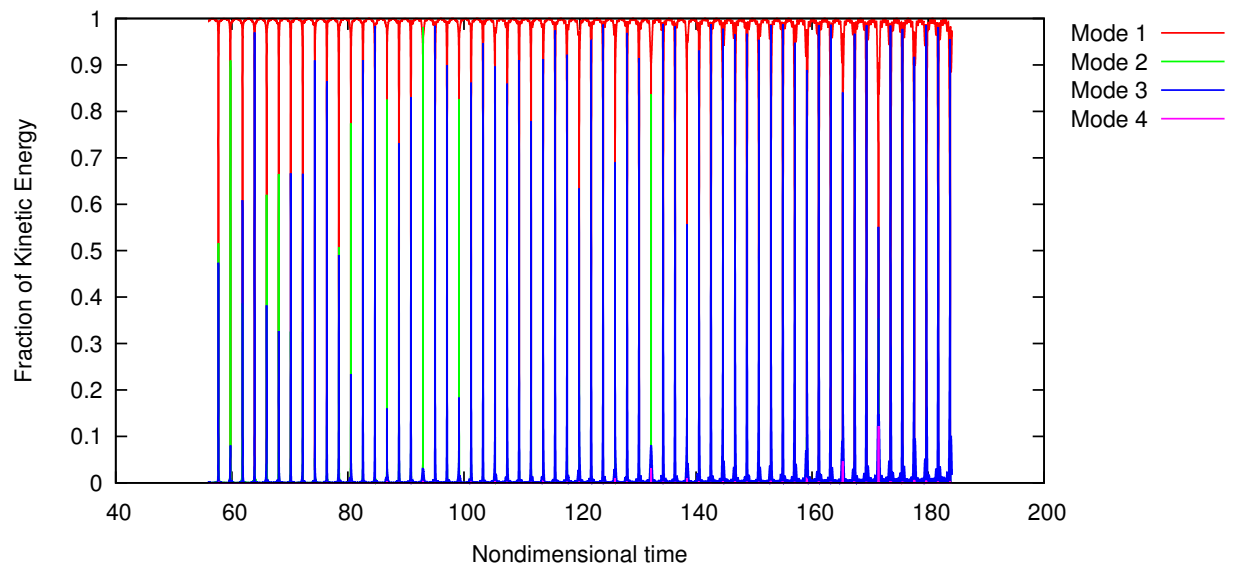


Figure 6.92: *F-Wing*: Distribution of kinetic energy across natural modes over time (Mach 1.00, density 0.02 kg/m^3).

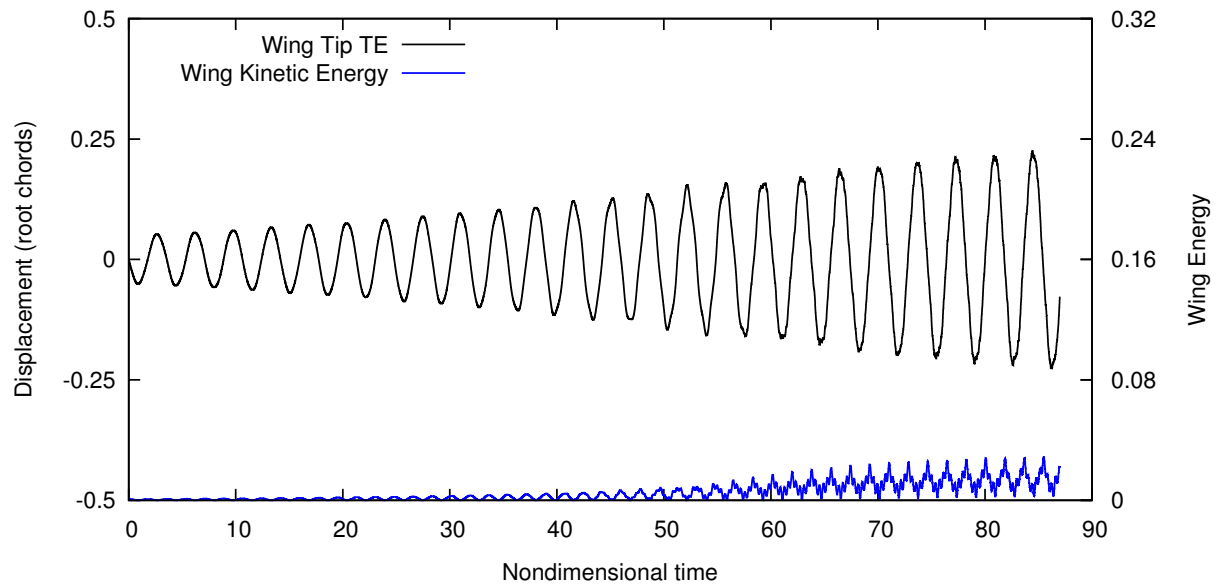


Figure 6.93: *F-Wing: Unstable plunge response in the Mach freeze region (Mach 1.00, density 0.15 kg/m^3).*

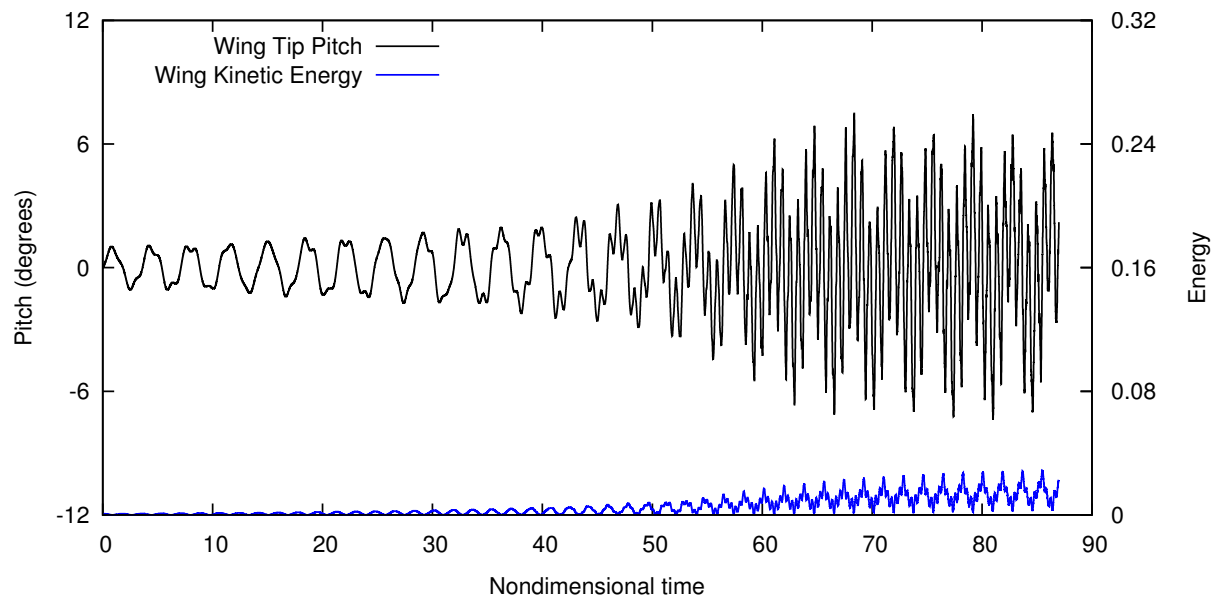


Figure 6.94: *F-Wing: Unstable pitch response in the Mach freeze region (Mach 1.00, density 0.15 kg/m^3).*

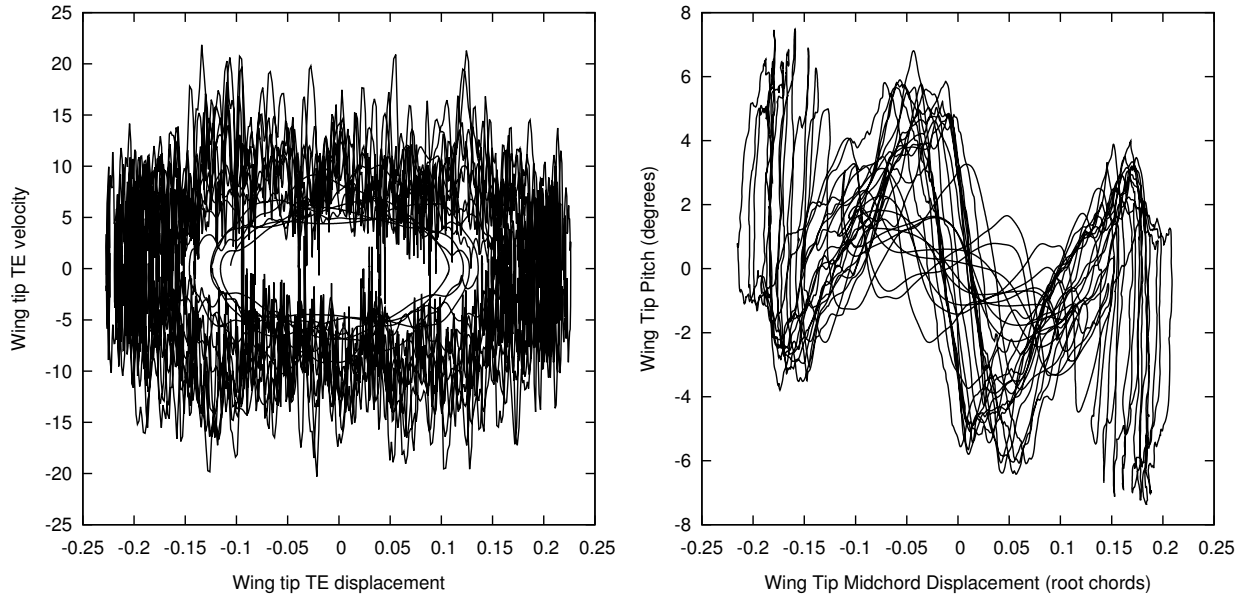


Figure 6.95: *F-Wing: Mach freeze region phase plots showing erratic patterns as first-bending and second-bending interact (Mach 1.00, density 0.15 kg/m³).*

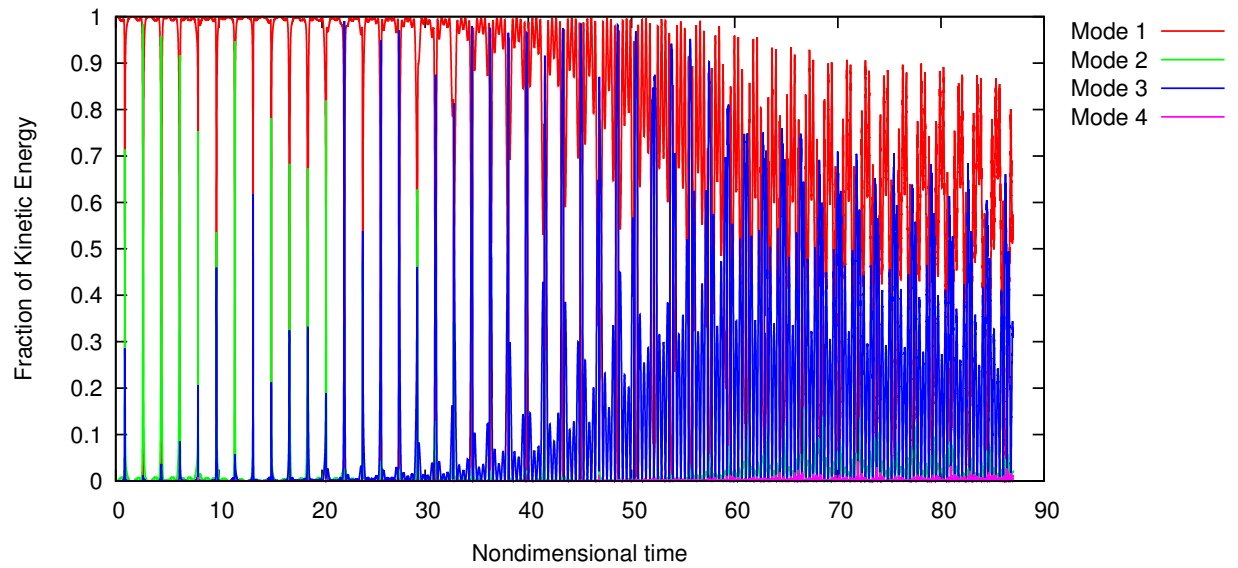


Figure 6.96: *F-Wing: Distribution of kinetic energy across natural modes over time (Mach 1.00, density 0.15 kg/m³).*

From Mach 1.01 to Mach 1.05 the character of the response becomes surprisingly simple. At low densities the first-bending mode exists almost entirely by itself and is neutrally stable. It is quite rare to see a condition so completely void of mode competition. Figures 6.97 through 6.100 show an example of an Essentially Single Degree of Freedom response. The phase plots are exceptionally smooth, and multi-mode presence is so low that the kinetic energy response hardly even dips at peak displacement, where first-bending is nearly stationary. With increasing density, the response becomes weakly unstable and sees very slight competition from second-bending. At high density, seen in Figures 6.101 through 6.104, the response transitions to the bending-torsion flutter that characterized unstable subsonic conditions.

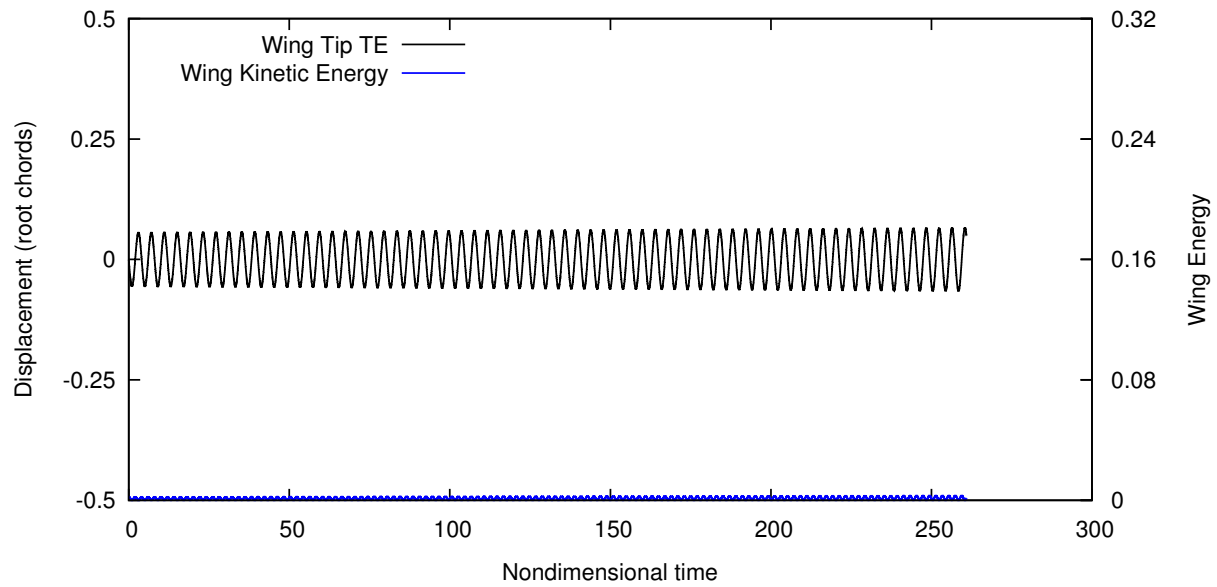


Figure 6.97: *F-Wing: Neutrally stable plunge response in the Mach freeze region (Mach 1.03, density 0.05 kg/m^3).*

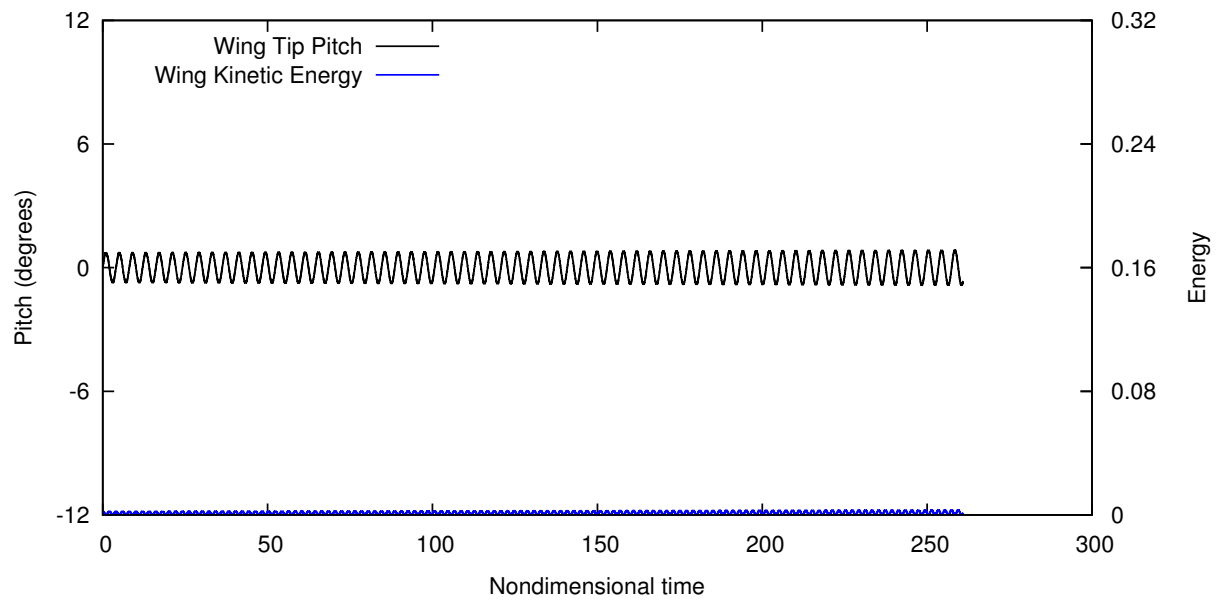


Figure 6.98: *F-Wing: Neutrally stable pitch response in the Mach freeze region (Mach 1.03, density 0.05 kg/m^3).*

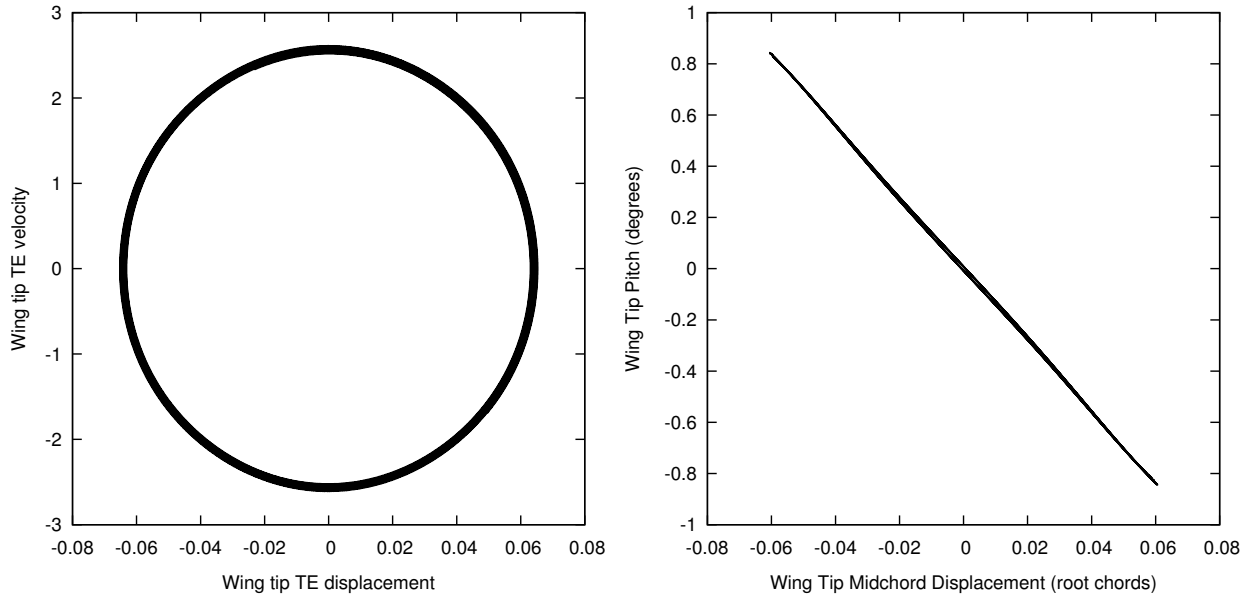


Figure 6.99: *F-Wing: Mach freeze region phase plots showing essentially single degree-of-freedom first-bending patterns at higher Mach number (Mach 1.03, density 0.05 kg/m^3).*

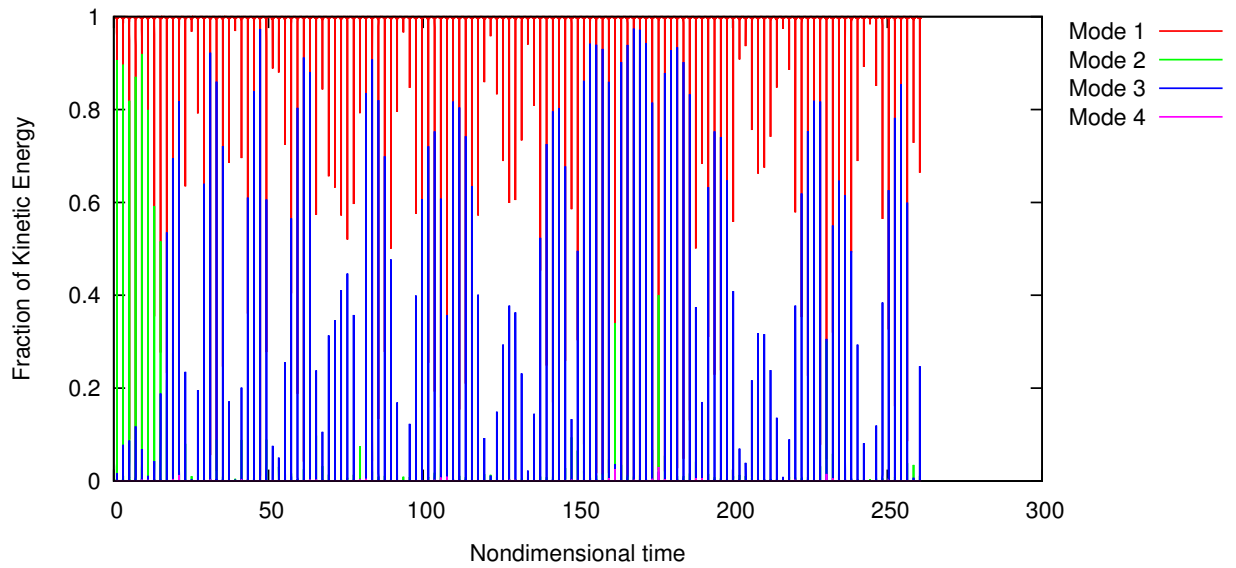


Figure 6.100: *F-Wing: Distribution of kinetic energy across natural modes over time (Mach 1.03, density 0.05 kg/m^3).*

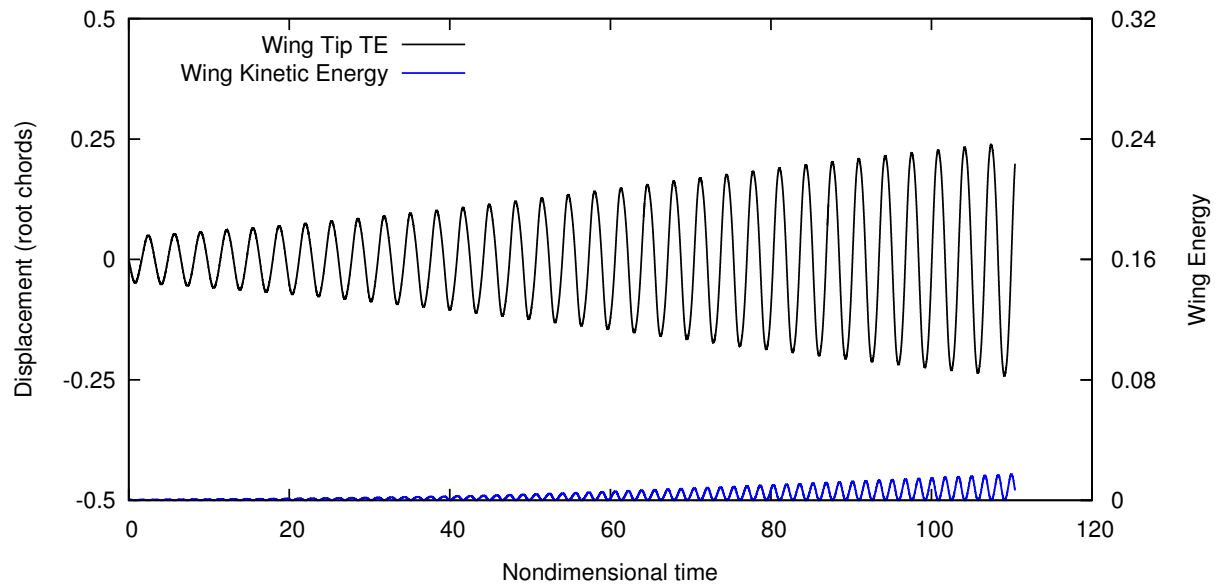


Figure 6.101: *F-Wing: Unstable plunge response in the Mach freeze region (Mach 1.02, density 0.2 kg/m³).*

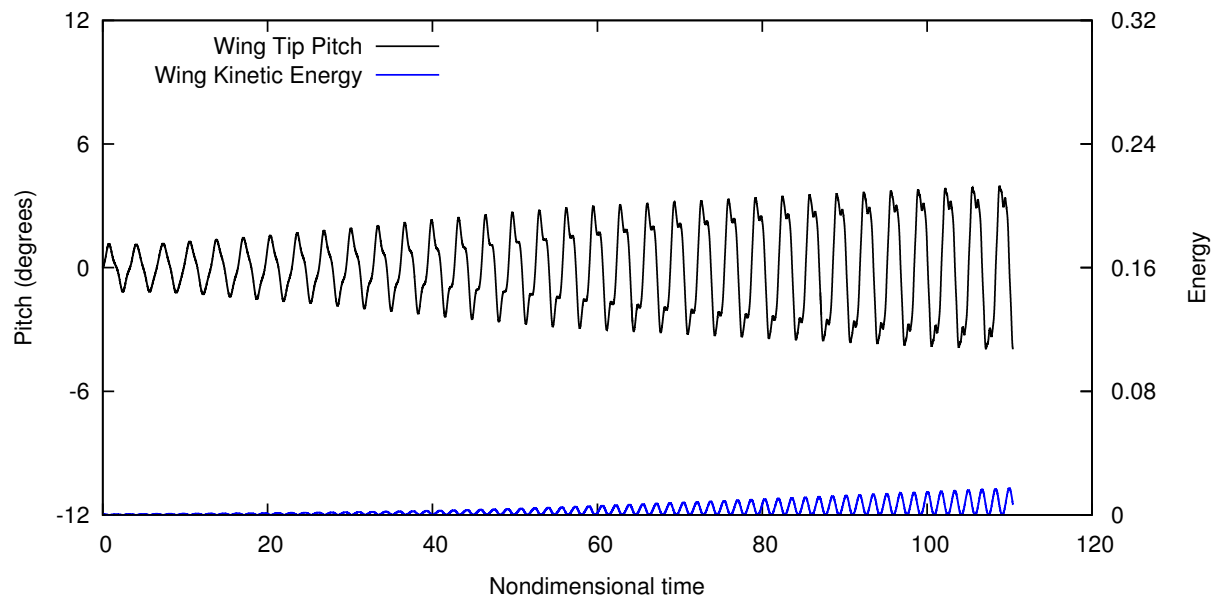


Figure 6.102: *F-Wing: Unstable pitch response in the Mach freeze region (Mach 1.02, density 0.2 kg/m³).*

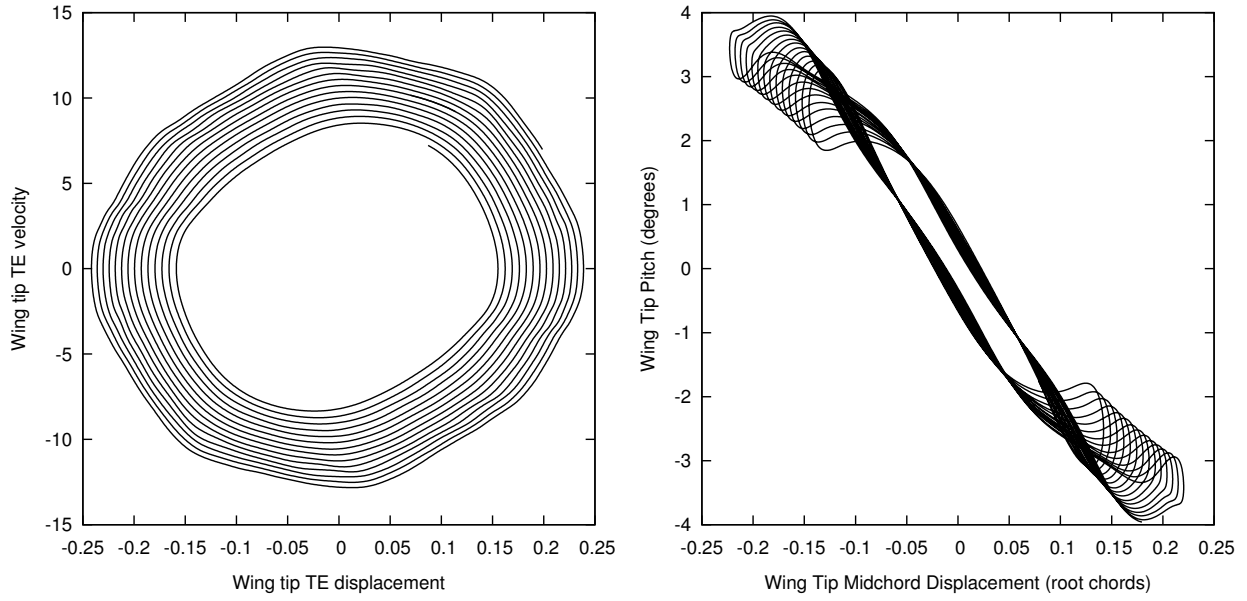


Figure 6.103: *F-Wing: Mach freeze region phase plots showing a transition to bending-torsion flutter (Mach 1.02, density 0.2 kg/m³).*

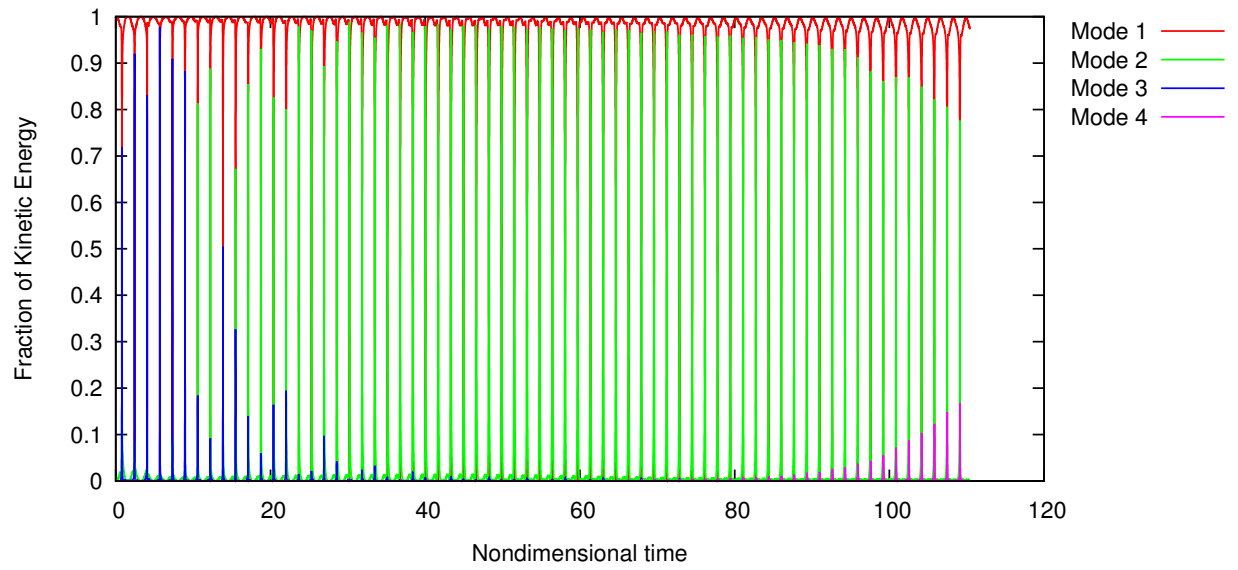


Figure 6.104: *F-Wing: Distribution of kinetic energy across natural modes over time (Mach 1.02, density 0.2 kg/m³).*

Chapter 7

Conclusions

7.1 Introduction

A parallel implementation of the Direct Eulerian-Lagrangian Method was successfully developed and optimized for use on multi-core shared-memory computational nodes. The program was used to develop two fighter wing models that are both excellent candidates for transonic wind tunnel testing. Results show a range of known flutter phenomena that have been previously identified in wind tunnel tests and numerical simulations for cranked aircraft wings.

7.2 Conclusions

The main conclusions of this study are as follows:

1. Parallelization was shown to be a worthwhile investment for reducing the time taken to obtain results using the Direct Eulerian-Lagrangian Method without changes to the

algorithm and without loss of accuracy.

2. The Direct Eulerian-Lagrangian Method was applied to fighter wings on a large volume of test points, providing a greater level detail about the boundaries and nuances of flutter behavior transitions than was known previously.
3. The FX-35 and F-Wing fighter wing models were shown to exhibit complex flutter behaviors within the operating parameters of the Transonic Dynamics Tunnel; either would provide valuable physical test data that is not currently available for use in validation of computational methods.
4. For both wings, a clear subsonic flutter stability boundary was observed with respect to density. Above this boundary, increased density results in a transition from weakly unstable first-bending flutter to fast-growing strong bending-torsion flutter.
5. Both the FX-35 and F-Wing experience a deep chimney of neutrally stable second-bending responses starting around Mach 0.95 that continue down to near-zero density. As Mach number increases towards 1.00, the first-bending and first-torsion modes show increased participation in these responses.
6. Around Mach 1.00, the flutter response of both wings is tempered considerably, often resulting in neutrally stable LCOs at previously unstable conditions. This is thought to be the result of the normal shocks reaching the trailing edge of the wing surface.
7. The FX-35 was shown to exhibit a variety of LCO behaviors, including ESDOF and multi-mode responses, over a wide range of Mach numbers and densities in the supersonic region. Of particular interest are 1B-1T-2B responses where all three modes

compete for dominance without establishing a clear hierarchy.

8. The F-Wing was shown to exhibit a short range of coupled first and second-bending responses directly after Mach 1.00, followed by ESDOF first-bending LCOs at low density for Mach 1.01 through Mach 1.05. These conditions transitioned to strong bending-torsion flutter at higher densities.

Bibliography

- [1] S. B. Smith and D. W. Nelson, “Determination of the aerodynamic characteristics of the mission adaptive wing,” *Journal of Aircraft*, vol. 27, pp. 1037–1047, November 1990.
- [2] B. Perry III, S. R. Cole, and G. D. Miller, “A summary of the active flexible wing program,” in *AIAA Paper 92-2080*, (Proc. AIAA Dynamics Specialist Conf Dallas, Texas), pp. 1–10, April 16-17, 1992.
- [3] e. a. Pendelton, E., “The active aeroelastic wing flight research program,” in *AIAA Paper 98-1972*, (Proc. AIAA/ASME/ASCE/AHS/ASC 39th SDM Conf., Long Beach, CA), April 20-23, 1998.
- [4] R. L. Bisplinghoff, H. Ashley, and R. L. Halfman, *Aeroelasticity*. Addison-Wesley.
- [5] H. Ashley, “Role of shocks in the “sub-transonic” flutter phenomenon,” *Journal of Aircraft*, vol. 17, no. 3, pp. 187–197, 1980.
- [6] O. O. Bendiksen, “Role of shock dynamics in transonic flutter,” *AIAA Dynamics Specialists Conference, Dallas, TX*, pp. 401–414, 1992.

- [7] K. Bhatia and J. Wertheimer, “Aeroelastic challenges for a high speed civil transport,” (34th AIAA/ASME/ASCE/AHS/ASC Structures, Structural Dynamics, and Materials Conference, La Jolla, CA), pp. 3663–3682, 1993.
- [8] W. Silva, D. Keller, J. Florance, S. Cole, and R. Scott, “Experimental steady and unsteady aerodynamic and flutter results for hsct semispan models,” in *41st AIAA/ASMC/ASCE/AHS/ASC Structures, Structural Dynamics, and Materials Conference*, (Atlanta, GA), April 2000.
- [9] O. O. Bendiksen, “A new approach to computational aeroelasticity,” *Proc.*, vol. 32, pp. 1712–1727, April 1991.
- [10] O. O. Bendiksen, “Modern developments in computational aeroelasticity,” *Proceedings of the Institution of Mechanical Engineers. Part G: Journal of Aerospace Engineering*, vol. 218, no. 3, pp. 157–177, 2004.
- [11] O. O. Bendiksen and G. Seber, “A direct fluid-structure coupling scheme for nonlinear finite element aeroelastic codes,” (International Forum on Aeroelasticity and Structural Dynamics, Stockholm, Sweden), 2007.
- [12] G. Y. Hwang, *Parallel Finite Element Solutions of Nonlinear Aeroelastic and Aeroelastic Problems in Three-Dimensional Transonic Flows*. PhD thesis, Mechanical and Aerospace Engineering Department, University of California, Los Angeles, March 1997.
- [13] G. Seber, *Aeroelastic Wing Response Analysis Using Finite Elements in a Large Deformation Direct Eulerian-Lagrangian Formulation*. PhD thesis, Mechanical and Aerospace Engineering Department, University of California, Los Angeles, 2004.

- [14] E. M. Murman and J. D. Cole, "Calculation of plane steady transonic flows," *AIAA Journal*, vol. 9, no. 1, pp. 114–121, 1971.
- [15] W. F. Ballhaus and F. R. Bailey, "Numerical calculation of transonic flow about swept wings," in *5th AIAA Fluid and Plasma Dynamics Conference*, (Boston, M. A.), June 1972.
- [16] W. F. Ballhaus and P. M. Goorjian, "Implicit finite-difference computations of unsteady transonic flows about airfoils," *AIAA Journal*, vol. 15, no. 12, pp. 1728–1735, 1977.
- [17] C. J. Borland, D. P. Rizzetta, and H. Yoshihar, "Numerical solution of three-dimensional unsteady transonic flow over swept wings," *AIAA Journal*, vol. 20, no. 3, pp. 340–347, 1982.
- [18] W. Ballhaus and P. Goorjian, "Computation of unsteady transonic flows by the indicial method," *AIAA Journal*, vol. 16, no. 2, pp. 117–124, 1978.
- [19] D. P. Rizzetta, "Time-dependent response of a two-dimensional airfoil in transonic flow," *AIAA Journal*, vol. 17, no. 1, pp. 26–32, 1979.
- [20] C. Borland and D. Rizzetta, "Nonlinear transonic flutter analysis," *AIAA Journal*, vol. 20, pp. 1606–1615, 1982.
- [21] V. Venkatakrishnan and A. Jameson, "Computation of unsteady transonic flows by the solution of euler equations," *AIAA Journal*, vol. 26, no. 8, pp. 974–981, 1988.
- [22] O. O. Bendiksen and K. Kousen, "Transonic flutter analysis using the euler equations," in *Aiaa Dynamics Specialists Conference*, (Monterey, C. A.), April 1987.

- [23] K. Kousen and O. O. Bendiksen, “Nonlinear aspects of the transonic aeroelastic stability problem,” in *29th AIAA/ASME/ASCE/AHS Structures, Structural Dynamics and Materials Conference*, (Williamsburg, VA), 1988.
- [24] J. C. Wu, L. N. Sankar, and K. R. V. Kaza, “A technique for the prediction of airfoil flutter characteristics in separated flows,” *Journal of Aircraft*, vol. 26, no. 2, pp. 168–177, 1989.
- [25] J. C. Wu, *A Study of Unsteady Turbulent Flow Past Airfoils*. PhD thesis, Georgia Institute of Technology, Atlanta, GA, August 1988.
- [26] G. P. Guruswamy, “Unsteady aerodynamic and aeroelastic calculations for wings using euler equations,” *AIAA Journal*, vol. 28, no. 3, pp. 461–469, 1990.
- [27] G. Guruswamy, “Numerical simulation of vortical flows on flexible wings,” in *27th Aerospace Sciences Meetings*, (Reno, N. V.), January 1989.
- [28] G. Guruswamy, “Vortical flow computations on swept flexible wings using navier-stokes equations,” in *30th AIAA/ASME/ASCE/AHS/ASC Structures, Structural Dynamics and Materials Conference*, (Mobile, AL), April 1989.
- [29] G. P. Guruswamy and C. Byun, “Fluid-structural interactions using navier-stokes flow equations coupled with shell finite element structures,” in *24th AIAA Fluid Dynamics Conference* (F. L. Orlando, ed.), 1993.
- [30] B. A. Robinson, H. T. Y. Yang, and J. T. Batina, “Aeroelastic analysis of wings using the euler equations with a deforming mesh,” *Journal of Aircraft*, vol. 28, no. 11, pp. 781–788, 1991.

- [31] E. M. Lee-Rausch and J. T. Batina, “Wing flutter boundary prediction using unsteady euler aerodynamic method,” *Journal of Aircraft*, vol. 32, pp. 416–422, March 1995.
- [32] E. Lee-Rausch and J. T. Baitina, “Wing flutter computations using an aerodynamic model based on the navier-stokes equations,” *Journal of Aircraft*, vol. 33, no. 6, pp. 1139–1147, 1996.
- [33] J. T. Batina, “Unsteady euler airfoil solutions using unstructured dynamic meshes,” *AIAA Journal*, vol. 28, no. 8, pp. 1381–1388, 1990.
- [34] G. Y. Hwang and O. O. Bendiksen, “Parallel finite element solutions of nonlinear aeroelastic problems in 3d transonic flow,” in *38th AIAA/ASME/ASCE/AHS/ASC Structures, Structural Dynamics and Materials Conference*, (Kissimmee, FL), April 1997.
- [35] G. A. Davis and O. O. Bendiksen, “Transonic panel flutter,” *AIAA Paper*, pp. 93–1476, April 1993.
- [36] O. O. Bendiksen, “Transonic limit cycle flutter/lco,” (Proc. AIAA/ASME/ASCE/AHS/ASCE 45TH SDM Conf, Palm Springs, CA), Aiaa Paper, 04-1694, April 19-22, 2004.
- [37] R. E. Gordnier, “Computation of limit-cycle oscillations of a delta wing,” *Journal of Aircraft*, vol. 40, no. 6, pp. 1206–1207, 2003.
- [38] B. B. Pranata, J. C. Kok, S. P. Spekrijse, M. H. L. Hounjet, and J. J. Meijer, “Simulation of limit cycle oscillation of fighter aircraft at moderate angle of attack,” in *Proceedings of the International Forum on Structural Dynamics and Aeroelasticity 2003*

- [CD-ROM] (N. A. of Aeronautical Engineers, ed.), (Amsterdam, The Netherlands), 4-6 June 2003.
- [39] P. J. Attar, E. H. Dowell, and J. R. White, “Modeling the lco of a delta wing using a high fidelity structural model,” in *45th AIAA/ASME/ASCE/AHS/ASC Structures, Structural Dynamics and Materials Conference*, (Palm Springs, CA), 2004.
- [40] S. Machida, T. Kikuchi, H. Arizono, K. Saitoh, and J. Nakamichi, “Transonic flutter characteristics of an arrow wing mounted with engine,” in *43rd AIAA Aerospace Sciences Meeting and Exhibit*, (Reno, Nevada), 2005.
- [41] O. O. Bendiksen, “Role of mach number freeze in transonic flutter,” in *International Forum on Aeroelasticity and Structural Dynamics*, (Bristol, UK), June 2013.
- [42] E. Mellquist, *Computational Transonic Flutter Solutions for Cranked Wings by the Direct Eulerian-Lagrangian Method*. PhD thesis, Mechanical and Aerospace Engineering Department, University of California, Los Angeles, 2014.
- [43] G. A. Davis, *Transonic Aeroelasticity Solutions Using Finite Element in an Arbitrary Lagrangian-Eulerian Formulation*. PhD thesis, Mechanical and Aerospace Engineering Department, University of California, Los Angeles, 1994.
- [44] C. Hsiao, *Mixed Euler-Lagrangian Finite Element Solutions of Unsteady Flow and Flutter in Transonic Cascades*. PhD thesis, Mechanical and Aerospace Engineering Department, University of California, Los Angeles, 1993.
- [45] O. O. Bendiksen, “High-altitude limit cycle flutter of transonic wings,” *Journal of Aircraft*, vol. 46, no. 1, pp. 123–136, 2009.

- [46] O. O. Bendiksen, “Transonic stabilization laws for unsteady aerodynamics and flutter,” in *53rd AIAA/ASME/ASCE/AHS/ASC Structures, Structural Dynamics and Materials Conference*, (Honolulu, HI), April 2012.
- [47] A. Jameson and D. Mavriplis, “Finite volume solution of the two-dimensional euler equations on a regular triangular mesh,” *AIAA Journal*, vol. 24, pp. 611–618, 1986.
- [48] D. J. Mavriplis, “Accurate multigrid solution of the euler equations on unstructured and adaptive meshes,” *AIAA Journal*, vol. 28, no. 2, pp. 213–221, 1990.
- [49] G. A. Davis and O. O. Bendiksen, “Unsteady transonic two-dimensional euler solutions using finite elements,” *AIAA Journal*, vol. 31, no. 6, pp. 1051–1058, 1993.
- [50] G. Seber and O. O. Bendiksen, “Nonlinear flutter calculations using finite elements in a direct eulerian-lagrangian formulation,” *AIAA Journal*, vol. 46, no. 6, pp. 1331–1341, 2008.
- [51] S. Rajasekaran and D. W. Murray, “Incremental finite element matrices,” *ASCE Journal of Structural Division*, pp. 2423–2438, December 1973.